Fakultät für Chemie

Investigation of Polyoxometalates and Nanostructured Carbon Materials as Electrode Materials for Energy Storage Applications

HAN-YI CHEN

Vollständiger Abdruck der von der Fakultät für Chemie der Technischen Universität München zur Erlangung des akademischen Grades eines Doktors der Naturwissenschaften (Dr. rer. nat.) genehmigten Dissertation.

Vorsitzender: Univ.-Prof. Dr. Tom Nilges
Prüfer der Dissertation: 1. Univ.-Prof. Dr. Ulrich Stimming
2. Prof. Dr. Madhavi Srinivasan

Die Dissertation wurde am 18.02.2016 bei der Technischen Universität München eingereicht und durch die Fakultät für Chemie am 17.03.2016 angenommen.

Abstract

Electrochemical energy storage devices such as lithium ion batteries (LIBs), sodium-ion batteries (NIBs) and supercapacitors (SCs) have been developed for various potential applications including portable electronics, electro-mobility, and large-scale stationary energy storage. This thesis focuses on developing novel polyoxometalates (POMs) and nanostructured carbon materials as electrode materials for SCs, LIBs, and NIBs, as well as investigating respective their charge storage/transport mechanism.

A polyoxovanadate, $Na_6[V_{10}O_{28}]$, is synthesized using a simple solution process, and studied as electrode materials for SCs and LIBs in this thesis. The electrochemical properties of $Na_6[V_{10}O_{28}]$ electrodes for SCs are investigated in Li-ion containing organic electrolyte utilizing galvanostatic charge/discharge and cyclic voltammetry in a three-electrode configuration. Activated carbon (AC) is employed as the positive electrode to assemble an asymmetric supercapacitor with $Na_6[V_{10}O_{28}]$ as the negative electrode in order to demonstrate that $Na_6[V_{10}O_{28}]$ is a promising electrode material for practical supercapacitor applications. The electrochemical properties of $Na_6[V_{10}O_{28}]$ as a cathode in LIBs is also tested by galvanostatic charge/discharge and cyclic voltammetry in a half-cell configuration, and exhibits a high capacity (up to 213 mAh g^{-1}). In order to figure out the charge storage and transport mechanism, in-situ V K-edge X-ray absorption fine structure (XAFS) measurements and temperature dependent Chronoamperometry measurements are utilized for $Na_6[V_{10}O_{28}]$ LIBs. Those techniques can detect the oxidation states and inner structure changes of $Na_6[V_{10}O_{28}]$ during charging/discharging, as well as determine the rate of electron transfer and the reorganization energy of $Na_6[V_{10}O_{28}]$ electrodes.

A POM/Carbon hybrid material is also investigated in this thesis for SC applications. A nanohybrid material which combines $(TBA)_5[PV^{V}_2Mo^{VI}_{10}O_{40}]$ (**TBA-PV_2Mo_{10}**, TBA: $[(CH_3(CH_2)_3)_4N]^+$, tetra-n-butyl ammonium) and single-walled carbon nanotubes (SWCNTs) is

synthesized by a simple solution method which electrostatically attaches anionic $[PV_2Mo_{10}O_{40}]^{5-}$ anions with organic TBA cations on the SWCNTs. **SWCNT-TBA-PV_2Mo_{10}** electrodes is tested in an acidic aqueous electrolyte by galvanostatic charge/discharge and cyclic voltammetry in three-electrode-configuration in order to figure out the electrochemical performance. In this **SWCNT-TBA-PV_2Mo_{10}** nanohybrid material, **TBA-PV_2Mo_{10}** offers redox activity while the TBA organic groups help to preventing dissolution in the aqueous electrolyte in order to increase the cycling stability, and SWCNTs offers high electrical conductivity with high double-layer capacitance that improve both energy and power density. A **SWCNT-TBA-PV_2Mo_{10}** symmetric SC is fabricated and exhibits a 39 % higher specific capacitance as compared to a SWCNT symmetric SC, and presents high cycling stability up to 6500 cycles.

A nanostructured carbon material, core–shell heterostructure with multi-walled carbon nanotubes (MWCNTs) as the core and graphene oxide nanoribbons (GONRs) as the shell (MWCNT@GONR), is also investigated as anode material for NIBs in this thesis. MWCNT@GONR with oxygen-containing functional groups is synthesized by unzipping process of MWCNTs utilizing microwave-assisted process. Annealing process is employed to study the influence of the amount of carboxylic acid groups on the electrochemistry of MWCNT@GONR. The novel core-shell structure prevents the restacking problem of graphene and enables penetration of the electrolyte. Furthermore, MWCNTs offer high electronic conductivity and direct electron transfer path while GONRs offer high surface area and functional groups which adsorb more Na ions on the surface therefore increasing capacity. A full cell which combines MWCNT@GONR as anode and P2-Na_xMnO_2 as cathode is assembled and exhibits a high energy density.

Acknowledgements

First of all, I deeply appreciate my supervisors, Professor Ulrich Stimming, and Professor Madhavi Srinivasan for accepting me as their doctoral student. Their encouragement, guidance and continuous support with patience and knowledge enabled me to develop an understanding of electrochemical energy storages as well as helped me to complete this thesis. I am deeply grateful for all the possibilities they provided for me, including collaborations with international research groups and sharing my research works in several international conferences.

I would like to acknowledge the financial, academic and technical support of TUM CREATE with funding by the National Research Foundation of Singapore and Nanyang Technological University, with the award of a Postgraduate Research Scholarship that provided the necessary financial support for this research.

I sincerely thank my mentors, Dr. Jochen Friedl and Dr. Grace Wee, for their thoughtful and patient supervision, encouragement and useful suggestions which helped in improving my reports and papers. I am especially grateful for their permanent willingness to help and their warmest friendship.

I would like to thank Dr. Oliver Schneider in Technische Universität München (TUM) for hosting me during my research attachment. I would also like to sincerely thank Prof. Ulrich Kortz, Dr. Rami Al-Oweini, Dr. Ali Haider, Dr. Zhengguo Lin, Dr. Wenjing Liu, and Dr. Yixian Xiang in Jocobs University, Bremen (Germany), for their help on polyoxometalate synthesis, characterization, and advice. Especially thanks Prof. Ulrich Kortz for supervision and hosting during my stay in Jacobs University as a visiting scientist. I truly appreciate to have such a fulfilling experience working with him. I sincerely thank Prof. Bing-Joe Hwang and his group members (Dr. Chun-Jern Pan, Ming-Hsien Lin, Dr. Sunny Hy, Liang-Yin Guo, Chia-Chun Hung, and Yu-Fo

Chen*)* in National Taiwan University of Science and Technology (NTUST) for In-situ XAFS measurements in National Synchrotron Radiation Research Center (NSRRC), Taiwan. Especially appreciate Prof. Bing-Joe Hwang and Dr. Chun-Jern Pan on the data analyses and valuable advices. I deeply thank Prof. Chia-Liang Sun and his student Ms. Huei-Ping Liou in Department of Chemical and Materials Engineering, Chang Gung University, Taiwan for MWCNT-GONR syntheses as well as valuable suggestions.

Thanks Prof. Harry Hoster, Prof. Rachid Yazami, Prof. Guenther Scherer, and Prof. Denis Yu for their useful advice during TUM CREATE RP1 meeting. I am very grateful for my colleagues Nicolas Bucher and Steffen Hartung for their strongly support on Na-ion-batteries projects including valuable suggestions and device fabrications. Many thanks toward to my colleague Dr. Linlin Li who helped a lot of my research projects after I left Singapore as well as her help in TEM characterizations several times. I would like to thank Dr. Yuxi Wang for his assistance in XPS characterizations, Jan Geder for his assistance in TGA-MS measurements, and Dr. Chui Ling Wong and Dr. Yan Ling Cheah for their help in TEM characterizations. I am grateful to our FYP student, Tan Kim Soon, Lee Ching Yi, Muhammad Izzat Bin Abdul Aziz, and Judith Lim Liting for helping me a lot on my research projects. I also thank Li-Chung Kin a lot on the writing advice of this thesis and confirmation report.

I am thankful for the teammates in TUM CREATE, NTU MSE, and TUM: Heryani Ahmad, Dr. Ali Rinaldi, Dr. Arun Nagasubramanian, Dr. Irina Gocheva, Dr. Shahnaz Ghasemi, Dr. Teng Yin Ting, Dr. Iulius Markovits, Dr. Olivia Wijaya, Steffen Schlueter, Max Herpich, Christoph Bauer, Dr. Tan Kim Seng, Patrick Osswald, Ramona Bucher, Dr. Tan Pei Fen, Su Tanto, Ko Yah Wen, Lee Chee Siang, Lukas Seidl, Dr. Sladjana Martens, Ludwig Asen, Wenbo Ju, Yunchang Liang for their friendship and the assistance provided in this work. I also acknowledge the help of

Hsin-Yi Wang (SCBE, NTU) for his valuable suggestions on electrochemical studies. I also appreciate the corporate team in TUM CREATE: Dr. Thomas Aulig, Dr. Bing Zou, Ms. Wendy Tham, Ms. Wai Mun Chen, Ms. Samantha Lee, Ms. Katherine Soh, Ms. Ivy Lua, Ms. Rain Teh, Ms. Marion Escasinas, Mr. Hardik Shelat, and Mr. Raymond Han for their warmly help on all the administration works such as approving finance support, travel authorization, Joint-PhD program, IT-related assistant and so on.

Lastly and most importantly, I would like to thank my parents, grandparents, and my young brother for their love, encouragement and always stand by me anytime and anywhere. I would like to thank my boyfriend, Meng-Che Tu, for encouraging and loving me and for accompanying me through my whole PhD life from Taiwan to Singapore, and from Singapore to Germany. I am looking forward to our shared journey in the future.

Table of Contents

List of Figures

List of Tables

Chapter 1 Introduction

1.1 Background

Energy storage has emerged as a key technological challenge in the field of power generation and transporting renewable energy sources. Various types of energy storage systems have been developed to store different kind of energies. Hydroelectric systems are used to store potential energy; flywheels are used to store kinetic energy; fuels store chemical energy; batteries and capacitors are used to store electrical or electrochemical energy. Tremendous effort has been focused on developing electrochemical energy storage devices such as batteries and supercapacitors (SCs) with potential applications including portable electronics, electro mobility, and large-scale stationary energy storage.[1] **Figure 1.1** shows the Ragone plot which illustrates energy density and power density for the most essential energy storage systems.

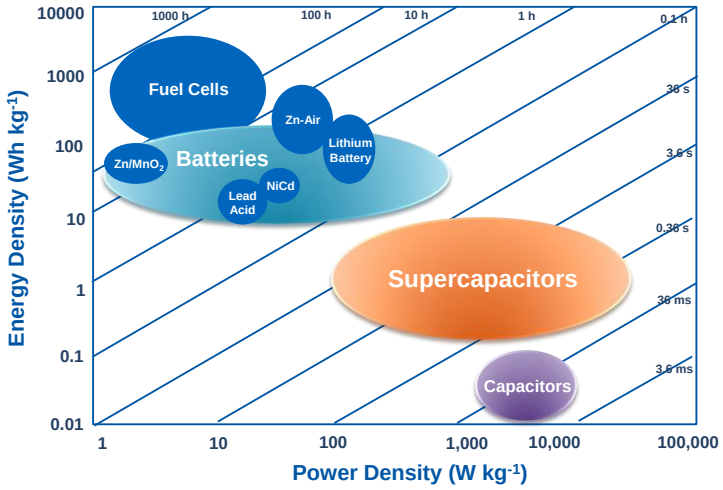

Figure 1.1 Ragone plot of various energy storage devices

1.2 Motivation and Objective

In recent years, lithium ion batteries (LIBs) have been widely used in portable electronic devices, and they are a promising means of energy storage for electric vehicles due to their high

energy density.[2] Commonly used cathode materials in LIBs are lithium intercalation compounds such as $LiCoO_2$ or $LiFePO_4$. The capacity and cycle stability are based on their relatively unchanged crystal structures during the lithium intercalation/de-intercalation process.[3] Structural changes upon lithium ion insertion into the layer-structured Li_xCoO_2 exceeding the critical composition range ($x = 0.5$) cause rapid capacity fading.[3] In addition, the charge/discharge rate of these lithium intercalation compounds is slow because of the slow kinetics during intercalation/de-intercalation of the lithium.[2]

Nowadays, LIBs are the leading energy storage technology but the scarcity of lithium (only 20 ppm in the earth's crust) and its high cost are the challenges for large-scale applications in the industry.[2,4-6] The high abundance of sodium (~ 2.5 % in the earth's crust) and potential cost advantages over LIBs enable Na-ion batteries (NIBs) be a promising candidate for large-scale energy storage.[6] Therefore, NIBs have attracted significant attention recently.

In contrast to batteries which provide high energy density but low power density, SCs can deliver high power density (> 10 kW/kg) which results in around 100 times faster charge/discharge rates than batteries.[7] In addition, SCs also have high cycle life with good stability. Therefore, they can be employed to complement or replace batteries in some energy storage applications, such as for uninterruptible power supplies, load leveling, and braking systems in electric vehicles.

Presently, activated carbon, which provides a high surface area with high double layer capacitance, is the most commonly used electrode material in commercial SCs.[8] However, activated carbon is unable to provide high power due to its low electrical conductivity as compared to other electrode materials such as fullerenes,[9] carbon nanotubes (CNTs),[10] graphene,[11] and nanofibers. Moreover, limited charge storage capability of activated carbon results in low energy density (~20 times lower than batteries) of the current SCs, which obstructs their widespread

applications such as electric vehicles and smart grid implementation. Accordingly, the development of electrode materials with high energy density and rapid charge/discharge capability is required for electric hybrid vehicles and smart grid applications. Transition metal oxides (TMOs) such as ruthenium oxide,[12] vanadium oxide,[13] and manganese oxide[14] have been widely investigated in order to improve the energy density of SCs. These TMOs are redox-active materials which can be utilized to construct pseudocapacitors and store electrochemical charge with highly reversible surface redox reactions. Although TMOs can provide high specific capacitance, their power densities and cycling life are much lower than carbon materials.[15] Hence, a new category of electrode material with long cycling life, high energy and power densities should be developed.

Polyoxometalates (POMs) are transition metal oxide molecular clusters with well-defined structures, and they have been reported to be promising electrode active materials for energy storage applications such as SCs,[7,16-21] LIBs,[3,22-24] and NIBs[25] POMs can undergo fast redox reactions and transfer multiple electrons per molecule while retaining their innate stability. The POM molecules are expected to stay as molecular crystal clusters during redox processes rather keep a continuous crystal structure, thus the stability of POM electrodes is independent of the recoverability of their crystal structure.[3,24,25] Different structures and components of POMs can be synthesized by various simple solution methods. Thus, ideal POMs as electrode materials for LIBs, NIBs, and SCs with high energy and power densities can be designed. However, the energy density and power density of POM SCs and LIBs reported so far cannot meet the commercial requirement. Thus, new POM electrode materials for SCs and LIBs will be investigated in this thesis.

Graphite is the commonly used anode material for LIBs. However, due to unfavorable thermodynamic processes, Na ions cannot intercalate into graphite reversibly.[25] Many anode materials have been investigated for NIBs, such as carbonaceous materials,[4,26,27] metal oxides/sulfides,[28,29] sodium alloys,[30,31] phosphorus,[32] and phosphides.[32] Carbon-

based materials are the most promising anode candidates for NIBs due to their low-cost, easily attainable, and environmentally friendly nature. Hard carbon,[26] expanded graphite, reduced graphene oxide (rGO),[4] and nitrogen-doped carbon fibers have been reported as potential carbon anode materials for NIBs.[27] rGO has received much attention recently because of its superior properties such as high electronic conductivity, good chemical stability, and high surface area.[33] However, the capacity in the 1st cycle is highly irreversible, and the rGO sheets restack during cycling which brings about poor capacity stability.[33] Therefore, a new nanostructured carbon material as anode for NIBs which can decrease those shortages will be proposed in this thesis.

Hence, the primary objective of this thesis is to develop novel POMs and nanostructured carbon materials which are able to satisfy the stringent performance demands of LIBs, NIBs, and SCs with high energy density (store more charge), high power density (fast charging/discharging), long cycling life (duration), and low cost. This thesis will focus on three topics:

(1) A vanadium-based POM ($Na_6[V_{10}O_{28}]$) as electrode materials for organic SCs and LIBs.

Due to the multiple oxidation states (V^{2+}~V^{5+}) of vanadium, V-based POMs SCs are identified as potential electrode materials which might provide high specific capacitance and high energy density with multiple redox reactions. In LIBs systems, V-based POM materials (polyoxovanadates) also show high capacity and long cycling stability.[3,22,24] Thus we will focus on V-based POMs as electrode materials for SCs and LIBs.

(2) A nanostructured carbon material (singe-wall carbon nanotube, SWCNT) and POM ($([(CH_3(CH_2)_3)_4N]^+)_5[PV^V_2Mo^{VI}_{10}O_{40}]$ (**TBA-PV_2Mo_{10}**)) hybrid as electrode material for aqueous SCs.

In this **SWCNT-TBA-PV_2Mo_{10}** hybrid material, **TBA-PV_2Mo_{10}** offers redox activity while the TBA organic groups help to preventing dissolution in the aqueous electrolyte in order to increase

the cycling stability, and SWCNTs offers high electrical conductivity with high double-layer capacitance that are proposed to improve both energy and power density.

(3) A novel nanostructured carbon material, core–shell structure with multi-walled carbon nanotubes (MWCNTs) as the core and graphene oxide nanoribbons (GONRs) as the shell (MWCNT@GONR) with functional groups as anode material for NIBs.

MWCNT@GONR provides unique core-shell structure consisting of MWCNTs between flat GONR sheets to avoid the restacking problem of graphene and ease the penetration of the electrolyte.

In this work, V-containing POMs $Na_6[V_{10}O_{28}]$, $([(CH_3(CH_2)_3)_4N]^+)_5[PV^V_2Mo^{VI}_{10}O_{40}]$ (**TBA-PV_2Mo_{10}**), and SWCNT-TBA-PV_2Mo_{10} will be synthesized by a simple solution method. MWCNT@GONR will be synthesized by unzipping the MWCNTs with microwave assistance. Above materials will be characterized by Fourier transform infrared spectroscopy (FT-IR), nuclear magneticr spectroscopy (NMR), thermo gravimetric analysis (TGA), Brunauer-Emmet-Teller (BET) surface area measurement, field-emission scanning electron microscopy (FESEM), and high resolution transmission electron microscopy (HRTEM), X-ray diffraction (XRD), X-ray photoelectron spectrometer (XPS), and Raman. The SC and battery performance whit those electrode materials will be analyzed by cyclic voltammetry (CV) and galvanostatic charge/discharge (GCD). Furthermore, advanced techniques such as in-situ X-ray absorption spectroscopy will be used to determine how many charges can be stored in the $Na_6[V_{10}O_{28}]$ electrode. For high power density studies, the fundamental kinetic studies will be investigated with potential step methods.

1.3 Thesis Organization

The thesis is organized as follows: Chapter 2 briefly introduces the configuration and operating principles of SCs, LIB, and NIBs. A brief literature review of the current electrode materials employed as well as their application in SCs, LIBs, and NIBs is presented. Chapter 3 describes the various techniques employed in this thesis including material synthesis and characterization, device fabrication, electrochemical characterization as well as methods of fundamental studies. Chapter 4 details the experimental results followed by its discussion in Chapter 5. The discussion explores the charge storage mechanism of $Na_6[V_{10}O_{28}]$, SWCNT-TBA-PV_2Mo_{10} , and MWCNT@GONR electrodes in SCs LIB, and NIBs. Chapter 6 reaches the conclusion of the whole research project and recommendations for future studies in Chapter 7.

Chapter 2 Literature Review

2.1 Supercapacitors (SCs)

2.1.1 Basic Principles of SCs

Supercapacitors are energy storage devices which provide higher power density and longer cycling stability as compared to batteries. A SC device consists of active material, current collector, electrolyte and separator. The mechanism of SCs can be divided into two types: (1) electrochemical double layer capacitance and (2) pseudocapacitance as shown in Figure 2.1. The formation of electrostatic forces at the interface between the charged surface of an electrode and the ions in the electrolyte provides electrochemical double layer capacitance. Other than direct electrostatic forces, the fast and reversible Faradaic redox reactions at the electrode surface provide pseudocapacitance. The following sections will discuss these two mechanisms in detail.

Electrochemical double layer capacitance can be obtained when charges separate at the interface between electrode and electrolyte by polarization as shown in **Figure 2.1 (a)**. The double layer capacitance (C) can be described as follows:

$$C = \frac{\varepsilon_r \varepsilon_0 A}{d} \tag{2.1}$$

where ε_r is the dielectric constant of electrolyte, ε_0 is the dielectric constant of the vacuum, A is the surface area of the electrodes, and d is the distance of charge separation. The power density of SCs is better than batteries due to the faster electrochemical kinetics, which are not limited by a polarization resistance that enables fast energy uptake and delivery at the surface. The cycling stability of SCs with electrochemical double layer charge storage mechanism (up to millions of cycles) is much better than batteries (only few thousand cycles) because no Faradic reactions occur and no irreversible changes are experienced in SC active materials during the charge/discharge process. However, the energy density of SC devices is limited by the electrostatic surface charging

mechanism. As shown in **Figure 2.2**, a rectangular shaped cyclic voltammogram of a two-electrode SC cell indicates a pure electrochemical double layer capacitance mechanism. According to the following equation, the capacitance can be calculated:

$$I = C \times \frac{dV}{dt} \tag{2.2}$$

where I is the current, (dV/dt) is the scan rate of potential, and C is the electrochemical double layer capacitance.

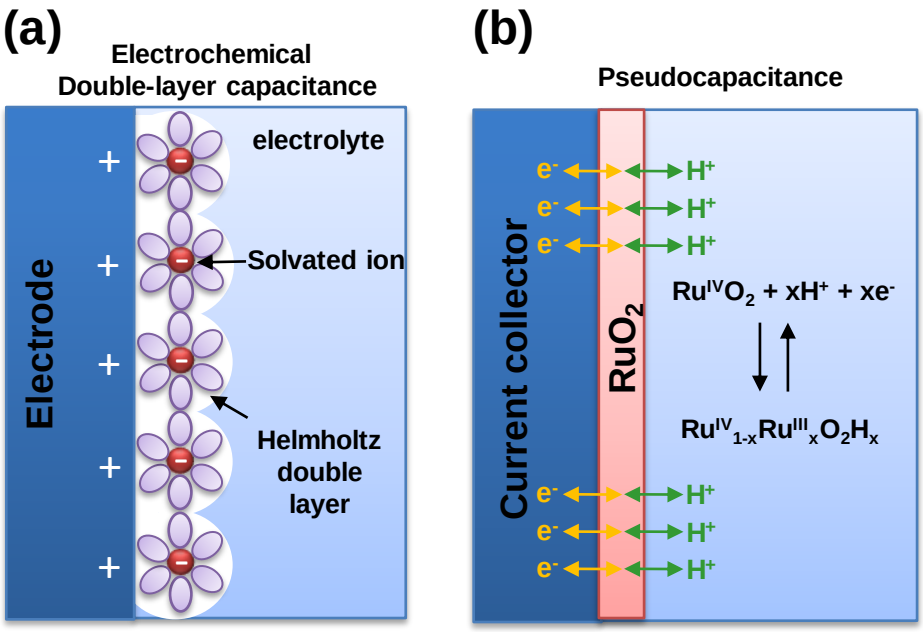

Figure 2.1 Schematic of two different charge storage mechanisms via (a) electrochemical double-layer capacitance (EDLC) or (b) redox reactions based pseudocapacitance.[34]

Pseudocapacitance is described as fast and highly reversible Faradaic redox reactions at the surface of active materials (electrodes) as shown in **Figure 2.1 (b)**. As illustrated in **Figure 2.2**, the redox peaks deviating from the ideal rectangular cyclic voltammogram indicate a Faradaic reaction. Slower kinetics of the pseudocapacitance during charging can be observed from the current delay upon the reversal of the potential sweep.

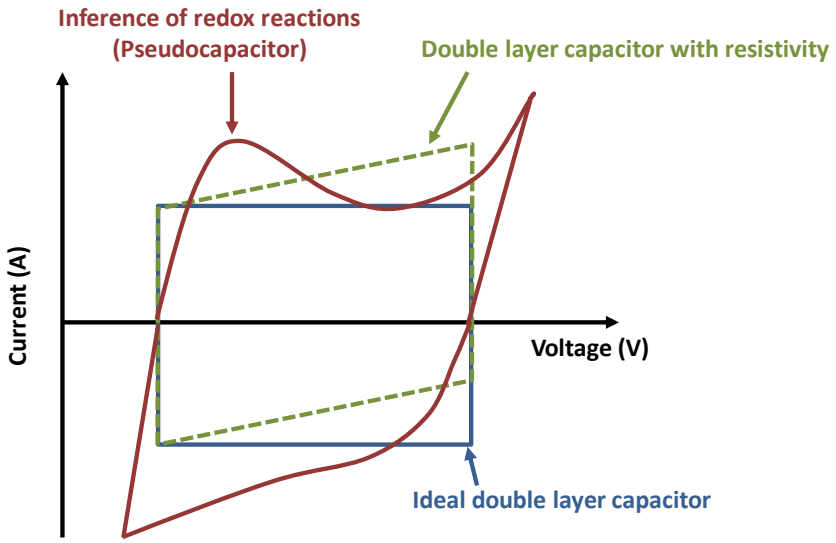

Figure 2.2 Typical cyclic voltammograms of supercapacitors[35]

The definition of energy density is the amount of charges that can be stored in SCs, and power density is how fast the charges stored in SCs can be released during discharge. Energy density, average power density, and maximum power density obtained during the discharge can be calculated from the following expressions:

$$E = \frac{1}{2}CV^2 \tag{2.3}$$

$$P_{ave} = \frac{E}{\Delta t} \tag{2.4}$$

$$P_{max} = \frac{V^2}{4R} \tag{2.5}$$

where C is the capacitance (F), V is the voltage window (V), t is the discharging time (h), and R is the device resistance (Ω).

2.1.2 Electrolytes for Supercapacitors

The selection of electrolytes could determine the performance of SCs. According to Equation 2.3 ($E = \frac{1}{2}CV^2$), the energy density of SC is proportional to the square of the voltage, which is limited by the electrochemical potential window of the electrolyte. According to Equation 2.5

($P_{max} = \frac{V^2}{4R}$), the power density is inversely proportional to the equivalent series resistance (ESR) of the SC device which is dominated by the conductivity of the electrolyte. Thus, electrolytes with low resistivity, high stability, and wide electrochemical potential window are important for SC studies. The electrolytes for SCs can be divided into two categories: liquid and solid electrolytes. In this thesis we concentrate on the two types of liquid electrolytes include aqueous and organic electrolytes.

Acids (e.g., H_2SO_4), alkalis (e.g. KOH), and neutral salt solutions (e.g. Na_2SO_4) are commonly used aqueous electrolytes in SCs. These electrolytes provide high ionic conductivity up to 1 Scm^{-1}, low cost and are simple to prepare. Compared to non-aqueous solutions, aqueous electrolytes provide a higher dielectric constant that can help achieve higher specific capacitance in high surface-area carbons.[36] However, the low electrolysis potential of ~1.23 V limits the voltage range of aqueous electrolytes and restricts the operating voltage < 1 V of SCs.[37]

Using organic electrolytes, the cell voltage window can be widened to 3 V; this results in higher energy density SCs.[37,38] Organic electrolyte mixtures such as $LiClO_4$ and $AlCl_3$ dissolved in propylene carbonate (PC) or acetonitrile (ACN) have been commonly used in commercial SCs. PC has lower toxicity and evaporating temperature and makes it more popular than ACN. However, high electrical resistivity of organic electrolytes, which is at least one order of magnitude higher than aqueous electrolytes, causes high internal resistance.

2.1.3 Electrode Materials for SCs

High specific surface area, good conductivity in porous matrices, and good electrolyte accessibility to pore surface area are required to obtain high capacitance in SCs [35]. Various electrode materials have been developed for SCs including carbon materials, electroconducting polymers, transition metal oxides, and polyoxometalates. Carbon materials, which have high

surface areas, produce high electrochemical double layer capacitance. Redox-active materials such as electroconducting polymers, transition metal oxides, and polyoxometalates which are known as pseudocapacitors, can provide pseudocapacitance through highly reversible surface redox reactions. These materials will be discussed in detail in the following sections.

Activated carbon (AC) is the most commonly used electrode material in commercial SCs. It has a high surface area (1000—3500 $m^2 g^{-1}$) which provides high double layer capacitance from 27.9 to 140 F g^{-1}.[8,39] However, AC has lower electric conductivity than graphitic carbon which can only be overcome by high temperature treatment (above 700 °C) to form conjugated sp2 carbon during carbonization.[40]

Other nanostructured carbon materials such as fullerenes,[9] nanofibers, carbon nanotubes (CNTs),[10] and graphene[11] and have been investigated for SCs applications. Egashira et al. reported a capacitance of 58 F g^{-1} of fullerenes with high rate stability and electronic conductivity.[9] The specific capacitance of graphene has been reported from 100 to 205 F g^{-1} with a high theoretical surface area of 2630 $m^2 g^{-1}$.[11,41-43] CNTs have been widely investigated as electrode materials for SCs due to their high electrical conductivity (ranging from 103 S m^{-1} for multi-walled carbon nanotubes (MWCNTs) to 108 S m^{-1} for single-walled carbon nanotubes (SWCNTs))[44,45] and a high surface area. The specific capacitances of MWNTs and SWNTs were reported from 49 to 120 F g^{-1} and from 20 to 300 F g^{-1}, respectively.[39,46,47] However, the limited charge storage capability of carbon materials brings on low energy density of SCs. Therefore, other electrode materials such as elctroconducting polymers and transition metal oxides are used to improve the energy density of SCs by their pseudocapacitance.

Electroconducting polymers (ECPs) such as polyaniline (PAni), polypyrrole (PPy), polythiophene (P3HT), and their derivatives provide higher electrical conductivity as compared to metal oxides and have been widely studied as electrode materials for SCs. These ECP materials

are inexpensive, have suitable morphology, and can be easily manufactured into SCs.[48] During charge-discharge processes, ECPs provide high doping-undoping rates related to the π-conjugated polymer chains that produce high pseudocapacitance (up to 150 F g^{-1}) and energy density.[39,49] However, swelling and shrinking of ECPs during charging/discharging process cause the poor long-term stability and limits the applications of ECPs as SC electrodes.[48]

Transition metal oxides (TMOs) are also promising candidate electrode materials for SCs with their pseudo capacitive behavior and higher stability as compared to ECPs. RuO_2 with high specific capacitance, high conductivity, long-term cycling stability, and high electrochemical reversibility, is the most promising electrode material among TMOs.[48] The high specific capacitance of RuO_2 prepared by sol-gel method approached 977 F g^{-1}. [50] However, the cost of ruthenium is high due to its scarcity, limiting the commercial applications for RuO_2 SCs. Alternative cheaper materials such as MnO_2, NiO, V_2O_5, In_2O_3, and SnO_2 have been investigated. More attention has been focused on MnO_2 as the potential candidates for SCs due to its low-cost, high specific capacitance, and its environmentally friendly nature.[50] The capacitance performance for both carbon-based EDLC electrodes and pseudocapacitor electrodes are shown in **Figure 2.3**.

Polyoxometalates (POMs) are a large family of transition metal oxide clusters with well-defined structures. They have fast and reversible multi-electron redox reactions which lead to high capability for charge storage in batteries and capacitors.[7,12,51-57] POMs are formed by numbers of transition metal centers such as V, Mo, and W, coordinated by bridging oxygen atoms. POMs are able to undergo fast and reversible redox reactions making them promising active materials for molecular electronics, biomedical devices, sensing, and energy storage applications.[7,12,51,52]

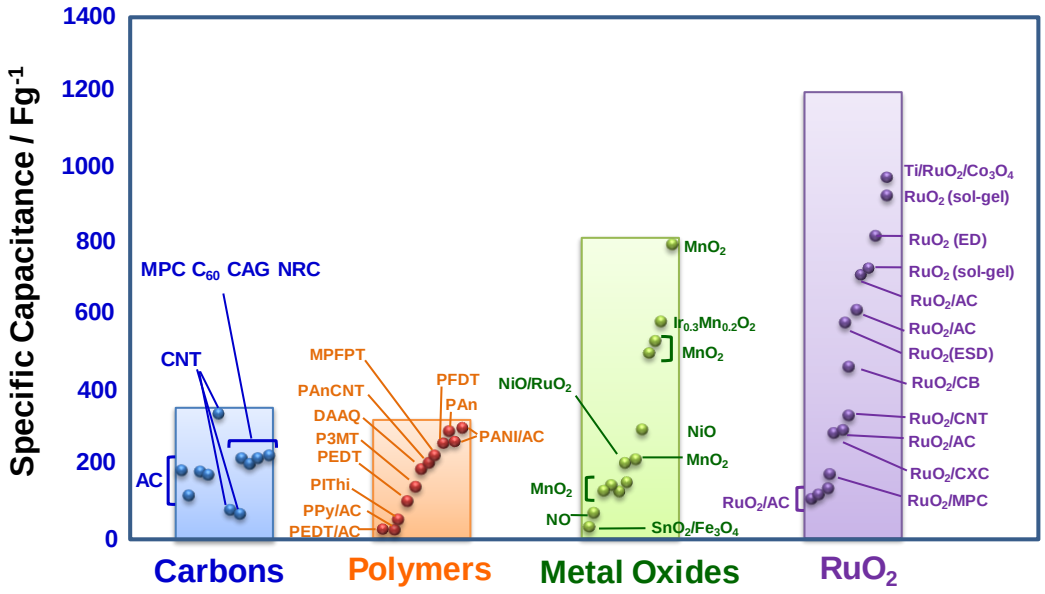

Figure 2.3 The capacitance performance for both carbon-based EDLC electrodes and pseudocapacitor electrodes (including transition metal oxides and conducting polymers) [34]

The diversity of structured of POMs can be generally classified into two categories: Isopolyanions and Heteropolyanions. Isopolyanions consist of a single type of high valence transition metals (V^{5+}, Nb^{5+}, Ta^{5+}, Mo^{6+} and W^{6+}) and are composed of a dense cluster of edge sharing octahedral. Two typical structures of isopolyanions, $[Mo_6O_{19}]^{2-}$ and $[V_{10}O_{28}]^{6-}$, are shown in **Figure 2.4 (a)** and **(b)**, respectively. . Heteropolyanion consist of addenda atoms (eg. V, Mo, W) and heteroatoms (eg. P, Si). **Figure 2.4 (c)** and **(d)** show the Keggin and Wells-Dawson structures which are the most studied structures of POMs.

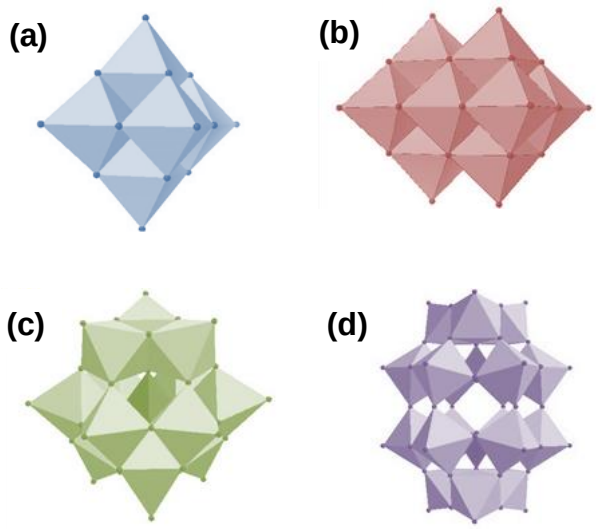

Figure 2.4 Structures of some typical POMs. Isopolyanions: (a)$[Mo_6O_{19}]^{2-}$, and (b) $[V_{10}O_{28}]^{6-}$. Heterpolyanions: (c) Keggin-type $[XM_{12}O_{40}]^{3-/4}$;(d) Wells-Dawson type $[X_2M_{18}O_{62}]^{n-}$

Several studies of POMs as electrode materials for SCs have been reported shown in **Table 2.1**. POM materials with a Keggin-type structure, $[XV_nMo_{12-n}O_{40}]^{m-}$ (X= P or Si; n= 0−3), were studied in SCs: $H_3PMo_{12}O_{40}$,[52,58-61] $Cs_3PMo_{12}O_{40}$,[18] $H_5PV_2Mo_{10}O_{40}$,[59] $H_3PW_{12}O_{40}$,[19] $H_4SiMo_{12}O_{40}$,[60] $H_4SiW_{12}O_{40}$,[17] and most of them were combined with carbon materials such as CNTs[18,60] and AC,[61] or ECPs such as polyaniline (PAni),[17] poly(3, 4-ethylenedioxythiophene) (PEDOT),[59] poly(diallyldimethylammonium) chloride (PDDA),[60] and pyrrole (PPy)[58] to prevent the dissolution of the POMs into the aqueous electrolytes and enhance the electrical conductivity. Those POMs are electrochemically active and stable in the acidic, aqueous electrolytes. POM/Carbon hybrid materials combine double-layer capacitance mainly from carbon materials and psudocapacitance mainly from POM materials with their redox activity. In POM/conducting polymer hybrid materials, POMs provide redox activity while benefiting from the conducting properties and polymeric nature of the polymers.

A. Yamada et al. demonstrated an inexpensive SC system with an asymmetric configuration: $H_3PMo_{12}O_{40}$•nH_2O/Nafion 117/H_xRuO_2•nH_2O. To prevent the POM electrode from dissolving into the aqueous electrolyte, a proton-conducting polymer electrolyte (Nafion 117) was used to improve the chemical stability. The specific capacitance of this asymmetric SC is 112 F/g and the energy density is 36 J/g with an operating voltage of 0.8 V at current density of 2.2 mA cm^{-2}.[52] J. Vaillant et al. reported an insoluble hybrid material PAni/$H_3PMo_{12}O_{40}$ with the aid of H_2O_2, showing almost no decay with a value of 90 F g^{-1} when cycling from 0 to 1 V for 200 cycles [62]. An asymmetric SC with PPy/$H_3PMo_{12}O_{40}$ as positive electrode and PEDOT/$H_3PW_{12}O_{40}$ as negative electrode in a 0.5 M H_2SO_4 aqueous electrolyte was studied by G. M. Suppes et al. This PPy/$H_3PMo_{12}O_{40}$//PEDOT/$H_3PW_{12}O_{40}$ asymmetric SC exhibited a device capacitance of 31 F g^{-1} with a maximum energy density of 4 Wh kg^{-1} and a power density of 103 W kg^{-1}. [19]

So far, sonication and layer-by-layer (LbL) deposition methods have been used to prepare POM/Carbon hybrid materials for SCs.[7,18,60,61,63] V. Ruiz et al. prepared an AC/$H_3PMo_{12}O_{40}$ hybrid material by sonicating a $H_3PMo_{12}O_{40}$ solution with AC powder, which bring on adsorption of the $H_3PMo_{12}O_{40}$ onto the surface of AC. The specific capacitance of this AC/$H_3PMo_{12}O_{40}$ symmetric SC exhibits 183 F g^{-1} at a current density of 2 A g^{-1} with a good cyclability (9 % capacitance loss after 8000 cycles).[61] MWCNTs/POM hybrid materials were also prepared by sonication method with several purification steps.[18,63] Skunik, et al. reported MWCNTs/$H_3PMo_{12}O_{40}$ hybrid materials which provided specific capacitance of 40 F g^{-1} at a current of 7 mA.[63] CNTs/$Cs_xPM_{O12}O_{40}$ hybrid materials as electrode material for symmetric SCs with a Nafion 117 membrane previously activated with a sulfuric acid dissolution as solid electrolyte reported by Cuentas-Gallegos et al. It showed high specific capacitance of 285 F g^{-1} and high energy density of 57 Wh kg^{-1} at a current density of 0.2 A g^{-1} with a reduction ~ 16 % of initial capacitance after 500 cycles. However, the specific capacitance exhibited was only 20 F g^{-1} and energy density of 12.5 Wh kg^{-1} at current

density of 2 A g^{-1}.[18] By using the sonication method, single POM molecules are generally adsorbed at defect sites and form monolayers.[18,63] Because of the high solubility of POMs in aqueous solution, excess POM molecules are washed out or dissolved in the aqueous electrolyte. Furthermore, the amount of chemisorbed POMs is also dependent on the functionalization degree of the carbon materials.[18,63]

The other simpler way to prepare POM/Carbon hybrid material is LbL deposition method. It alternates electrostatic adsorption of cationic polymer (ex. poly(diallyldimethylammonium) chloride, PDDA) and anionic POMs on functionalized carbon materials.[7,60,64] Nevertheless, the long polymer chain might block electron hopping from POM to SWCNT.

However, the specific capacitances of these POM SCs are not as high as TMO SCs. Therefore, new POM electrode materials for SCs should be developed.

Table 2.1 Summary table of supercapacitor with POM electrodes. (Reproduced from my published paper by permission of The Royal Society of Chemistry.[21])

Electrode	Electrolyte/ Membrane	Device	Current density/ scan rate	Specific capacitance	Cycle no. (retention)	Ref
$H_3PMo_{12}O_{40}$//H_xRuO_2	Nafion 117	Asymmetric device	2.2 mA cm^{-2}	112 F g^{-1}	-	52
$H_3PMo_{12}O_{40}$/PAni[a]	poly(2,5-benzimidazole)	Symmetric device	0.125 mA cm^{-2}	195 mF cm^{-2}	2000^{th} (~85%)	16
$H_3PMo_{12}O_{40}$/PAni	Nafion 117	Symmetric device	0.4 A g^{-1}	168 F g^{-1}	200^{th} (~60%)	62
$H_3PMo_{12}O_{40}$/PAni	Nafion117+acid	Symmetric device	0.4 A g^{-1}	110 F g^{-1}	4000^{th} (~68%)	17
$H_3PMo_{12}O_{40}$/PPy[b]	0.1 M H_2SO_4	3-electrode configuration	1 mV s^{-1}	130 F g^{-1}	-	58
$H_3PMo_{12}O_{40}$/PPy	Nafion 115	3-electrode configuration	1 mV s^{-1}	22.9 F g^{-1}	-	65
$H_5PV_2Mo_{10}O_{40}$/PPy	0.1 M H_2SO_4	3-electrode configuration	1 mV s^{-1}	422 F g^{-1}	-	58
$H_5PV_2Mo_{10}O_{40}$/PPy	Nafion 115	3-electrode configuration	1 mV s^{-1}	27.6 F g^{-1}	-	65
$H_4SiMo_{12}O_{40}$/PPy	0.1 M H_2SO_4	3-electrode configuration	1 mV s^{-1}	266 F g^{-1}	-	58
$H_4SiMo_{12}O_{40}$/PPy	Nafion 115	3-electrode configuration	1 mV s^{-1}	33.4 F g^{-1}	-	65
$H_3PMo_{12}O_{40}$/PPy// $H_3PW_{12}O_{40}$/PEDOT[c]	0.5 M H_2SO_4	Asymmetric device	1 mA	31 F g^{-1}	200^{th} (~68%)	19
$H_3PMo_{12}O_{40}$/PEDOT	0.1 M H_2SO_4	3-electrode configuration	10 mV s^{-1}	140 F g^{-1}	-	59
$H_5PV_2Mo_{10}O_{40}$/PEDOT	0.1 M H_2SO_4	3-electrode configuration	10 mV s^{-1}	70 F g^{-1}	-	59
$Cs_xPMo_{12}O_{40}$/MWCNT	Nafion 117+acid	Symmetric device	0.2 A g^{-1}	285 F g^{-1}	500^{th} (~65%)	18
$H_3PMo_{12}O_{40}$/MWCNT	1 M H_2SO_4	Symmetric device	1 A g^{-1}	38 F g^{-1}	-	63

$H_3PMo_{12}O_{40}$/PDDA/ Carbon Nanoparticles	1 M H_2SO_4	3-electrode configuration	5 V s^{-1}	0.6 F cm^{-2}	-	[7]
$H_3PMo_{12}O_{40}$/PDDA[d]/ MWCNT	1 M H_2SO_4	3-electrode configuration	50 mV s^{-1}	2.68 F cm^{-2}	-	[60]
$H_3PMo_{12}O_{40}$/PDDA/ MWCNT	1 M H_2SO_4	3-electrode configuration	50 mV s^{-1}	1.93 F cm^{-2}	-	[60]
$H_3PMo_{12}O_{40}$+$H_4SiMo_{12}O_{40}$/ PDDA/MWCNT	1 M H_2SO_4	3-electrode configuration	10 mV s^{-1}	2.4 F cm^{-2}	-	[64]
$H_3PMo_{12}O_{40}$+$H_5PV_2Mo_{10}O_{40}$/ PDDA/MWCNT	1 M H_2SO_4	3-electrode configuration	50 mV s^{-1}	158 F cm^{-3}	-	[66,67]
$H_3PMo_{12}O_{40}$/AC	1 M H_2SO_4	Symmetric device	1 A g^{-1}	140 F g^{-1}	8000^{th} (~91%)	[61]

[a] PAni: polyaniline [b] PPy: polypyrrole [c] PEDOT: poly(3,4-ethylenedioxythiophene) [d] PDDA: poly(diallyldimethylammonium) chloride

2.1.4 The research scope of POM SCs in this thesis

In order to increase the energy density of POM SCs with long cycling life, V-containing POMs will be synthesized and test in this thesis. Based on the performance of transition metal oxides in SCs, V_2O_5 provides relatively high specific capacitance due to its multiple oxidation states (V^{2+}~V^{5+}). Hence, Vanadium-containing POMs are identified as potential electrode materials which might provide high specific capacitance and high energy density in this study. In this work, V-containing POMs $Na_6[V_{10}O_{28}]$ and $([(CH_3(CH_2)_3)_4N]^+)_5[PV^V_2Mo^{VI}_{10}O_{40}]$ (**TBA-PV_2Mo_{10}**) will be synthesized by a simple solution method, and characterized.

POM electrodes have been reported to be unstable in aqueous liquid electrolyte due to high solubility of the molecules [52]. Different POMs have different solubility in aqueous and organic electrolytes. Thus, the selection of POMs for certain electrolytes is important. In our study, $Na_6[V_{10}O_{28}]$ can be dissolved in aqueous electrolyte but is insoluble dissolved in organic electrolyte. Thus, we choose a Li-ion-containing organic solution (1 M $LiClO_4$ in propylene carbonate (PC)) as an electrolyte for $Na_6[V_{10}O_{28}]$ SCs, and an acidic aqueous electrolyte (1 M H_2SO_4) for $(TBA)_5[PV_2Mo_{10}O_{40}]$ (**TBA-PV_2Mo_{10}**, TBA: $[(CH_3(CH_2)_3)_4N]^+$, tetra-n-butyl ammonium) SCs. **TBA-PV_2Mo_{10}** is insoluble in aqueous electrolyte because of its organic cation (TBA). Thus, high cycling stability in acidic aqueous electrolyte is expected. POMs are metal

oxide clusters with low electronic conductivity. In this study, a nanostructured carbon material, SWCNT, will be employed to improve the electronic conductivity thus enhance the power density and specific capacitance of POM SCs.

2.2 Li-ion batteries (LIBs)

In 1970s, primary LIBs were commercialized for the first time.[68] Since then, many researchers have focused on developing rechargeable LIBs such as Li-TiS_2, Li-MoS_2 and Li-LixMnO_2 systems. However, safety issues and short lifetime of those systems limited their commercial applications. During the 1980s, Yazami[69] and Goodenough[70] made a breakthrough in rechargeable LIB research by utilizing graphite (Li_xC_6) and lithium cobalt oxide ($LiCoO_2$) as anode and cathode materials respectively. This resulted in the first commercialized LIBs in 1991 by Sony Corporation. Nowadays, the graphite-$LiCoO_2$ LIB system is used to store electronic charges for most electronic devices such as the cellphones, laptops and digital cameras.

LIB has a higher working voltage (~3.7 V) and higher gravimetric energy density than other secondary battery systems, such as lead acid and Nickel-cadmium batteries.[71] LIBs cannot utilize an aqueous electrolyte because of the high voltage and presence of Li ions. Hence, organic solvents such as ethylene carbonate (EC), diethyl carbonate (DEC), propylene carbonate (PC), and dimethyl carbonate (DMC) with large potential windows are common utilized in LIBs. Furthermore, LIBs do not suffer from the memory effect, which is the drawback of nickel-cadmium (Ni-Cd) batteries.

2.2.1 Basic Principles of LIBs

The conventional LIB consists of a layer-structured $LiCoO_2$ cathode, a graphite anode and an organic lithium-containing electrolyte such as $LiPF_6$ in EC/DEC as shown in **Figure 2.5**. LIBs operate mainly by intercalation and deintercalation of Li ions. During charging, Li ions are

deintercalated from the cathode and inserted into the anode through the lithium-containing organic electrolyte, while the electrons are transferred through the external circuit from cathode to the anode. Conversely, Li ions are released from the anode and intercalate back into the cathode during discharging. During charge/discharge processes, LIB converts the chemical energy into electricity and stores the electrical energy in the battery by transporting Li ions between anode and cathode through the organic electrolyte. The chemical reactions can be summarized in the equations below:[72]

$$\text{Cathode: } LiCoO_2 \leftrightarrow Li_{0.5}CoO_2 + 0.5Li^+ + 0.5e^- \quad (2.5)$$

$$\text{Anode: } C_6 + xLi^+ + xe^- \leftrightarrow Li_xC_6 \quad (2.6)$$

The operating principle of LIBs strongly relies on the intercalation and deintercalation of Li ions into the electrodes. Thus, the selection of electrode materials is critical. The commonly used cathode material, $LiCoO_2$ only enables deintercalation of up to 0.5 Li per $LiCoO_2$ as shown in Equation 1, results in a theoretical specific capacity of 135 mAh g^{-1}. In the other side, graphite anode can intercalate 1 mole of Li ion per mole of graphite which leads to a theoretical capacity of 370–372 mAh g^{-1}. The mismatched specific capacities between cathode and anode give rise to an increased mass of cathode for the purpose of achieving higher efficiency in batteries. Hence, the overall energy density of the commercial LIBs is limited by the specific capacity of cathodes. Therefore, an alternative cathode with higher specific capacity is necessary for high-performance LIBs.

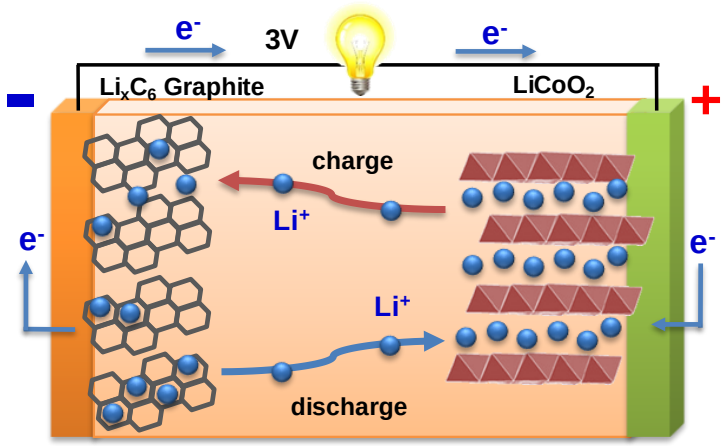

Figure 2.5 Schematic illustration of a LIB which consists a graphite anode, $LiCoO_2$ cathode, and a Li-conducting organic liquid electrolyte.[73]

2.2.2 Cathode Materials for LIBs

Commonly used cathode materials in LIBs are lithium intercalation compounds, including layered lithium metal oxides such as $LiCoO_2$, layered integral materials such as Li_2MnO_3 and $LiMnO_2$, and olivine phosphates such as $LiFePO_4$. Those cathode materials are electrochemically active via lithium intercalation/deintercalation into and out of their respective layered/framework structures. The capacity and cycle stability are dependent on their crystal structures during the lithium intercalation/de-intercalation process.[3] $LiCoO_2$ has working voltage of 3.6-4 V with high theoretical capacity of ~274 mAh g^{-1}. However, over-release of Li ions ($x < 0.5$) from the layer-structured Li_xCoO_2 causes irreversible structural changes and results in rapid capacity fading.[3] Thus, only half of theoretical capacity is achieved practically (~135 mAh g^{-1}). Furthermore, $LiCoO_2$ is highly expensive and toxic. $LiMn_2O_4$ has good structural stability but the dissolution of Mn^{2+} ions into the electrolyte from the cathode lattice restricts the practical applications on a large scale. [YL4, 5, 56] Framework structured cathode materials olivine phosphates such as $LiFePO_4$ (theoretical capacity 170 mAh g^{-1}) and $LiMnPO_4$ (theoretical capacity 171 mAh g^{-1}) exhibit good structural stability, good safety, low cost, and environmental friendliness advantages. Nevertheless,

the low conductivity of these cathode materials lowers their performance in lithium ion batteries. Furthermore, the charge/discharge rate of those lithium intercalation compounds is slow due to the slow kinetics during intercalation/de-intercalation of the lithium.[2]

Organic radical materials that do not rely on lithium intercalation have been developed as cathode materials for LIBs. In these, stable organic radicals (e.g. nitroxyl) in organic polymers act as redox active sites.[2,3,74,75] Lithium ions desorption and adsorption onto the organic radical material surface during charge/discharge process is independent of the crystal structure; their electrochemical reactions are faster than lithium intercalation compounds which lead to better high rate performance. However, their capacities (ca. 120 mAh g^{-1}) are lower than for typical lithium intercalation compounds (ca. 150 mAh g^{-1}) due to their high molecular weight (ca. 200 g Mol^{-1}) and limited redox sites.[2,74] Moreover, the stability of the organic electrode materials is a concern.[3,75]

POMs have been reported as promising cathode active materials for LIBs recently due to their ability to undergo fast redox reactions and transfer multiple electrons per molecule.[3,22,23,51,75-81] They are expected to exhibit a lithium storage mechanism in between the ones described for lithium intercalation materials and organic radical materials.[75] electrode active materials for energy storage applications such as SCs,[7,16-21] LIBs,[3,22-24] and NIBs[25]. POMs can undergo fast redox reactions and transfer multiple electrons per molecule while attaining their innate stability. The POM molecules are expected as a molecular cluster during redox process rather than a continuum, thus the stability of POM electrodes is independent from the recoverability of their crystal structure.[3,24,25] The commonly used POMs as electrode materials in LIBs are Keggin-type Mo-based POMs including $TBA_3[PMo_{12}O_{40}]$ (TBA=$[N(CH_2CH_2CH_2CH_3)_4]^+$), $K_3[PMo_{12}O_{40}]$, and $K_4[SiMo_{12}O_{40}]$. $TBA_3[PMo_{12}O_{40}]$ can store up to 24 electrons in each molecule results in high capacity of ca. 270 mAh g^{-1}. However, the cycling stability is poor of Mo-based POMs because of

the instability of molecular cluster ions $[PMo_{12}O_{40}]^{3-}$ in the reduced state and the dissolution of TBA-POMs into the organic electrolytes. Moreover, less than 30 wt % of Mo-based POMs was used as active material in the electrode which decreases the energy density of the practical devices.[81] Vanadium-based POMs have been reported by N. Sonoyama and his group, including $(KH)_9[PV_{14}O_{42}]$,[22] $K_7[NiV_{13}O_{38}]$,[3] and $K_7[MnV_{13}O_{38}]$,[24] which exhibit high capacity (up to 200 mAh g^{-1}) and higher cycling stability than Mo-based POMs. N. Sonoyama and his group reported a discharge–charge reaction mechanism of $K_7[NiV_{13}O_{38}]$ based on the results from ex situ XRD and ex situ FT-IR measurements as shown in **Figure 2.6**.[3] During first discharge process, the lithium ion inserts into the $K_7[NiV_{13}O_{38}]$ cathode and the crystal structure of $K_7[NiV_{13}O_{38}]$ becomes to amorphous. In the following charge and discharge cycles, $K_7[NiV_{13}O_{38}]$ remains in a stable amorphous state. The reactions between $[NiV_{13}O_{38}]^{7-}$ molecular cluster ion and lithium ion are reversible and independent from the recoverability of crystal structure.[3] Nevertheless, low ratio of active material (less than 32 %) in the electrodes still restricts the applications for actual devices.

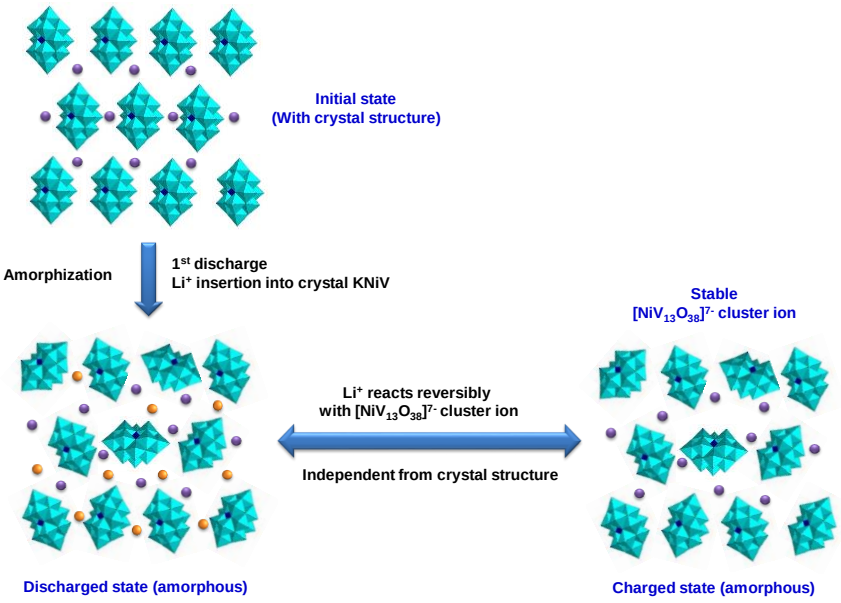

Figure 2.6 Schematic illustration of the discharge–charge reaction mechanism for $K_7[NiV_{13}O_{38}]$ cathode. [3]

2.2.3 In-situ X-ray absorption fine structure (XAFS) measurement of POM LIB electrodes

In-situ X-ray absorption fine structure (XAFS) spectroscopy is a powerful technique which can provide insights into variation of local structures and oxidation states during cycling of batteries.[2,23,82] The XAFS spectra contain the X-ray absorption near-edge structure (XANES) and the extended X-ray absorption fine structure (EXAFS). For battery applications, XANES can be used to detect what oxidation states are involved and how many of the transition metal ions undergo changes. EXAFS are utilized to detect how the molecular structure changes during the charging/discharging by analyzing the local structures surrounding the detected atoms. H. Wang et al. reported an in-situ Mo K-edge XAFS measurements on a Keggin-type POM, $TBA_3[PMo_{12}O_{40}]$, employed in LIBs and found a 24-electron reduction during the discharging processes.[23] It showed that all 12 Mo^{VI} ions can be reduced to Mo^{IV} which results in high specific capacity up to ca. 270 mAh g^{-1}. Nevertheless, the valence and structural changes of V-based POMs in the battery reaction have not yet been investigated so far.

2.2.4 Kinetic studies of LIB electrodes

Chidsey's method was widely utilized in surface-bound redox systems for electrode-electrolyte interfaces. The reaction rates can be extracted by fitting the linear relationship in the Tafel plots which are generated from potential-step chronoamperometry experiments.[83] The following equation is a simple exponential decay which is used to fit the transient current generated from a potential step:[84]

$$I = e\Gamma k_{app} \exp(-k_{app} t) \quad (2.7)$$

where Γ is the coverage of the electrode and k_{app} is the single decay rate representing the rate of reactant consumption. However, the above equation is utilized only for flat electrodes with uniform reaction rates, such as the surface-bound monolayers of redox species. Porous electrodes or phase-

transforming particles with non-uniform reaction rates cannot be described by this equation.[85] A model with a simple three-state Markov chain which consists of untransformed, active (transforming), and transformed particles can be used to describe the redox dynamics in a porous electrode.[85,86] As shown in **Figure 2.7**, we assume that the $LiFePO_4$ porous electrode consists of $FePO_4$ particles, active (phase-transforming) particles, and $LiFePO_4$ particles. k_A is the activation rate of each $FePO_4$ particle to transform into an activate particle. k is the reaction rate at the surface of activate particles that continuously intercalate/deintercalate lithium ions during charging/discharging process.[85,86]

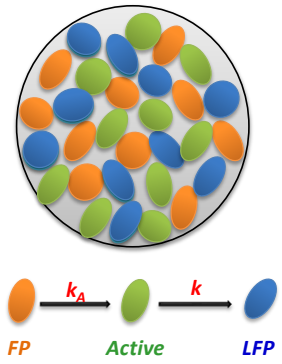

Figure 2.7 Schematic process in a porous electrode consisting of $FePO_4$ (FP) particles which will transform to active particles with an activation rate of k_A, active (transforming) particles, and $LiFePO_4$ (LFP) particle which are transformed from an active particle with a reaction rate of k.[86]

A statistical model for characterizing discrete-particle phase transformations in porous electrode has been reported by Bai and Tian recently.[85,86] The following equation expresses the transient current generated from a potential step in porous electrode:[85]

$$I = kQ\left[\frac{N_0 k+(N_1-1)k_A}{k-k_A}e^{-kt} + \frac{(1-N_0-N_1)k_A}{k-k_A}e^{-k_A t}\right] \quad (2.8)$$

where Q is the capacity, N_0 is the initial fraction of reacting particles in the electrode. N_1 is the initial fraction of inactive particles in the electrode, which is set to zero in this work.[85] According to the above method, Bai et al. extracted the charge transfer rates in carbon-coated $LiFePO_4$ porous

electrodes from potential step experiments over a range of temperatures. The rate constant k_0 of ~ 2×10^{-4} s^{-1} and a reorganization energy λ of ~ 460 meV can be obtained.[85]

J. Friedl et al. reported a kinetic study of POMs as electrolyte. A chronoamperometric single pulse method at different temperatures is utilized to investigate the charge transfer kinetics of a tri-manganese substituted Keggin-based tungstosilicates $[MnIII_3(OH)_3(H_2O)_3(A\text{-}\alpha\text{-}SiW_9O_{34})]^{4-}$ **($Mn^{III}_3SiW_9$)** dissolved in solution.[87] The oxidation of solvated Mn^{III}_3 to Mn^{IV}_3 exhibits a kinetic rate of k_0 =0.0032 cm s^{-1}. So far, there are kinetic studies for POMs in solution as electrolytes,[87] but no systematic investigation of the electron transfer rates of POMs as solid-state porous electrode materials.

2.2.5 The research scopes of POM LIBs in this thesis

In LIBs systems, V-based POM materials (polyoxovanadates) also show high capacity and long cycling stability.[3,22,24] Thus we will focus on V-based POM, $Na_6[V_{10}O_{28}]$, as electrode materials for LIBs.

To further understand the charge storage/transport which takes place at the electrode-electrolyte interface, the study of oxidation state changes in POM materials and transport mechanisms are important. Here we propose two assumptions of POM electrodes and later prove these assumptions by fundamental electrochemistry studies. First, POMs can transfer multiple electrons per molecule which can lead to a high energy density. Second, due to their large size, POMs exhibit a low reorganization energy upon electron transfer which leads to high rate capability and therefore high power density. The reorganization energy of POMs is expected to be low because the POM framework shields the electrostatic interaction between redox-center and polar solvent.[87]

In this study, advanced techniques such as in-situ X-ray absorption spectroscopy will be used to determine how many charges can be stored in the $Na_6[V_{10}O_{28}]$ electrode. For high power density studies, the fundamental kinetic studies will be investigated with potential step methods.

2.3 Na-ion batteries (NIBs)

The high abundance of sodium (~ 2.5 % in the earth's crust) and potential cost advantages over LIBs enable Na-ion batteries (NIBs) be a promising candidate for large-scale energy storage.[6] Therefore, NIBs have attracted significant attention recently. Na is an alkali metal and has chemical properties similar to Li. Thus, it is commonly assumed that transfer of materials and techniques from LIB to NIB technology are simple. However, the higher standard reduction potential ($E^0_{Na^+/Na}$ = −2.17 V vs. standard hydrogen electrode (SHE); $E^0_{Li^+/Li}$ = −3.04 V vs. SHE)[4] and the heavier atomic mass of Na result in a lower energy density for NIBs. Nonetheless, the cost advantage over LIBs still make NIBs a promising candidate for large-scale applications.[4] In order to intercalate the larger atomic mass and ionic radius of Na^+ as compared to Li^+, the electrode materials are restricted to those that provide large channels and interstitial sites for reversible Na-ion-intercalation. However, the relatively large Na^+ widens the flexibility of material design. Many Na-containing materials can be prepared easily under thermodynamic equilibrium conditions and can be found in natural minerals.[6] Furthermore, the larger ionic radius of Na^+ compared with Li^+ bring on a lower desolvation energy in polar solvents which results in faster diffusion processes and increases the possibility of high-power battery design with NIBs.[6]

2.3.1 Basic Principles of NIBs

Commercialized high-temperature sodium-based batteries (such as Na/S_7 and $Na/NiCl_{28}$ systems) utilize metallic sodium as an anode and alumina-based solid (ceramic) as electrolyte. They require high operating temperature (~300 °C) to maintain the electrodes in the liquid state in order to have good contact with the solid−electrolyte. The active materials contain molten sodium and sulfur at such high temperature, safety issues of high-temperature sodium-based batteries are critical concerns. Unlike those high-temperature sodium-based batteries, NIBs can be operated at ambient temperature. NIBs consist of sodium insertion electrode materials without metallic sodium (except during unfavorable reactions such as overcharge) and Na-containing organic electrolyte. Structures, components, systems, and charge storage mechanisms of NIBs are basically as same as LIBs where the Li ions are replaced with Na ions. A NIB consists of sodium insertion anode and cathode with a Na-ion-containing organic electrolyte as shown in **Figure 2.8**.

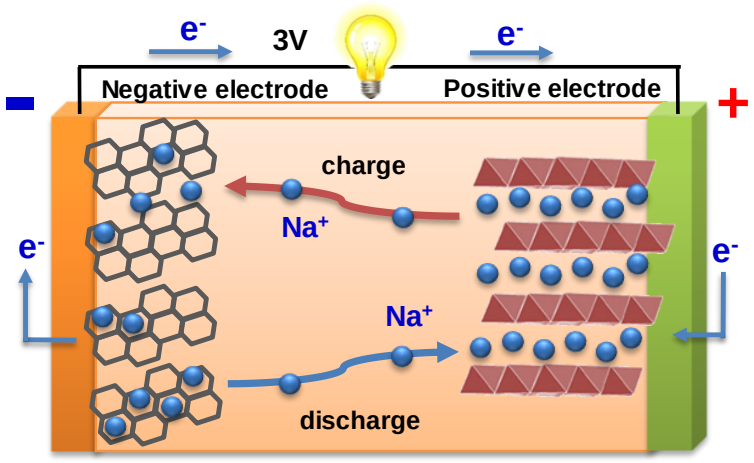

Figure 2.8 Schematic illustration of Na-ion batteries[6]

2.3.2 Anode Materials for NIBs

The most widely used anode material for LIBs is graphite. However, Na ions are not easy to intercalate into graphite reversibly due to unfavorable thermodynamical processes.[25,88] Different kind of anode materials have been developed for NIBs, including carbonaceous materials,[4,5,26,27,89]

metal oxides/sulfides,[28,29,90-101] sodium alloys, [24-33] phosphorus,[32] phosphides,[102] organic compounds,[37,38] and POMs.[25] A selection of those anode materials is presented in **Figure 2.9**.[25]

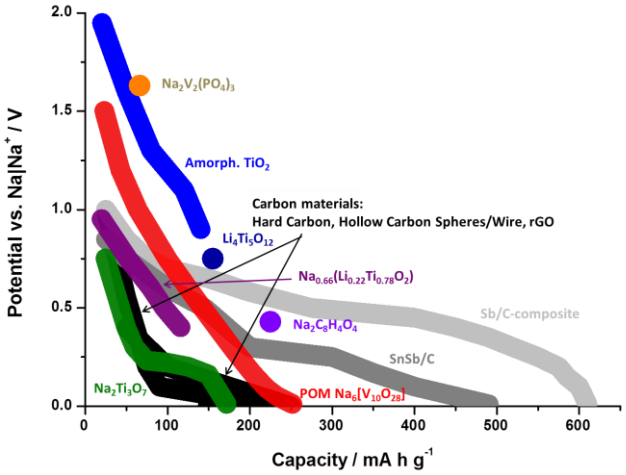

Figure 2.9 Overview of different anode materials for sodium ion batteries. Reproduced by permission of the reference.[25]

Recent works on titanium-based oxides include TiO_2,[28] $Li_4Ti_5O_{12}$,[90] $Na_2Ti_3O_7$,[91] and layered P2-$Na_{0.66}[Li_{0.22}Ti_{0.78}]O_2$.[29] TiO_2 has attracted researcher's attention due to their low cost and high availability of materials.[88] The reversible capacity of mesoporous TiO_2 is around 150 mA h g^{-1} when cycled between 0.01 and 2.5 V vs. Na^+/Na.[28] Spinel $Li_4Ti_5O_{12}$ provided a reversible capacity of ~150 mA h g^{-1} at an average potential of 0.9 V with a first cycle coulombic efficiency up to ~81 %.[90]A discharge capacity of approximately 200 mA h g^{-1} could be obtained for layered $Na_2Ti_3O_7$ with a voltage plateau at 0.3 V vs. Na^+/Na when cycled between 0.01 and 2.5 V; however, cycling stability is poor.[91]

Other conversion type metal oxides/sulfides exhibit high capacities such as $NiCoO_4$ (initial discharge/charge capacity of ~ 618 / 200 mA h g^{-1}),[92] Fe_3O_4 (initial discharge/charge capacity of ~ 643 / 366 mA h g^{-1}),[93] MoO_3 (initial discharge/charge capacity of ~ 771 / 410 mA h g^{-1}),[94] CuO (initial discharge/charge capacity of ~ 935 / 640 mA h g^{-1}),[95] Ni_3S_2,[96] MoS_2,[97] SnS_2,[98] SnS,[98]

Co_9S_8,[99] FeS,[100] and Sb_2S_3.[101] Nevertheless, they are suffered from large potential hysteresis (for some larger than 1 V), low initial coulombic efficiency (30–70%) and poor cycling stability which restrict the actual application of those conversion materials in NIBs.[88] Large volume change during sodiation/desodiation might be the main reason for the poor cycling stability. It can be improved by using carbon composite materials (eg. graphene) and by modification of the electrolytes (with the addition of FEC).[88] Several metals electrode materials such as tin (Sn) and antimony (Sb) can deliver high capacities by forming sodium alloys.[30,31,88,103-110] Large initial discharge capacities of 878 mA h g^{-1} for Sn and ~ 600 mA h g^{-1} for Sb can be approached. However, large volume expansion (420 % volume change for Sn and 290 % for Sb) during the formation of alloys leads to fast capacity fading.[30,31,88] Nanosizing and the preparation of composites materials (carbon composite or intermetallics composites) are possible solutions to improve the cycling stability of Sn and Sb.[103-110] Carbon and the intermetallics components in the composites are used as a buffering matrix for the volume expansion during the Na ion (de-)insertion reactions.[88] An initial capacity of 544 mA h g^{-1} with a capacity retention of 80 % after 50 cycles can be achieved by SnSb/C composites reported by Xiao *et al*.[111] Organic compounds with high structural flexibility and low cost, as well as an open structure for high structure kinetics, have also been investigated as potential anode materials in NIBs.[88] Recently Zhao *et. al.* and Park *et. al.* have reported 250 and 300 mA h g^{-1}, respectively, for disodium terephthalate ($Na_2C_8H_4O_4$) with an intercalation potential of 0.29 V vs. Na^+/Na.[112,113] During the charge/discharge process, the disodium terephthalate reacts to tetrasodium terephthalate through a radical intermediate that stabilizes conjugated structure between the carbonyl and phenyl groups.[25,88] However, a high percentage of conductive agent (up to 37.5%) was used because of the non-conductive nature of the organic compounds that limits the applications in practical devices.[113] Hartung et al. have reported a promising new class of materials, polyoxometalates (POMs), as an anode in NIBs. $Na_6[V_{10}O_{28}]\bullet 16H_2O$ reveals a reversible capacity

of approximately 276 mA h g^{-1} with an average discharge potential of 0.4 V vs. Na^+/Na, as well as a high cycling stability.[25]

Among above materials, carbon-based materials are the most promising candidates due to their low-cost, easily attainable, and environmentally friendly advantages. Furthermore, they can be utilized as buffer matrixes for conversion and alloy type anode in order to prevent the volume expansion during the Na ion (de-)intercalation.[103-110] Potential carbon materials such as hard carbon,[26] expanded graphite,[89] reduced graphene oxide (rGO),[4] and nitrogen-doped carbon fibers have been developed.[27] Palacin et al reported a hard carbon as NIB anode material which shows high cycling stability at C/10 for over 100 cycles with the capacity more than 300 mAh g^{-1}.[26] However, the capacity at 20 C is only around 150 mAh g^{-1} due to its lower electronic conductivity as compared to other carbon materials such as graphite and rGO. Furthermore, high synthesis temperature of up to 1100 °C is required for hard carbon in order to increase the electrical conductivity which causes high energy consumption during the synthesis. Expanded graphite which exhibits excellent cycling stability with a very low capacity decay rate of ~ 0.013% per cycle from the 11^{th} cycle to $2{,}000^{th}$ cycle has been reported by Wen et al.[89] However, expanded graphite displays a poor rate capability where the capacity drops from 284 mAh g^{-1} at 20 mA g^{-1} to 91 mAh g^{-1} at 200 mA g^{-1}. RGO has attracted much attention recently because of its superior properties such as high electronic conductivity, good chemical stability, and high surface area.[33,114] A rGO anode which has been reported by Wang et al. exhibits reversible capacities of 217.2 mAh g^{-1} at 40 mA g^{-1} and 95.6 mAh g^{-1} at a high current rate of 1000 mA g^{-1}, exhibiting good rate capability.[4] Nevertheless, the highly irreversible capacity in the 1^{st} cycle, and the restacking problem of the rGO sheets during cycling leads to poor capacity retention.[33] RGO have been used to prepare composite materials with many alloy type or metal

sulphide anode materials in order to increase electrical connectivity and surface area, as well as prevent volume expansion.[33,88,115] A rGO/Sb_2S_3 composite which has been reported by Yu et al. exhibits a high capacity of 730 mAh g^{-1} at 50 mA g^{-1}, and an excellent rate capability of up to 6C with a good cycle stability.[115] Wang et al. reported functionalized N-doped carbon nanofibers (FN-CNFs) as anode material for NIB showing a capacity of 134.2 mA h g^{-1} after 200 cycles at a current density of 200 mA g^{-1} (capacity retention of 88.7%).[27] The porous carbon nanofibers with interconnected structure provide a continuous path for electron transport and enable Na ions transport easily. The functional groups which contain oxygen and nitrogen on the surface of FN-CNFs can speed up the surface redox reactions and induce a large number of defects on the graphene layer which enhances sodium ion absorption properties leading to high rate performance.[27]

2.3.3 The research scopes of nanostructured carbon NIBs in this thesis

A nanostructured carbon material, core–shell heterostructure with multi-walled carbon nanotubes (MWCNTs) as the core and graphene oxide nanoribbons (GONRs) as the shell (MWCNT@GONR), is proposed as anode material for NIBs in this thesis. The MWCNT@GONR samples will be synthesized by a simple microwave assistant method which cuts the surface of MWCNTs. MWCNT@GONR provides unique core-shell structure consisting of MWCNTs between flat GONR sheets to avoid the restacking problem of graphene and ease the penetration of the electrolyte. The synthesis process of unzipping the MWCNTs generates many functional groups on the surface. In order to investigate the influence of functional groups on ion adsorption, different thermal treatment temperatures will be used to vary the amount of functional groups attached. These functionalized MWCNT@GONR samples will then be characterized by FT-IR, TGA, BET surface area measurement, XRD, XPS, Raman, FESEM, and HRTEM. The battery

performance will be analyzed by cyclic voltammetry and galvanostatic charge/discharge. The charge storage and transport mechanism will also be investigated. A comparison with commercial graphene nanopowder (GNP) and MWCNTs employed as anode materials is conducted.

Chapter 3 Experimental Methodology

3.1 Synthesis of POMs, POM/Carbon hybrid, and MWCNT@GONR

3.1.1 Synthesis of $Na_6[V_{10}O_{28}]$

Decavanadate(V), $Na_6[V_{10}O_{28}]$, was prepared according to the method from literature.[116] A 3 g sample of sodium metavanadate ($NaVO_3$) was dissolved in 100 mL water and 4 M HCl was used to decrease the pH to 4.8. The solution was filtered and additional HCl reduced the pH again to 4.5. After adding 200 mL 95% ethanol, the bulk sodium salt of the polyanion was precipitated from the solution. The orange $Na_6[V_{10}O_{28}]$ product was then isolated by filtration and air-dried.

3.1.2 Synthesis of SWCNT-TBA-PV_2Mo_{10} nanohybrid

$[(CH_3(CH_2)_3)_4N]_5[PV_2Mo_{10}O_{40}]$ (**TBA-PV_2Mo_{10}**, TBA: $[(CH_3(CH_2)_3)_4N]^+$, tetra-n-butyl ammonium) was synthesized according to a method described in literature.[117,118] 24.4 g sodium metavanadate ($NaVO_3$) was dissolved in 100 mL boiling H_2O. 7.1 g Na_2HPO_4 in 100 mL H_2O was then added to the above solution. After the solution cooled to room temperature, 5 mL concentrated H_2SO_4 was added, then 121 g Na_2MoO_4•$2H_2O$ in 200 mL H_2O were added and stirred vigorously. Next, 85 mL concentrated H_2SO_4 were added in the solution slowly. The orange $(TBA)_5[PV_2Mo_{10}O_{40}]$ which was obtained by adding 19.5 g of TBA-Br into the homogeneous solution, was thoroughly filtered and washed with water in order to get the desired powder.

Purified SWCNTs with 1−3 atomic% carboxylic acid groups were purchased from Carbon Solution, Inc. The **SWCNT-TBA-PV_2Mo_{10}** nanohybrid material was prepared according to the method reported by Kawasaki et al.[51] 17 mg of **TBA-PV_2Mo_{10}** dissolved in acetonitrile solution (5 mL) was added to a toluene suspension (50 mL) with 40 mg purified SWCNTs. The yellowish mixture was stirred vigorously at room temperature for 10 minutes. The solution became colorless

and a black precipitate was formed after leaving the mixture to stand for 1 hour. This indicates that all the **TBA-PV_2Mo_{10}** molecules were anchored onto the surface of SWCNTs. The solution was filtered using a membrane with pore diameter of 0.1 mm, and then the product was washed with toluene for several times, followed by drying at 80 °C under vacuum overnight.

3.1.3 Synthesis of MWCNT@GONR

MWCNTs were purchased from Mitsui & Co. (diameter = 40~90 nm; length = >10 μm). Sulfuric acid (H_2SO_4, 98 %), phosphoric acid (H_3PO_4, 85 %), and potassium permanganate ($KMnO_4$) were obtained from J. T. Baker.

The MWCNT@GONR was prepared using the method described in literature.[119,120] 0.05 g MWCNTs were suspended in a H_2SO_4/H_3PO_4 solution (molar ratio 9:1), followed by a microwave treatment (microwave reactor, CEM-Discover) at 200 W for 2 min. After adding 0.25 g $KMnO_4$, the solution was then treated with the same micro-wave power at 65 °C for 4 min. A weak acid, H_3PO_4, was utilized to ameliorate the selectivity of the oxidative unzipping process, assuming the in-situ protection of the vicinal diols formed on the basal plane of graphene during oxidation and therefore prevents their over oxidation and the subsequent hole generation.

The MWCNT@GONR solution was filtered by a Millipore membrane with a pore size of 0.1 mm, followed by washing with deionized (DI) water several times and then dried at 80 °C overnight. This as-prepared MWCNT@GONR contained oxygen-containing functional groups (carboxylic acid groups). In order to investigate the effect of functional groups, a further thermal treatment in a tube furnace at temperature range from 300 °C to 900 °C with an argon flow of 5 cm^3 min^{-1} was applied to reduce MWCNT@GONR.

3.2 SCs and Batteries Preparation

3.2.1 $Na_6[V_{10}O_{28}]$ as electrode material for SCs

- ***Electrode preparation***

The active material ($Na_6[V_{10}O_{28}]$) was mixed with poly(vinylidene fluoride) (PVDF) binder and carbon black (super P) in N-methylpyrrolidinone (NMP) with a weight ratio of 75:15:10 to prepare the active layer of the electrodes. The slurry was coated onto graphite papers with the working area of 1 cm × 1 cm as working electrodes and dried at 80 °C overnight, as shown in **Figure 3.1**.

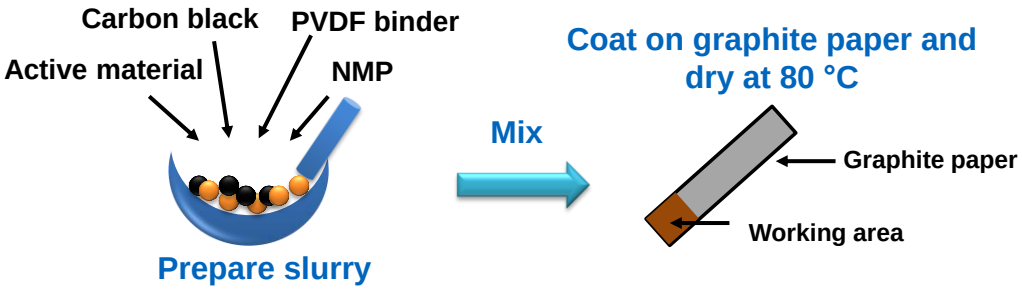

Figure 3.1 Process flow of electrode preparation

- ***Three-electrode set-up***

A three-electrode cell set-up which utilizes $Na_6[V_{10}O_{28}]$ on graphite paper as the working electrode, $Ag/AgNO_3$ as the reference electrode, a platinum wire as the counter electrode, and an organic electrolyte (1 M $LiClO_4$ in propylene carbonate (PC)) as electrolyte was used to test cyclic voltammetry (CV) and galvanostatic charge/discharge (GCD) cycles, as shown in **Figure 3.2**.

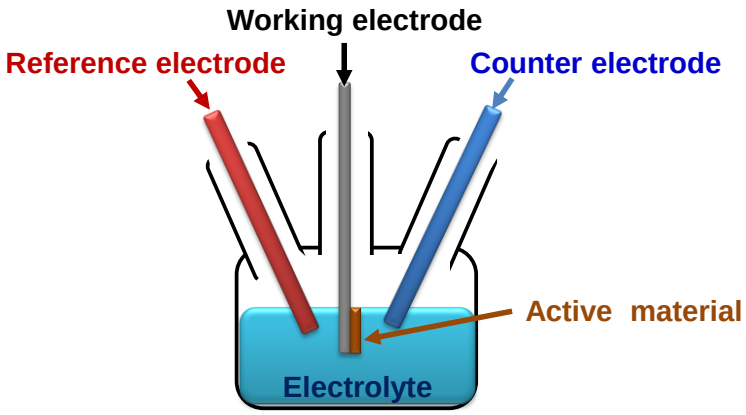

Figure 0.2 A three-electrode cell set-up which consisted of a working electrode, a reference electrode, and a counter electrode in an electrolyte.

- ***Asymmetric AC// $Na_6V_{10}O_{28}$ SCs***

The method of preparation of the activated carbon (AC) (Norit, The Netherlands) electrode was as same as for $Na_6[V_{10}O_{28}]$ electrode. The asymmetric SC was fabricated as pouch cell as shown in Figure 3.3 using $Na_6[V_{10}O_{28}]$ as negative electrode and AC as positive electrode after match the mass of the active materials. A porous glassy fibrous paper (GF/D) from Whatman was used as a separator, and 1 M $LiClO_4$ in PC as electrolyte. The devices was sealed by heat pressing the SCs in-between two pieces of polymer-coated Aluminum foil (Charlston Technologies, D-EL40H).

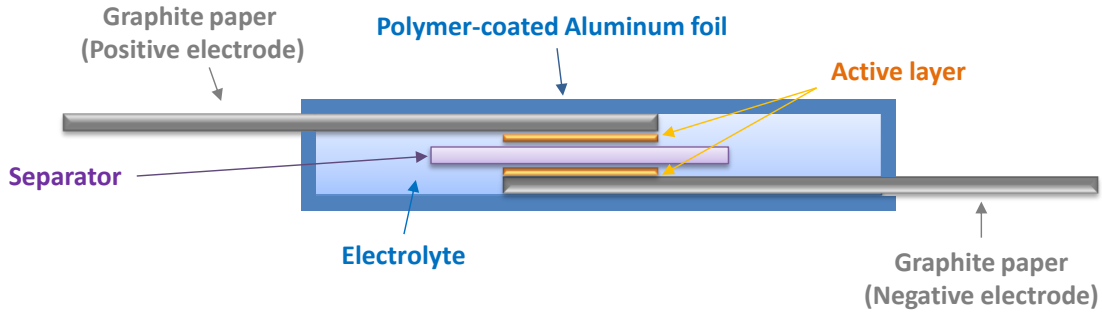

Figure 3.3 An asymmetric SC with a pouch cell configuration which consists of a positive electrode, a negative electrode, and a separator in an electrolyte. The pouch cell was sealed by heat pressing the SCs in-between two pieces of polymer-coated Aluminum foil

3.2.2 $Na_6V_{10}O_{28}$ as cathode material for LIBs

- ***Electrode preparation***

The active layers of electrodes were prepared by mixing active material ($Na_6[V_{10}O_{28}]$), poly(vinylidene fluoride) (PVDF) binder, and carbon black (super P) in N-methylpyrrolidinone (NMP) with a weight ratio of 60 : 20 : 20, respectively. The slurry was coated onto Al foil using a doctor blade, and then the electrode was dried in air at 80 °C at least 3 hours in order to remove the NMP solvent. After drying, the coating was punched into pieces with diameter 16 mm and then roll-pressed, followed by drying at 110 °C under vacuum for 4 hours.

- ***LIB half-cell configuration***

The $Na_6[V_{10}O_{28}]$ electrodes were assembled in 2016 coin cells as the working electrode with circular metallic lithium metal (diameter 16 mm) as the counter electrode, and a glass fiber paper (Whatman, diameter 19 mm) as separator. 1M $LiPF_6$ in a mixture of ethylene carbonate (EC) and diethyl carbonate (DEC) (1:1 weight %) was used as electrolyte.

3.2.3 SWCNT-TBA-PV_2Mo_{10} as electrode material for SCs

- ***Electrode preparation***

The active layers of electrodes were prepared by mixing active material (**SWCNT-TBA-PV_2Mo_{10}**, SWCNT, or **TBA-PV_2Mo_{10}**), poly(vinylidene fluoride) (PVDF) binder, and carbon black (super P) in N-methylpyrrolidinone (NMP) with a weight ratio of 75 : 15 : 10, respectively, as shown in **Figure 3.1.** The slurry was coated onto graphite papers (1 cm × 1 cm) as well as the facets of glassy carbon rods, and then dried at 80 °C overnight.

- ***Three-electrode set-up***

A three-electrode cell as shown in **Figure 3.2** was used to test the CV of **SWCNT-TBA-PV_2Mo_{10}** nanohybrid material and SWCNT in an acidic aqueous electrolyte (1 M H_2SO_4). The

materials which were coated onto the facets of glassy carbon rods were utilized as working electrodes. Ag/AgCl in 3.5 M KCl was used as the reference electrode, and a platinum wire was used as the counter electrode.

- ***Symmetric SCs***

The symmetric SCs were fabricated as pouch cells as shown in **Figure 3.3** using the coated graphite papers as working electrodes, porous glassy fibrous papers (GF/D) purchased from Whatman as separators, and 1 M H_2SO_4 as electrolyte. The pouch cells were sealed by heat pressing the SCs in-between two pieces of polymer-coated Aluminum foil (Charlston Technologies, D-EL40H).

3.2.4 MWCNT@GONR as anode material for NIBs

- ***Electrode preparation***

Commercial MWCNT and GNP were used as comparison in this study. Commercial GNP (UR-graphene 12, 99.2%, special surface area ~ 80 m^2 g^{-1}, average flake thickness ~ 12 nm, with 30 to 50 monolayers, average particle (lateral) size ~ 4.5 mm) was purchased from Uni-Region. The active layer of the electrodes were prepared by mixing active material (commercial MWCNT, GNP, or synthesized MWCNT@GONR) with carbon black as conducting agent (super P, Sigma-Aldrich) and sodium carboxymethyl cellulose (CMC) (Sigma-Aldrich) as binder in a solution of DI water : methanol (1 : 1 weight %) with a weight ratio of 80 : 10 : 10. The slurry was stirred overnight and coated onto a copper foil by a doctor blade and then dried in air at 80 °C at least 3 hours to remove the solvent. The dried coating was punched into pieces with a diameter of 10 mm followed by roll-pressing. The coating was then dried in an oven at 110 °C under vacuum overnight.

- ***NIB half-cell configuration***

2016 coin cells were assembled with those coated foils as working electrodes, circular metallic sodium metal (diameter 16 mm) as the counter electrode, and glass fiber (Whatman) with a diameter of 19 mm as a separator. The electrolyte was prepared by 1M $NaClO_4$ in a mixture of ethylene carbonate (EC) and propylene carbonate (PC) (1:1 weight %).

- ***NIB full-cell configuration***

A full cell prepared with P2-Na_xMnO_2 cathode and MWCNT@GONR anode was used to investigate the potential of MWCNT@GONR in a practical NIB application. The P2-Na_xMnO_2 cathode material was synthesized according to the literature.[121] NH_4HCO_3 was dissolved in deionized water and followed by the addition of a small amount of ethanol. A solution of $MnSO_4$ in deionized water was added to the above solution drop by drop. Spherical $MnCO_3$ was formed after stirring this solution at room temperature. The precipitate was filtered and washed with water and ethanol for several times, following by annealing in air for 5 h at 400 °C leading to the formation of spherical MnO_2 powder. The spherical MnO_2 powder was dispersed in a solution of NaOH in deionized water and ethanol. After the solvents were evaporated, the powder was annealed in air for 3 h at 320 °C and then 4 h at 800 °C in order to produce spherical P2-Na_xMnO_2. The spherical P2-Na_xMnO_2 was mixed with acetylene black as conducting agent (Alfa Aesar) and polyvinylidene fluoride (PVDF, Arkema, Kynar HSV 900) binder in the weight ratio 60:20:20 with N-methyl-2-pyrrolidone (NMP) to form a homogeneous slurry for the cathode preparation. This mixed slurry was then coated on an aluminum foil using a doctor blade and the coating was dried in air at 80 °C to remove the NMP. The coating was punched into pieces (diameter of 16 mm) and then roll-pressed, followed by drying in an oven at 110 °C under vacuum overnight. MWCNT@GONR anode and P2-Na_xMnO_2 cathode were tested in half-cells separately with a current density of 20 mA g^{-1} in order to calculate the mass ratio for full cell preparation. The

MWCNT@GONR half-cell was cycled for five times and kept at 2.2 V vs. Na/Na^+, while the P2-$Na_{0.7}MnO_2$ half-cell was cycled for two time and kept at 2.2 V vs. Na/Na^+ in order to reduce the effect of solid electrolyte interfaces formation. Those electrodes were assembled as a full cell with a matched mass ratio, and the full cell was charged/discharged between voltage of 0 ~ 4 V at a current density of 20 mA g^{-1} based on the mass of anode active material.

3.3 Characterization Techniques

3.3.1 Materials Characterizations

- **Fourier Transform Infrared Spectroscopy (FT-IR)**

A Fourier transform infrared spectroscopy (FTIR) spectrophotometer (PerkimElmer Frontier) was used to record the infrared spectra of $Na_6[V_{10}O_{28}]$, **TBA-PV_2Mo_{10}**, SWCNT, **SWCNT-TBA-PV_2Mo_{10}**, MWCNT, GNP, and MWCNT@GONR using KBr pellets and repeatedly scanned four times over the range of 4000 – 400 cm^{-1}.

- **Nuclear Magnetic Resonance Spectroscopy (NMR)**

The identity of $Na_6[V_{10}O_{28}]$ was also established by ^{51}V NMR, and the identity of **TBA-PV_2Mo_{10}** was established by ^{31}P NMR, ^{51}V NMR. The NMR spectra were recorded on a 400 MHz JEOL ECX instrument.

- **Inductively Coupled Plasma Spectroscopy (ICP)**

Inductively coupled plasma spectroscopy (ICP) was utilized to detect the atomic ratio of sodium and vanadium of $Na_6[V_{10}O_{28}]$ with a Dual-view Optima 5300 DV ICP-OES system.

- **UV-Vis spectrophotometer**

The identity of **TBA-PV_2Mo_{10}** was established by UV-Vis spectrum, which was carried out on a UV-Vis spectrophotometer (Varian Cary 100 Bio).

- **Thermo Gravimetric Analysis (TGA) and Mass Spectroscopy (MS)**

TA Instruments SDT Q600 thermobalance was used to determine the thermogravimetric analysis (TGA) of $Na_6[V_{10}O_{28}]$, SWCNT, **TBA-PV_2Mo_{10}**, and **SWCNT-TBA-PV_2Mo_{10}**. The TGA measurements were recorded under 100 mL min^{-1} flow of nitrogen and the temperature was increased from 20 to 800 °C at a rate of 5 °C min^{-1}. A TGA coupled with mass spectroscopy (TGA-MS) setup (STARe TGA from Mettler Toledo connected with Thermostar GSD3200 from Pfeiffer Vacuum) was utilized to measure the decomposition temperature of the surface functional groups of MWCNT@GONR. The samples were heated from 25 °C to 100 °C with a constant temperature ramp of 10 °C /min under an argon flow of 100 mL min^{-1} and dwelled at 100 °C for 2 h in order to get rid of the water adsorption. Then the temperature was increased again from 100 °C to 1000 °C at the same condition.

- **Brunauer-Emmet- Teller (BET) surface area measurement**

The Brunauer Emmetand Teller (BET, Quantachrome NOVA 3200 BET) surface area and the Barrett-Joyner-Halenda (BJH) pore size distribution of $Na_6[V_{10}O_{28}]$, SWCNT, **TBA-PV_2Mo_{10}**, **SWCNT-TBA-PV_2Mo_{10},** MWCNT, and MWCNT@GONR were detected by N_2 adsorption-desorption isotherms at 77 K.

- **Field-emission Scanning Electron Microscopy (FESEM)**

The surface morphologies of $Na_6[V_{10}O_{28}]$, SWCNT, **TBA-PV_2Mo_{10}**, **SWCNT-TBA-PV_2Mo_{10},** MWCNT, GNP, and MWCNT@GONR were characterized by field emission scanning electron microscope (FESEM, JEOL JSM 7600F). Samples were prepared by pasting the powder onto the copper holder using carbon tape. Scanning of the images was done at an accelerating voltage of 15 kV.

- **Transmission Electron Microscopy (TEM)**

The morphologies of $Na_6[V_{10}O_{28}]$, SWCNT, **TBA-PV_2Mo_{10}**, **SWCNT-TBA-PV_2Mo_{10},** MWCNT, GNP, and MWCNT@GONR were detected by high resolution transmission electron

microscopy (HRTEM, JOEL-JSM 2100F) equipped with high contrast objective aperture (20μm in diameter) equivalent to a point to point resolution of 1.7Å. The HRTEM images were performed at 200 kV.

- **X-ray diffraction (XRD)**

The Rigaku Smartlab X-ray Diffractometer was utilized to determine the d-spacing of MWCNT, GNP, and MWCNT@GONR by X-ray diffraction (XRD) measurements.

- **Raman spectroscopy**

Renishaw Raman Microscopy with 2.33 eV (532 nm) excitation laser was used to record the Raman spectroscopy of MWCNT and MWCNT@GONR.

- **X-ray photoelectron spectrometer (XPS)**

An X-ray photoelectron spectrometer (XPS, PHI Kratos AXIS Ultra) with a monochromatic Al Kα (1486.71 eV) X-ray radiation (15 kV / 10 mA) was used to analyze the Li-ion intercalation and vanadium oxidation states of $Na_6[V_{10}O_{28}]$ SC electrodes tested in 1 M $LiClO_4$ in PC. C 1s line of the adventitious carbon at 284.6 eV was utilized as reference.

A X-ray photoelectron spectrometer (Thermo Fisher Scientific ThetaProbe XPS) with a monochromatic Al Kα (1486.68 eV) X-ray radiation (15 kV / 6.7 mA) was used to detect the surface functional groups on MWCNT, GNP, and MWCNT@GONR. C 1s line of the adventitious carbon at 285.0 eV was utilized as reference.

3.3.2 Electrochemical Characterizations

3.3.2.1 Cyclic voltammetry (CV)

Cyclic voltammetry (CV) cycles of $Na_6V_{10}O_{28}$ SC working electrodes were investigated using a three-electrode cell set-up tested in a Biologic VMP3 potentiostat in the potential range of 1.6 – 1.2 V vs. $Ag/AgNO_3$ at various scan rates (20, 10, 5, and 2 mVs^{-1}). The $AC//Na_6V_{10}O_{28}$ asymmetric

SC device was characterized by CV measurement with a potentiostat (Solatron, SI 1255B) in the potential range of 0–2.8 V at different scan rates (20, 10, 5, and 1 mVs^{-1}). A Bio-Logic SP300 potentiostat was used to measure CV of $Na_6V_{10}O_{28}$ LIB half-cell in the potential range of 1.75 V to 4.0 V vs. Li/Li^+ at scan rates of 0.1, 0.2, 0.5, 1, and 2 mVs^{-1}, and MWCNT@GONR NIB half-cell in the potential range of 0.005 V to 3.0 V vs. Na/Na^+ at scan rates of 0.1, 0.2, 0.3, 0.5, 0.8, 1, 2, 3 and 5 mVs^{-1}. CV of **SWCNT-TBA-PV_2Mo_{10}** nanohybrid material and SWCNT coated on glassy carbon electrodes was performed using a three-electrode cell, while the potential and current control and data acquisition was done with a Biologic VMP3 potentiostat in the potential range of −0.2 V to 1.0 V vs. Ag/AgCl at scan rates of 100, 50, 20, 10, and 5 mVs^{-1}.

3.3.2.2 Galvanostatic charge-discharge (GCD)

Galvanostatic charge/discharge (GCD) cycles of $Na_6V_{10}O_{28}$ SC working electrodes were investigated using a three-electrode cell set-up tested in a Biologic VMP3 potentiostat in the potential range of 1.6 V – 1.2 V vs. $Ag/AgNO_3$. The AC//$Na_6V_{10}O_{28}$ asymmetric SC device was characterized by GCD measurement with a potentiostat (Solatron, SI 1255B) in the potential range of 0 V – 2.8 V. The **SWCNT-TBA-PV_2Mo_{10}** symmetric devices were characterized by GCD cycle measurements with a potentiostat (Solatron, SI 1255B) in the potential range of 0 V – 1 V. A Neware battery tester was employed for GCD tests of $Na_6V_{10}O_{28}$ LIB half-cells in the range of 1.75 V – 4 V vs. Li/Li^+, and of MWCNT@GONR NIB half-cells in the range of 0.005 V – 3 V vs. Na/Na^+. The MWCNT@GONR//P2-$Na_{0.7}MnO_2$ NIB full cell was charged and discharged between a voltage of 0 V – 4 V at a current density of 20 mA g^{-1} based on the mass of anode active material.

3.3.2.3 Chronoamperometry

The LIB half-cell configuration was employed to investigate the kinetic of $Na_6[V_{10}O_{28}]$ electrodes. Chronoamperometry experiments of $Na_6[V_{10}O_{28}]$ electrodes were conducted at −10, 10, 25, 50 ˚C with a Bio-Logic SP300 potentiostat. $Na_6[V_{10}O_{28}]$ electrodes were maintained at a potential of 4.0 V vs. Li/Li^+ for 4 h before each negative over potential step in order to ensure that the whole electrode is fully oxidized. Similarly, the electrode was kept at 2.0 V vs. Li/Li^+ for 4 h for positive over-potentials. The size of the potential step was estimated based on the equilibrium potential $E^{0'}$ which was measured as the average of the mean peak potentials from the CV at different temperatures.

3.3.2.4 In-situ X-ray Absorption Spectroscopy (XAS)

As shown in **Figure 3.4,** the in-situ XAS cell was a modified 2016 coin cell where the $Na_6[V_{10}O_{28}]$ is the working electrode (diameter 16 mm), circular metallic lithium metal (diameter 16 mm) is the counter electrode, and polyolefin (diameter 19 mm) is separator. The stainless steel cap, bottom, spacer, and spring were punched with a hole in the middle in order to generate windows for X-ray penetration (beam size: 2×2 mm^2). Those holes were covered with Kapton tape sealed using epoxy adhesive (AB glue). 1M $LiPF_6$ in EC:DEC (1:1 weight %) was used as electrolyte.

The beamline BL17C at the National Synchrotron Radiation Research Center (NSRRC), Hsinchu, Taiwan was employed to measure the in-situ V K-edge XAS spectra in transmission mode at room temperature, as shown in **Figure 3.5**. The electronic accelerator of the storage ring supplied 1.5 GeV with an operating current of 360 mA. A Si double crystal monochromator was used to perform energy scan so as to adjust the parallelism and prevent higher order harmonics. The beam size on the electrode was restricted to an area of 2×2 mm^2 during in-situ XAS

measurements. Ionization chambers were utilized to detect the intensity of the incident and transmitted beams through the coin cell.

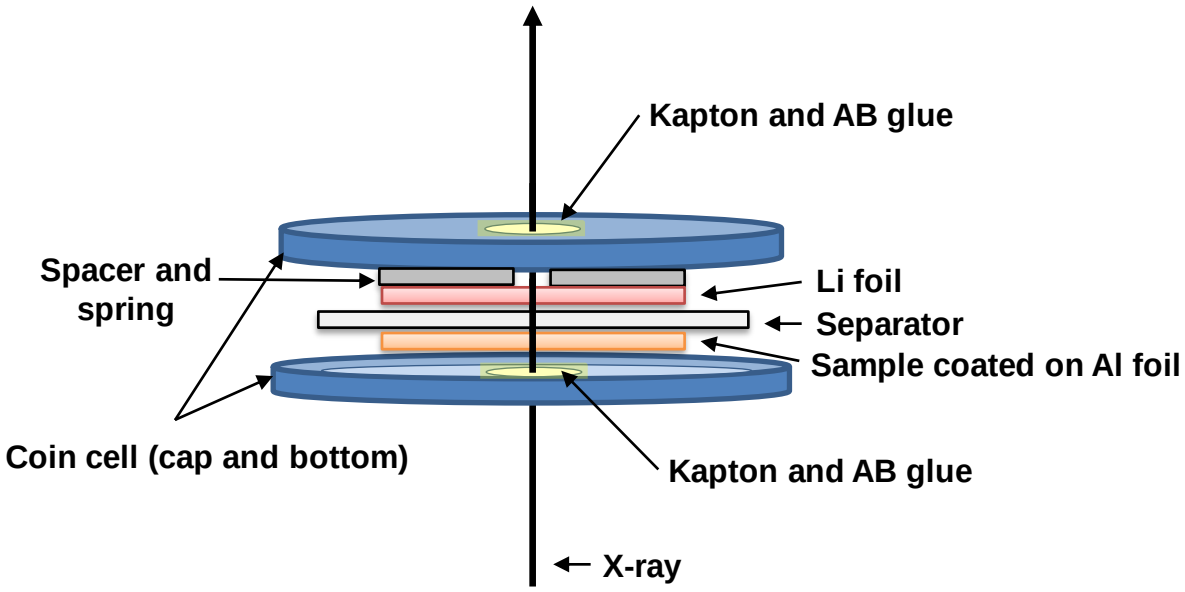

Figure 3.4 Schematic sketch of the in situ XAS cell. (Reproduced from my published paper by permission of The Royal Society of Chemistry: http://pubs.rsc.org/en/content/articlelanding/2017/cp/c6cp05768c..)

The XANES spectra recorded the edge jumps for V of $Na_6[V_{10}O_{28}]$ electrodes. The $Na_6[V_{10}O_{28}]$ electrodes were discharged from open circuit voltage (3.0 V vs. Li/Li^+) to 2.75, 2.40, 2.25, and 1.75 V vs. Li/Li^+ and then charged to 2.25, 2.60, 3.00, 4.00 V vs. Li/Li^+ at a constant current (I = 25 mA g^{-1}). When the potentials reached to the desired potentials, the currents were set to zero for the measurement (each measurement took ~ 40 minutes).

The post-edge background of XANES spectra were subtracted and normalized. Extended X-ray absorption fine structure (EXAFS) were analyzed by standard procedures as following: the EXAFS oscillation function $k^3\chi(k)$ (k: the photoelectron wavenumber) was acquired by subtracting the post-edge background from the overall absorption (cubic spine), and normalization with respect to the edge jump step; k^3-weighted $\chi(k)$ data was Fourier transformed to r-space with the

k-space ranging from 3.5 to 12.0 $Å^{-1}$ for the V K-edge. V_2O_5 and VO_2 were used as reference material to calculate the structural parameters such as the coordination numbers and bond distance.

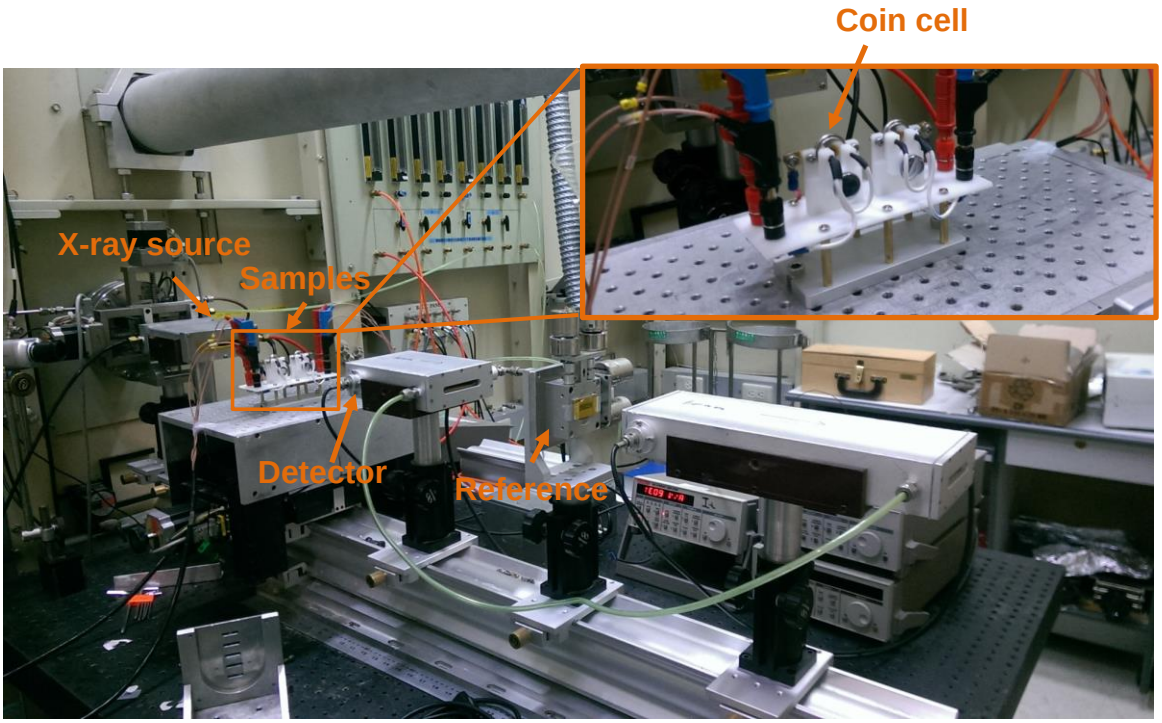

Figure 3.5 The set-up of in-situ XAS measurement at the National Synchrotron Radiation Research Center (NSRRC), Hsinchu, Taiwan

Chapter 4 Results

4.1 $Na_6[V_{10}O_{28}]$ as Electrode Material for Supercapacitors and Li-ion batteries

In this research, we propose for the first time the utilization of the vanadium-based POM material decavanadate(V), $Na_6[V_{10}O_{28}]$ as electrode material in SCs and LIBs. The polyhedral representation for the $[V_{10}O_{28}]^{6-}$ molecular cluster is shown in **Figure 4.1(a)**.

According to the performance of V_2O_5 which provides relatively high specific capacitance due to the multiple oxidation states (V^{2+}~V^{5+}), vanadium-based POMs are proposed as potential electrode materials which might provide high specific capacitance and high energy density of SCs in this study.[122,123] Furthermore, the theoretical capacity of $Na_6[V_{10}O_{28}]$ cathode in LIB is 245 mAh g^{-1} which assumes full reduction of V(5+) to V(4+). This theoretical capacity of $Na_6[V_{10}O_{28}]$ electrode is much higher than other common LIB cathode materials such as $LiCoO_2$ (137 mAh g^{-1}) and $LiFePO_4$ (170 mAh g^{-1}).

The electrochemical properties of $Na_6[V_{10}O_{28}]$ electrodes used in SCs and LIBs are analysed by electrochemical measurements such as GCD and CV. Also, an asymmetric SC device which combines commercial AC as positive electrode and $Na_6V_{10}O_{28}$ as negative electrode is fabricated to demonstrate the potential for SC applications. Furthermore, most of the POM SCs utilize acidic aqueous electrolyte, which restricts the operating voltage of the SC to ~ 1 V.[39] Thus, a Li-ion-containing organic electrolyte (1 M $LiClO_4$ in propylene carbonate (PC)) is employed to extend the potential window in order to increase high energy density and power density of $Na_6[V_{10}O_{28}]$ SCs.

4.1.1 Material characterization of $Na_6[V_{10}O_{28}]$

$Na_6[V_{10}O_{28}]$ is characterized by FTIR and ^{51}V NMR. As shown in **Figure 4.1 (b)**, the ^{51}V NMR spectrum of $[V_{10}O_{28}]^{6-}$ solution shows characteristic signals at −514 ppm, −500 ppm and −424 ppm which identifies the three different V environments in $[V_{10}O_{28}]^{6-}$ polyanion**,** similar to the results in the literature.[21,25,116,124] The FTIR spectrum shown in **Figure 4.1 (c)** detects the characteristic absorption bands of $Na_6[V_{10}O_{28}]$. The vibrational mode centered at 956 cm^{-1} is assigned to a V=O bond.[125] The bands located at 837, 746, and 576 cm^{-1} are attributed to V-O-V bridging as characterized for $[V_{10}O_{28}]^{6-}$ in previous studies.[125]

Figure 4.1 (d) shows the N_2 adsorption-desorption isotherms of $Na_6[V_{10}O_{28}]$, and the Brunauer-Emmett-Teller (BET) surface area of 21 $m^2\ g^{-1}$ is obtained. As shown in the inset of **Figure 4.1 (d)**, the Barrett-Joyner-Halenda (BJH) pore size distribution of $Na_6[V_{10}O_{28}]$ shows the pore diameters ranging from ~ 3 nm to ~ 160 nm, and most of these pores show a narrower distribution of mesopores centered between 3 and 5 nm.

The scanning electron microscopy (SEM) images of powder $Na_6[V_{10}O_{28}]$ is shown in **Figure 4.2 (a)** and **(b)**. $Na_6[V_{10}O_{28}]$ shows micro-sized-rods morphological structure with a diameter of 0.5–1 μm and a length of several micrometers. A transmission electron microscope (TEM) is used to further investigate the structure and crystallinity of $Na_6[V_{10}O_{28}]$ rods. A bright-field TEM image of a $Na_6[V_{10}O_{28}]$ rod with a diameter of about 600 nm is shown in **Figure 4.2 (c)**. **Figure 4.2 (d)** is the high resolution transmission electron microscopy (HRTEM) image of an individual rod which provides further insight into the structure. The $Na_6[V_{10}O_{28}]$ rod shows polycrystallinity in random orientation with d-spacings of 0.333 nm and 0.769 nm which are consistent with ICSD data file 66807.

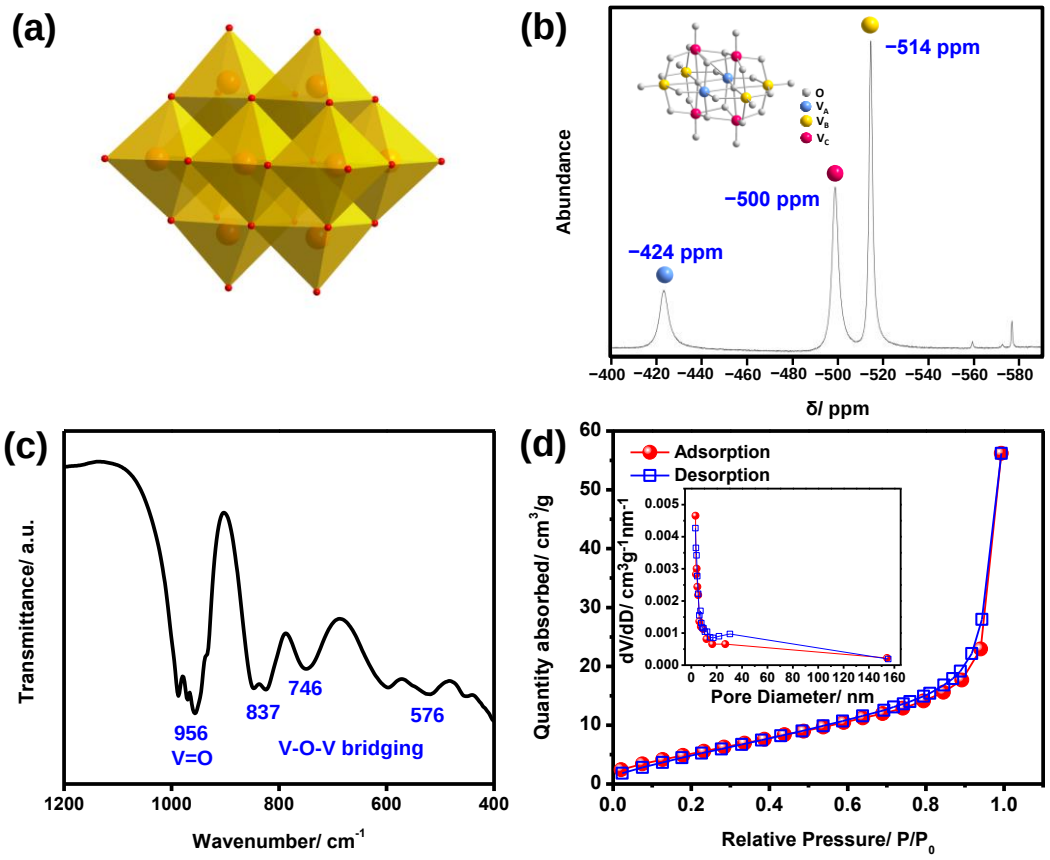

Figure 4.1 (a) Polyhedral representation for structure of $[V_{10}O_{28}]^{6-}$ polyanion. (Reproduced from my published paper by permission of PCCP Owner Societies. http://pubs.rsc.org/en/content/articlelanding/2017/cp/c6cp05768c.[126]) (b) ^{51}V NMR spectrum, (c) FTIR spectrum, and (d) BET graph of $Na_6[V_{10}O_{28}]$. Inset in (b) is the polyhedral representation of $[V_{10}O_{28}]^{6-}$. Inset in (c) is the corresponding BJH pore size distribution curve for $Na_6[V_{10}O_{28}]$ determined by N_2 adsorption-desorption isotherms. (Han-Yi Chen et al.: "A Polyoxovanadate as an Advanced Electrode Material for Supercapacitors". ChemPhysChem 2014, 15, 2162–2169. Copyright Wiley-VCH Verlag GmbH & Co. KGaA. Reproduced with permission[20])

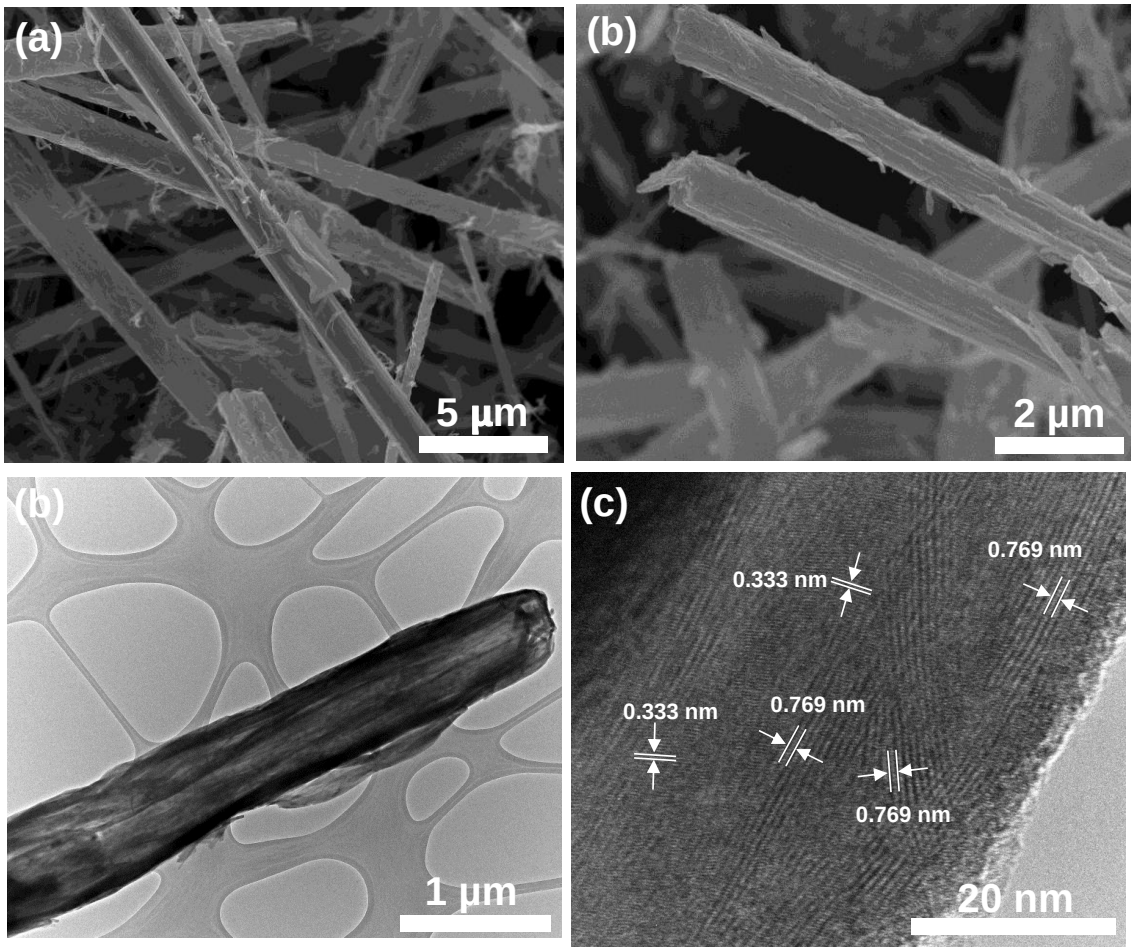

Figure 4.2 (a) and (b) The SEM image of $Na_6V_{10}O_{28}$ powder. (c) A bright-field TEM image of a $Na_6V_{10}O_{28}$ rod, and (d) a high-resolution TEM image. (Han-Yi Chen et al.: "A Polyoxovanadate as an Advanced Electrode Material for Supercapacitors". ChemPhysChem 2014, 15, 2162–2169. Copyright Wiley-VCH Verlag GmbH & Co. KGaA. Reproduced with permission[20])

4.1.2 Electrochemical properties of $Na_6[V_{10}O_{28}]$ electrodes in three-electrode configuration SCs

In order to investigate the electrochemical performance of $Na_6[V_{10}O_{28}]$ as electrode material for SCs in 1 M $LiClO_4$ in PC, three-electrode CV and GCD measurements were employed. An $Ag/AgNO_3$ reference electrode (approximately 0.55 V vs. NHE,[127] supporting electrolyte for reference electrode is 0.1 M tetraethylammonium tetrafluoroborate ($TEABF_4$) and 0.01 M $AgNO_3$ in acetonitrile) and a Pt wire counter

electrode were utilized. The CV curves of a $Na_6[V_{10}O_{28}]$ electrode measured from −1.6 V to 1.2 V vs. $Ag/AgNO_3$ at various scan rates (20, 10, 5, and 2 mV s^{-1}) are shown in **Figure 4.3 (a)**. The CV curves deviating from the rectangular shape of an ideal capacitor indicates faradaic processes.[18] The redox peaks are broader at higher scan rates showing slower kinetics.[61] Oxidation peaks can be observed at -0.17 V and 0.45 V at scan rate of 2 mV s^{-1}, corresponding reduction peaks at −0.78 V, −0.53 V, −0.02 V and 0.37 V. These peaks are attributed from the redox reactions of vanadium ions and intercalation or adsorption of Li^+ ions into the $Na_6[V_{10}O_{28}]$ structure. The evidence for this statement will be provided later in the discussion session. The gravimetric specific capacitance of $Na_6[V_{10}O_{28}]$ electrodes calculated from CV curves at various scan rates are shown in **Figure 4.3 (b)**. The following equation is used to calculate the specific capacitances from the CV curves:[128]

$$C_{sp} = \frac{\int i\Delta t}{\Delta U \times m} = \frac{q}{\Delta U \times m} \quad (4.1)$$

where C_{sp} is the gravimetric specific capacitance (F g^{-1}), q is the charge obtained by integrating the negative currents (discharging cycle) after subtracted the charge from current collector (graphite paper), ΔU is the potential range (V), and m is the mass of the active materials on the electrodes (g). The specific capacitance of 121, 142, 170, and 223 F g^{-1} are obtained for 20, 10, 5, and 2 mV s^{-1} from the CV curves of $Na_6V_{10}O_{28}$ electrodes, respectively.

The specific capacitances obtained from GCD measurements in the potential range from −1.6 V to 1.2 V at current densities ranging from 10 to 0.1 A g^{-1} are also shown in **Figure 4.3 (c)** and **(d)**. The pseudocapacitive behaviour can be observed from the nonlinear charge/discharge profile, and the potential positions of the plateaus are similar with the redox peaks observed in the CV curves. The specific capacitance is calculated according to the following equation:[129]

$$C_{sp} = \frac{I \times \Delta t}{m \times \Delta U} \qquad (4.2)$$

where I is the constant current (A), and Δt is discharge time (s), respectively.

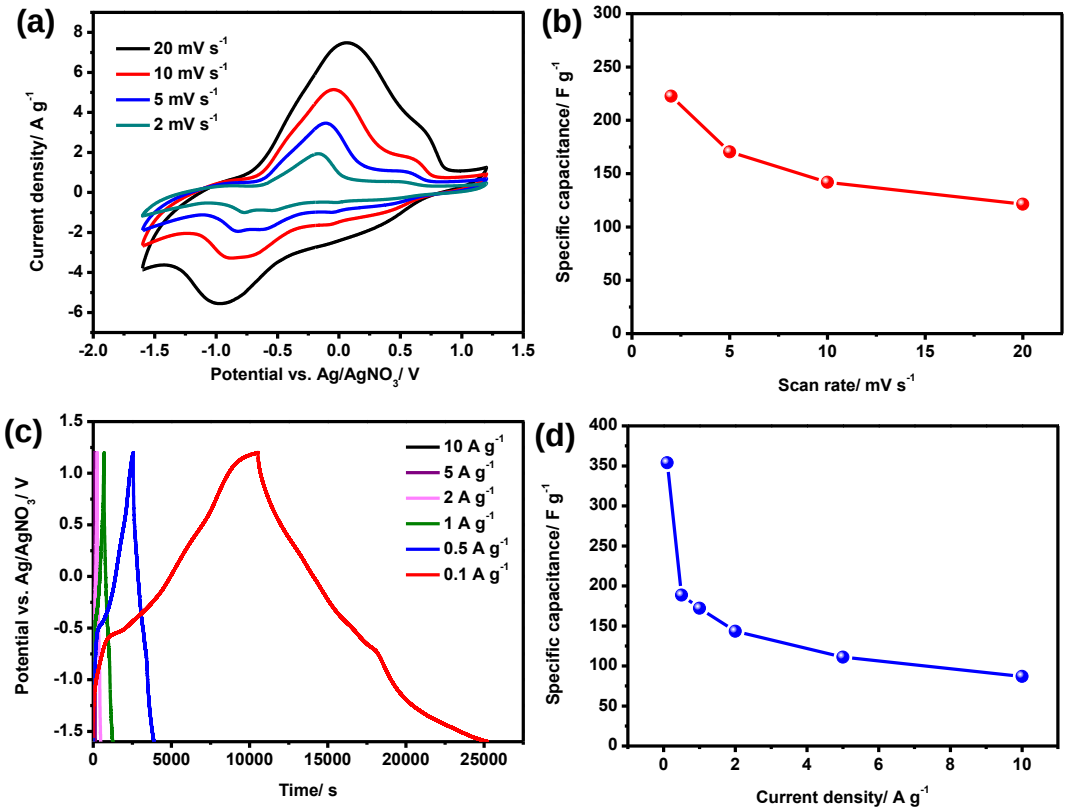

Figure 4.3 Electrochemical characterizations of $Na_6[V_{10}O_{28}]$ electrodes in 1 M $LiClO_4$/PC in a three-electrode configuration with Pt wire as the counter electrode and $Ag/AgNO_3$ as the reference electrode: (a) cyclic voltammograms and (b) the specific capacitance at various scan rates (20, 10, 5, and 2 mV s^{-1}); (c) galvanostatic charge-discharge curves at current density of 0.1 A g^{-1}, and (d) the specific capacitance at various current densities (10, 5, 2, 1, 0.5, and 0.1 A g^{-1}). (Han-Yi Chen et al.: "A Polyoxovanadate as an Advanced Electrode Material for Supercapacitors". ChemPhysChem 2014, 15, 2162–2169. Copyright Wiley-VCH Verlag GmbH & Co. KGaA. Reproduced with permission[20])

The specific capacitance calculated from GCD at current density of 10, 5, 2, 1, 0.5, and 0.1 A g^{-1} are 87, 111, 143, 172, 189, and 354 F g^{-1}, respectively. The decrease of the specific capacitance with increasing scan rate and current density in **Figure 4.3 (b)** and **(d)** can be

explained as: (1) Low electrical conductivity of thick $Na_6[V_{10}O_{28}]$ electrode (~ 40 μm) leads to a large ohmic drop during fast charging/discharging.[7,123] (2) Slow diffusion of Li^+ ion into the pores of $Na_6[V_{10}O_{28}]$. The charge storage only occurs at the outer active surface due to the restriction of Li^+ ion diffusion at high current density and high scan rate. On the contrary, all the active surface area can be utilized to store charge at low current density and low scan rate, resulting in higher specific capacitance.[7,122]

4.1.3 Asymmetric supercapacitor based on $Na_6[V_{10}O_{28}]$ and activated carbon

Asymmetric SCs are fabricated using AC as the positive electrode and $Na_6[V_{10}O_{28}]$ as the negative electrode in $LiClO_4$-containing organic electrolyte in order to demonstrate the potential of $Na_6[V_{10}O_{28}]$ electrodes for practical device applications. During the charging process, Li ions are inserted into or adsorbed onto the $Na_6[V_{10}O_{28}]$ (negative electrode) with partial reduction of V^{5+} to V^{4+}, while ClO_4^{-1} ions are adsorbed onto the porous structure of AC (positive electrode). During the discharging process, Li ions are extracted or desorbed from the $Na_6[V_{10}O_{28}]$ and adsorbed onto the porous structure of AC, while the ClO_4^{-1} ions are adsorbed onto the $Na_6[V_{10}O_{28}]$.

The mass ratio and the voltage range of $Na_6[V_{10}O_{28}]$ and AC electrodes are optimized in order to obtain the maximum gravimetric cell energy of asymmetric SCs. The CV curves of AC, $Na_6[V_{10}O_{28}]$, and graphite paper (blank substrate) at 10 mV s^{-1} in three-electrode configuration are shown in **Figure 4.5 (a)**. The CV curve of AC shows a near-ideal rectangular shape, indicating nearly pure electrochemical double layer charging. The potential regions of $Na_6V_{10}O_{28}$ as negative electrode and AC as positive electrode were found between −1.6 V to 1.2 V vs. $Ag/AgNO_3$. Thus, the asymmetric SCs were performed in the voltage window of 0 V to 2.8 V. The mass ratio was optimized based on the equation:

$$q_+ = q_- \left(C_{sp+} m_+ \Delta U_+ = C_{sp-} m_- \Delta U_-\right) \quad (4.3)$$

where + represents positive electrode, − represents negative electrode.[123,130] The specific capacitances of $Na_6[V_{10}O_{28}]$ and AC are calculated from the CV curves at a scan rate of 10 mV s^{-1} after subtracting the blank capacitance generated from the graphite paper in **Figure 4.5 (a)**. The specific capacitances of $Na_6[V_{10}O_{28}]$ and AC were 142 and 109 F g^{-1}, respectively. An optimized mass ratio of AC : $Na_6[V_{10}O_{28}]$ = 1.3 : 1 is selected for the asymmetric device based on the above data.

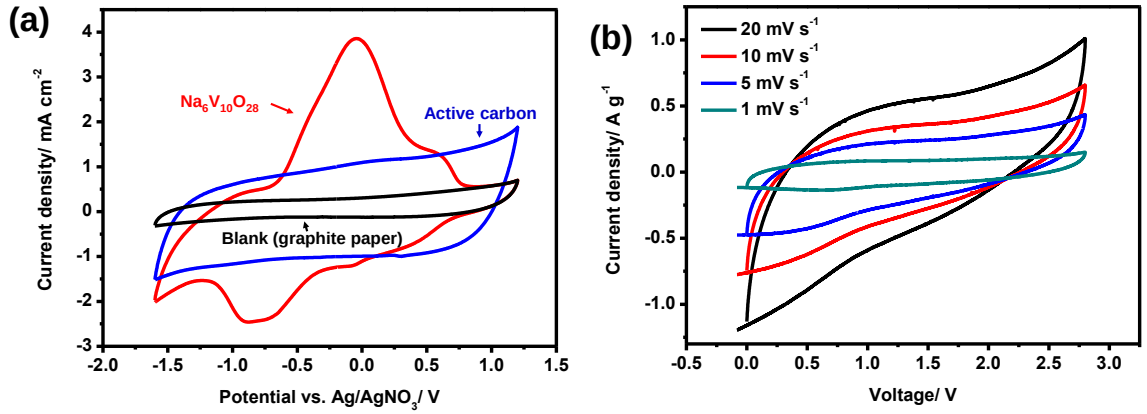

Figure 4.5 (a) Cyclic voltammograms of AC, $Na_6[V_{10}O_{28}]$, and graphite paper (blank electrode) measured at 10 mV s^{-1} in a three-electrode configuration. (b) Cyclic voltammograms of AC//$Na_6[V_{10}O_{28}]$ asymmetric SC at the mass ratio of m_+/m_-=1.3 : 1 in different scan rates (20, 10, 5, and 1 mV s^{-1}). (Han-Yi Chen et al.: "A Polyoxovanadate as an Advanced Electrode Material for Supercapacitors". ChemPhysChem 2014, 15, 2162–2169. Copyright Wiley-VCH Verlag GmbH & Co. KGaA. Reproduced with permission[20])

Figure 4.5 (b) and **Figure 4.6** display the electrochemical performance of AC//$Na_6[V_{10}O_{28}]$ asymmetric SC with the optimized mass ratio of 1.3 : 1 in the voltage window of 0 V to 2.8 V. The CV curves of AC//$Na_6[V_{10}O_{28}]$ asymmetric SC in various scan rates (20, 10, 5, and 1 mV s^{-1}) are shown in **Figure 4.5 (b)**. The CV curves of the AC//$Na_6[V_{10}O_{28}]$ asymmetric SC deviate from an ideal rectangular shape, indicating that

faradaic reactions from the $Na_6[V_{10}O_{28}]$ electrode add pseudocapacitance to the capacitance stemming from the electrochemical double layer.[130]

The GCD profile at current densities of 0.5 A g^{-1} (mass based on the negative electrode) is shown in Figure 4.6 (a), and the slopes of the charge/discharge curves are not strictly linear. This illustrates that electrochemical performance of the AC//$Na_6[V_{10}O_{28}]$ asymmetric SC is a combination of pseudocapacitance and double-layer capacitance.[130] The specific capacitance (C_{sp}) of the asymmetric and symmetric SCs can be calculated from the equation.[63]

$$C_{sp} = \frac{2C_e}{m} \quad (4.4)$$

where m is the mass of the active materials in negative electrode (g), and C_e is the experimental capacitance calculated from the equation.[63]

$$C_e = \frac{I \times \Delta t}{\Delta U} \quad (4.5)$$

The comparison of specific capacitance and Ragone plots of AC//$Na_6[V_{10}O_{28}]$ asymmetric SC and AC//AC symmetric SC at various current densities are shown in **Figure 4.6 (b)** and **(c)**. The specific capacitance of The AC//$Na_6[V_{10}O_{28}]$ asymmetric SC are 80, 104, 152, 203, and 269 F g^{-1} at current densities of 10, 5, 2, 1, and 0.5 A g^{-1}, respectively, which are significantly higher than for the AC//AC symmetric SC. The specific capacitances are smaller at high current densities for both AC//$Na_6[V_{10}O_{28}]$ asymmetric SC and AC//AC symmetric SC as expected.[17] A detailed analysis of AC//AC symmetric SC will not be investigated here. Nevertheless, the diminishing specific capacitance of AC//AC symmetric SC at higher current density is mainly attributed to the mass transfer limitation of Li^+ ions inside porous AC structure.[7,131]

The specific capacitance of AC//$Na_6[V_{10}O_{28}]$ asymmetric SC decreases even more quickly with increasing current density. It might result from the relatively low electrical conductivity of $Na_6[V_{10}O_{28}]$ or from the kinetics of the redox-reactions which are not fast enough to deal with the high rates.[7] **Figure 4.6 (c)** illustrates the Ragone plot generated from the energy and power densities at various current densities for the two SC devices. The following equations are utilized to calculate the energy and average power densities obtained during the discharge:[123,130]

$$E = \frac{1}{2}\frac{C_e}{M}\Delta U^2 \quad (4.6)$$

$$P = \frac{\mathrm{E}}{\Delta \mathrm{t}} \quad (4.7)$$

where M is the total mass of the active material in both positive and negative electrodes. Both energy density and power density of the AC//$Na_6V_{10}O_{28}$ asymmetric SC are significant higher than the AC//AC symmetric SC from the Ragone plot. The maximum energy density of 73 Wh kg^{-1} with a power density of 312 W kg^{-1} can be achieved from the AC//$Na_6V_{10}O_{28}$ asymmetric SC, while the energy density of AC//AC symmetric SC is around 51 Wh kg^{-1} with similar power density. The energy density of AC//$Na_6[V_{10}O_{28}]$ asymmetric SC still exhibits a higher energy density of 22 Wh kg^{-1} than the AC//AC symmetric SC (~ 13 Wh kg^{-1}) even at the power density of 6238 W kg^{-1}, indicating that $Na_6[V_{10}O_{28}]$ is a promising electrode with organic electrolyte for SC applications.

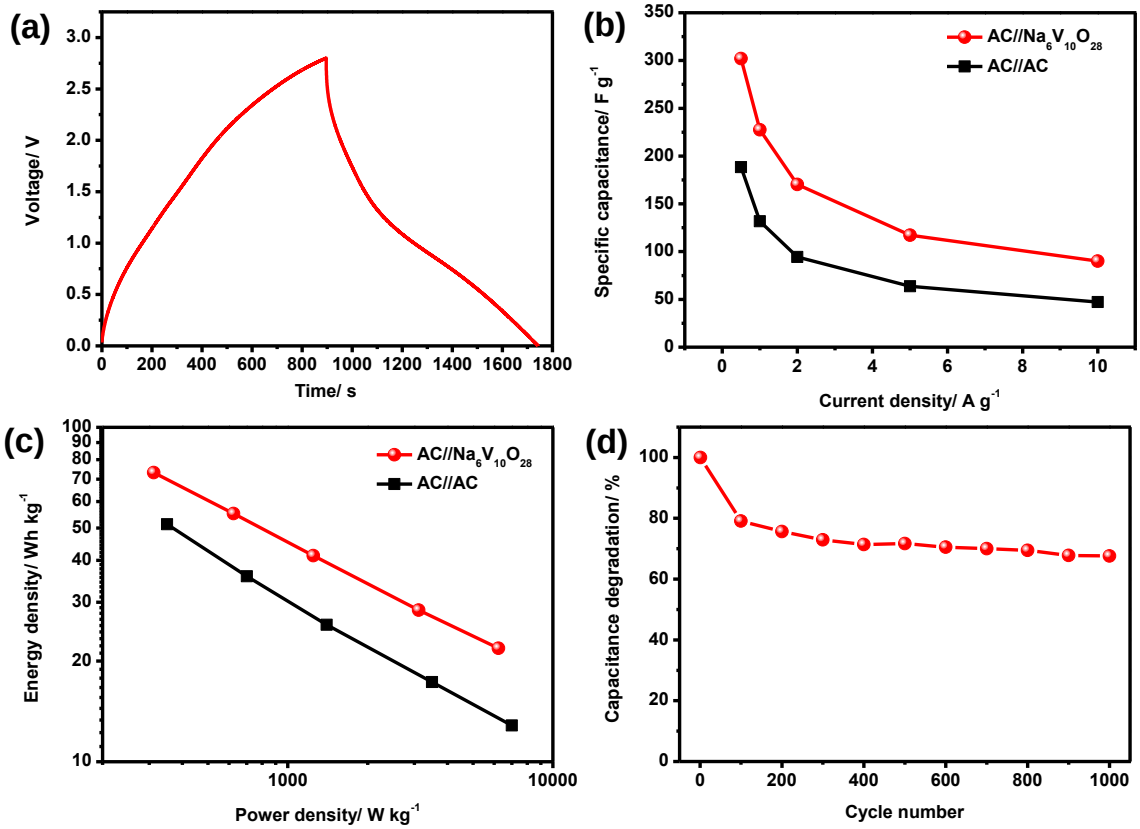

Figure 4.6 Electrochemical performance of AC//$Na_6[V_{10}O_{28}]$ asymmetric SC at the mass ratio of m_+/m_-=1.3 : 1. (a) Galvanostatic charge-discharge curves at a current densities of 0.5 A g^{-1}. (b) The specific capacitance and (c) the Ragone plots of the AC//$Na_6[V_{10}O_{28}]$ asymmetric SC and AC//AC symmetric SC as contrast at different current densities of 10, 5, 2, 1, and 0.5 A g^{-1}. (d) Capacitance retention of AC//$Na_6[V_{10}O_{28}]$ asymmetric SC at 1 A g^{-1}. (Han-Yi Chen et al.: "A Polyoxovanadate as an Advanced Electrode Material for Supercapacitors". ChemPhysChem 2014, 15, 2162–2169. Copyright Wiley-VCH Verlag GmbH & Co. KGaA. Reproduced with permission[20])

Figure 4.6 (d) displays the capacitance retention of an AC//$Na_6[V_{10}O_{28}]$ asymmetric SC tested between 0 and 2.8 V with charge-discharge cycling measurement at a current density of 1 A g^{-1}. In the first 100 cycles, the capacitance decreases about 20 %, following by slowly decreasing ~ 1 % per 100 cycles. The AC//$Na_6[V_{10}O_{28}]$ asymmetric SC exhibited moderate cycle stability with capacitance retention around 70 % after 1000 cycles.

The energy density and power density of AC//$Na_6[V_{10}O_{28}]$ asymmetric SC developed in this work and other POM/polymer or POM/CNT hybrid SCs from the literatures are summarized in **Figure 4.7**.[19,63,65] The AC//$Na_6[V_{10}O_{28}]$ asymmetric SC in this study exhibits the highest energy density and power density in 1 M $LiClO_4$ in PC as compared to other POM SCs, demonstrating $Na_6[V_{10}O_{28}]$ is a promising electrode material for SC applications.

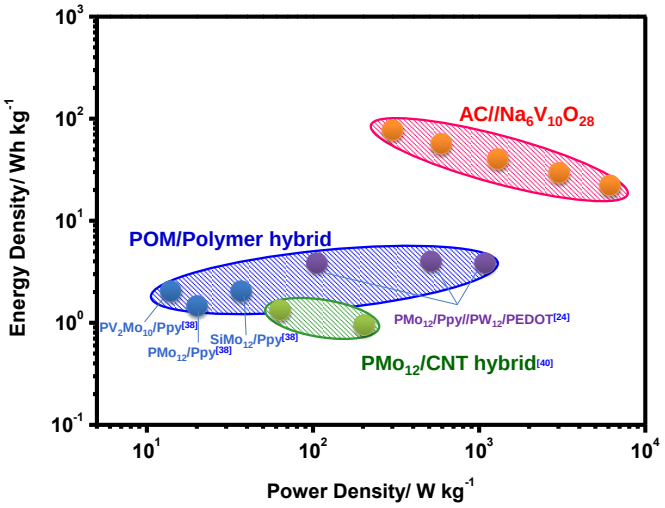

Figure 4.7 The Ragone plot of AC//$Na_6[V_{10}O_{28}]$ asymmetric SC compared with other POM SCs.[19,63,65] (PMo_{12}: $H_3PMo_{12}O_{40}$, $SiMo_{12}$: $H_4SiMo_{12}O_{40}$, PV_2Mo_{10}: $H_5PV_2Mo_{10}O_{40}$, PW_{12}: $H_3PW_{12}O_{40}$). (Han-Yi Chen et al.: "A Polyoxovanadate as an Advanced Electrode Material for Supercapacitors". ChemPhysChem 2014, 15, 2162–2169. Copyright Wiley-VCH Verlag GmbH & Co. KGaA. Reproduced with permission[20])

4.1.4 LIBs performance of $Na_6[V_{10}O_{28}]$ electrodes

In order to understand the electrochemical properties of $Na_6[V_{10}O_{28}]$ electrode in LIB half-cell configuration, CV was carried out at a scan rate of 0.1 mV s^{-1} as shown in **Figure 4.8 (a)**. The main oxidation peaks are located at 3.73 V, 2.90 V, 2.65 V, and 2.21 V vs. Li/Li^+, corresponding

reduction peaks can be observed at 3.71 V, 2.75 V, 2.40 V, and 2.24 V vs. Li/Li^+. It exhibits high reversibility and stability after 20 cycles.

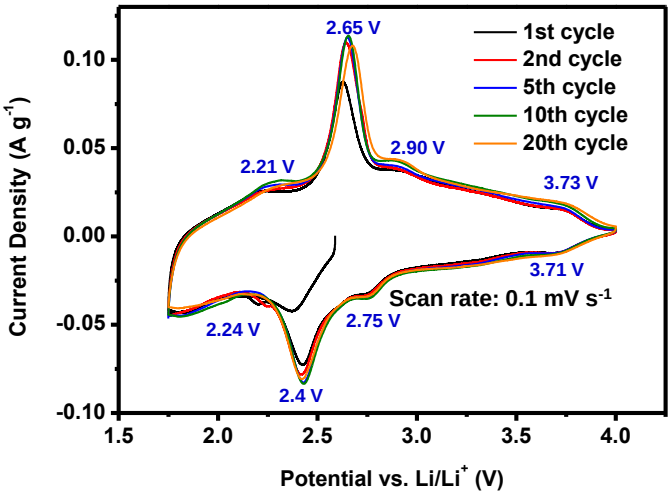

Figure 4.8 Cyclic voltammograms of $Na_6[V_{10}O_{28}]$ electrodes in 1 M $LiPF_6$/EC:DEC (1:1) in a half-cell configuration with Li metal as counter electrode and reference electrode at 0.1 mV s^{-1}.

To test the concept of $Na_6[V_{10}O_{28}]$ used as cathode in LIBs that retain their capacity better than commonly used intercalation compounds, we performed GCD cycling at different current densities. **Figure 4.9 (a)** shows the GCD curves of initial 10 cycles at the current density of 15 mA g^{-1}. One well-defined and three indistinct plateaus can be observed on the discharge and charge curves which are in close agreement with the CV curves. The electrodes exhibit high capacity of 213 mAh g^{-1} at 15 mA g^{-1}. Nevertheless, the measured capacity is lower than the theoretical capacity of 245 mAh g^{-1} (~ 87 %), which might be caused by the low conductivity of $Na_6[V_{10}O_{28}]$ electrode and the limited accessible pores due to the high thickness (~ 22 μm). The density of the electrode is ~ 76 g cm^3 and the total surface area on the electrode is ~ 0.138 m^2 estimated from BET surface area of $Na_6[V_{10}O_{28}]$ (~ 21 m^2 g^{-1}) and carbon black (Super P, ~ 62 m^2 g^{-1}) where the surface area of PVDF binder can be ignored. After 50 cycles, the $Na_6[V_{10}O_{28}]$ LIBs exhibited high cycling

stability as shown in **Figure 4.9 (b)**. The coulombic efficiency is ~100 % with capacity retention of around 86 % over 50 cycles at a current density of 150 mA g^{-1} as shown in **Figure 4.9 (c)**.

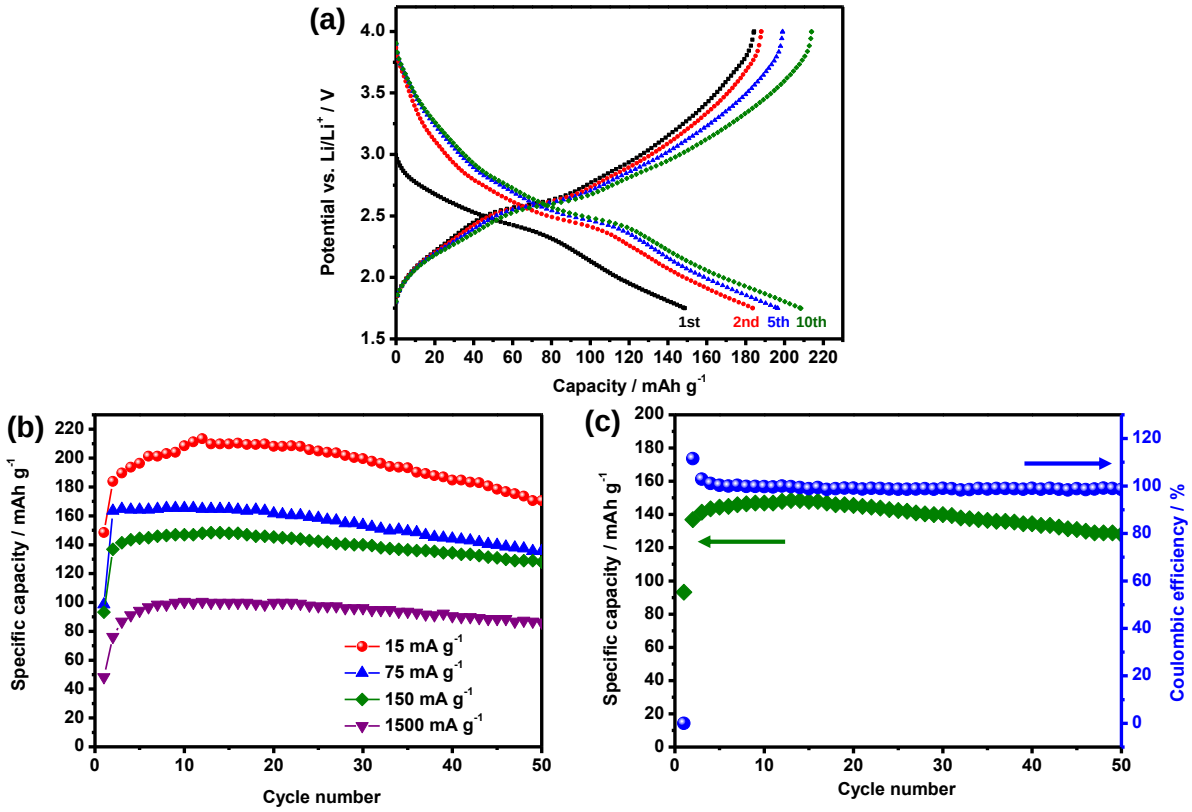

Figure 4.9 Battery performance of $Na_6[V_{10}O_{28}]$ LIBs in 1 M $LiPF_6$/EC:DEC (1:1) in a half-cell configuration with Li metal as counter electrode and reference electrode: (a) the galvanostatic charge-discharge curves at current density of 15 mA g^{-1}; (b) the cycling performance at various densities; and (c) the cycling performance and the coulombic efficiency at current density of 150 mA g^{-1}.

4.1.5 Summary

In this section of this thesis, a polyoxovanadate, $Na_6[V_{10}O_{28}]$, has been demonstrated to be a potential electrode material for SC and LIB applications. The $Na_6[V_{10}O_{28}]$ electrodes in 1 M $LiClO_4$ in PC have been tested in a three-electrode configuration and present a high specific capacitance of 354 F g^{-1} at 0.1 A g^{-1}. In addition, an asymmetric SC device which consisted of

commercial activated carbon (AC) as positive electrode and $Na_6[V_{10}O_{28}]$ as negative electrode was assembled and investigated. The AC//$Na_6[V_{10}O_{28}]$ asymmetric SC provides a high power density of 6238 W kg^{-1} (with a corresponding energy density of 22 Wh kg^{-1}) and high energy density of 73 Wh kg^{-1} (with the power density of 312 W kg^{-1}), exhibiting the highest values of energy and power density among reported POM SCs so far. The AC//$Na_6[V_{10}O_{28}]$ asymmetric SC is cycled up to 1000 cycles with a capacitance retention of ~ 70 %, showing moderate cycling stability. After the first 100 cycles, the decay slowed to ~ 1 % per 100 cycles. $Na_6[V_{10}O_{28}]$ was also utilized and investigated as cathode material for LIB applications, and the $Na_6[V_{10}O_{28}]$ LIBs exhibit high capacity of 213 mAh g^{-1} at 15 mA g^{-1} and display high cycle stability up to 50 cycles with capacity retention of ~ 86 % at 150 mAh g^{-1}.

4.2 A SWCNT-POM Hybrid Material as Electrode for Supercapacitors

Two methods have been employed to prepare POM/Carbon hybrid materials for SCs so far: sonication and layer-by-layer (LbL) deposition.[7,18,60,61,63] The sonication method is mixing POM solution and Carbon materials by sonication. Single POM molecules are usually adsorbed at defect sites of carbon materials and form monolayers.[18,63] Additional POM molecules are washed out because of the high solubility in aqueous solution. The ratio of chemisorbed POMs is also based on the functionalization degree of the carbon materials.[18,63]

The LbL deposition method utilizes a simple way to prepare POM/Carbon hybrid material by alternating electrostatic adsorption of anionic POMs and cationic polymer on functionalized carbon materials.[7,60,64] Nevertheless, the non-conducting long polymer chain might limit electron hopping from POM to SWCNT which resulting in high resistivity.

Here we report the combination of SWCNTs and $(TBA)_5[PV_2Mo_{10}O_{40}]$ (**TBA-PV_2Mo_{10}**, TBA: $[(CH_3(CH_2)_3)_4N]^+$, tetra-n-butyl ammonium), as electrode material for SCs in acidic aqueous electrolyte (1 M H_2SO_4) for the first time. **TBA-PV_2Mo_{10}** is not soluble in aqueous electrolyte because of its organic cation (TBA) which is different from other POMs used in SCs. Hence, we expect **TBA-PV_2Mo_{10}** has high cycling stability in acidic aqueous electrolyte. Purified SWCNTs with 1−3 atomic% carboxylic acid groups are used as carbon material in this research. The hydrophilic carboxylic acid groups in SWCNTs not only improve the contact with polar aqueous electrolytes, but also provide pseudocapacitance. The anionic $[PV_2Mo_{10}O_{40}]^{5-}$ are electrostatically attached to the SWCNTs through the organic TBA cations. Therefore, it is even simpler to prepare **SWCNT-TBA-PV_2Mo_{10}** nanohybrid material by solution process compared with sonication and LbL methods. The alkyl chains of TBA are much shorter than of cationic polymers,[7,60,64] so it shortens the electron-hoping distance between POMs and SWCNTs.

The concept of **SWCNT-TBA-PV_2Mo_{10}** is combining pseudocapacitance mainly contributed from **TBA-PV_2Mo_{10}** and double-layer capacitance mainly contributed from SWCNTs. **TBA-PV_2Mo_{10}** provides redox reactions and benefits from the conducting properties of the SWCNTs at the same time that increase both energy and power density.

4.2.1 Material characterization of TBA-PV_2Mo_{10}

TBA-PV_2Mo_{10} is synthesized and characterized by ^{31}P NMR, ^{51}V NMR, FTIR, and UV-Vis spectroscopy. The phosphorous and vanadium atoms in the $[PV_2Mo_{10}O_{40}]^{5-}$ structure can be analyzed by ^{31}P NMR and ^{51}V NMR in solution as shown in **Figure 4.10 (a)** and **(b)**. The NMR spectra show the characteristic signals of $[PV_2Mo_{10}O_{40}]^{5-}$ (^{31}P NMR: δ −2.2 ppm, −1.6 ppm; ^{51}V NMR: δ −532 ppm, −544 ppm, −551 ppm, and −554 ppm) which are consistent with literature.[132]

The FTIR spectrum of **TBA-PV_2Mo_{10}** is displayed in **Figure 4.10 (c)**. As reported for the Keggin unit in literature, the FTIR characteristic absorption bands located at 1055 cm^{-1}, 952 cm^{-1}, 880 cm^{-1}, and 802 cm^{-1} can be appointed to P-O, M=O (M: Mo, V), inter-octahedral M−O−M, and intra-octahedral M−O−M vibrations, respectively.[118,133-136] The C−H bending bond contributed from TBA ($[(CH_3(CH_2)_3)_4N]^{5+}$) can be found in the absorption bands located at 1381 and 1483 cm^{-1}. The representation of **TBA-PV_2Mo_{10}** is shown in the inset of **Figure 4.10 (c)**. **Figure 4.10 (d)** recorded the UV-Vis spectrum of **TBA-PV_2Mo_{10}** and the absorption band observed at 305 nm is contributed from Mo^{6+} in octahedral position at a ligand metal charge transfer state.[133]

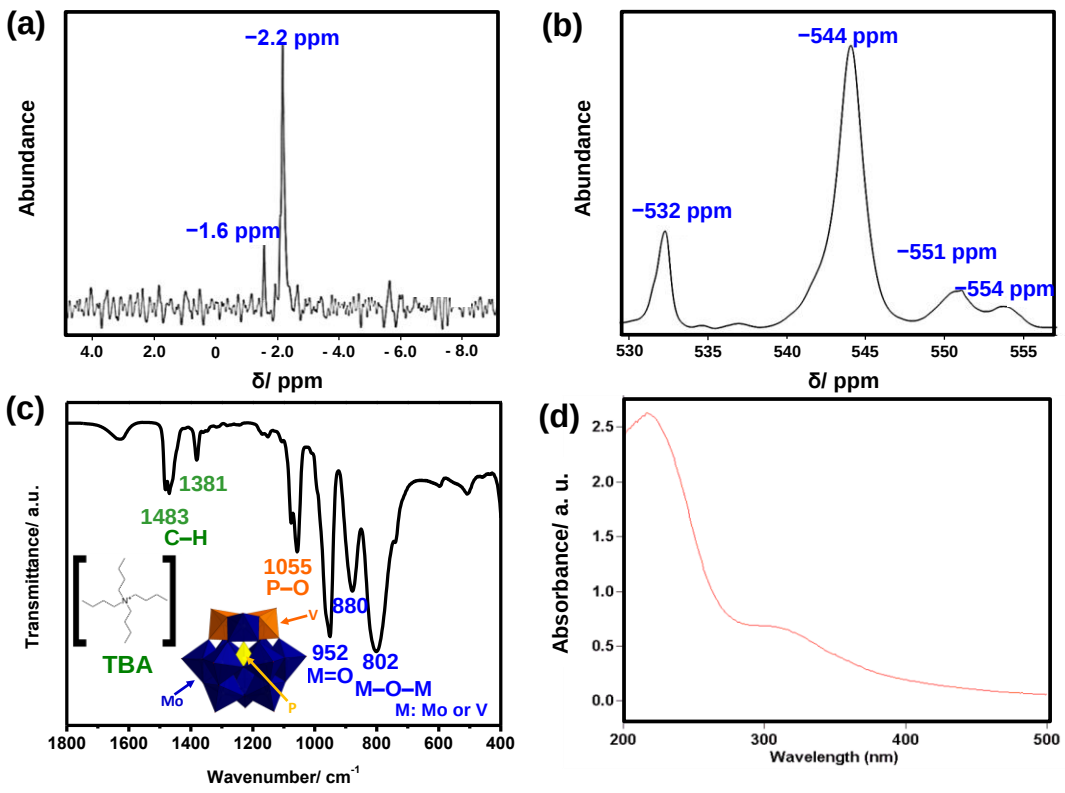

Figure 4.10 (a) ^{31}P NMR spectrum, (b) ^{51}V NMR spectrum, (c) FTIR spectrum, and (d) UV-Vis spectrum of **TBA-PV$_2$Mo$_{10}$**. Inset in (c) is the representation of **TBA-PV$_2$Mo$_{10}$**. (Reproduced from my published paper by permission of The Royal Society of Chemistry: http://pubs.rsc.org/en/content/articlelanding/2015/nr/c4nr07528e.[21])

4.2.2 Material characterization of SWCNT-TBA-PV$_2$Mo$_{10}$ material

A simple solution method was utilized to prepare the **SWCNT-TBA-PV$_2$Mo$_{10}$** hybrid material as described in the experimental section. The insoluble nature of **TBA-PV$_2$Mo$_{10}$** in aqueous electrolyte enables the **SWCNT-TBA-PV$_2$Mo$_{10}$** nanohybrid material not limited to form monolayers of POM onto SWCNTs. Therefore, the ratio of **TBA-PV$_2$Mo$_{10}$** and carbon material in the nanohybrid material can be optimized.

The optimum precursor weight ratio was determined to be 30 wt % **TBA-PV$_2$Mo$_{10}$** and 70 wt % SWCNTs after varying several weight ratios of SWCNTs and **TBA-PV$_2$Mo$_{10}$**. After preparation, the weight percentage of **TBA-PV$_2$Mo$_{10}$** in **SWCNT-TBA-PV$_2$Mo$_{10}$** material was

confirmed to be around 30 wt % by TGA analysis as shown in **Figure 4.11 (a)**, proving that all **TBA-PV_2Mo_{10}** molecules are attached to SWCNTs.

The FTIR spectra of SWCNT, **TBA-PV_2Mo_{10}**, and **SWCNT-TBA-PV_2Mo_{10}** are displayed in **Figure 4.11 (b)**. The vibrational modes of $[PV_2Mo_{10}O_{40}]^{5-}$ polyanion (P-O: 1055 cm^{-1}, M=O: 952 cm^{-1}, and M−O−M: 880, 802 cm^{-1}) present in the nanohybrid material which indicate the successful combination of POM and SWCNT.

Figure 4.11 (c) shows the BET measurement of the surface areas for SWCNT, **TBA-PV_2Mo_{10}**, and **SWCNT-TBA-PV_2Mo_{10}** by N_2 adsorption-desorption isotherms. The surface areas obtained from BET measurement of SWCNT, **TBA-PV_2Mo_{10}**, and **SWCNT-TBA-PV_2Mo_{10}** are 157, 5, and 71 $m^2\ g^{-1}$, respectively. The SWCNT-matrix helps disperse the **TBA-PV_2Mo_{10}** over a larger interface area, thus the surface area of **SWCNT-TBA-PV_2Mo_{10}** is much higher than pure **TBA-PV_2Mo_{10}**. It also indicates the possibility of this **SWCNT-TBA-PV_2Mo_{10}** nanohybrid material to deliver substantial double layer capacitance.

Figure 4.12 (a) displays a HRTEM image of as-received SWCNTs which presents an average diameter of ~ 1.4 nm for one individual tube. Those SWCNTs tend to bundle together with average bundle diameters of 4-10 nm. A SEM image and a bright-field TEM image of **SWCNT-TBA-PV_2Mo_{10}** nanohybrid material are shown in **Figure 4.12 (b)** and **(c)**. From the images, the **TBA-PV_2Mo_{10}** recrystallizes on the surface of the SWCNTs which exhibit nanoparticle agglomerates with a diameter of 20–500 nm. The SWCNTs connect those POM nanoparticles together and perform as an electrically conductive network. Furthermore, as shown in the TEM image, nano-sized black spots (~1.5 nm, highlighted with red circles) which can be considered to be **TBA-PV_2Mo_{10}** single molecules are attached on the surface of SWCNTs separately.[51] The HRTEM image shown in the **Figure 4.12 (d)** provides further insights into the crystal structure of the **TBA-**

PV_2Mo_{10} nanoparticles. The d-spacings of the **TBA-PV_2Mo_{10}** nanoparticles are 0.24 nm, 0.48 nm, and 1.5 nm, showing polycrystallinity in random orientation.

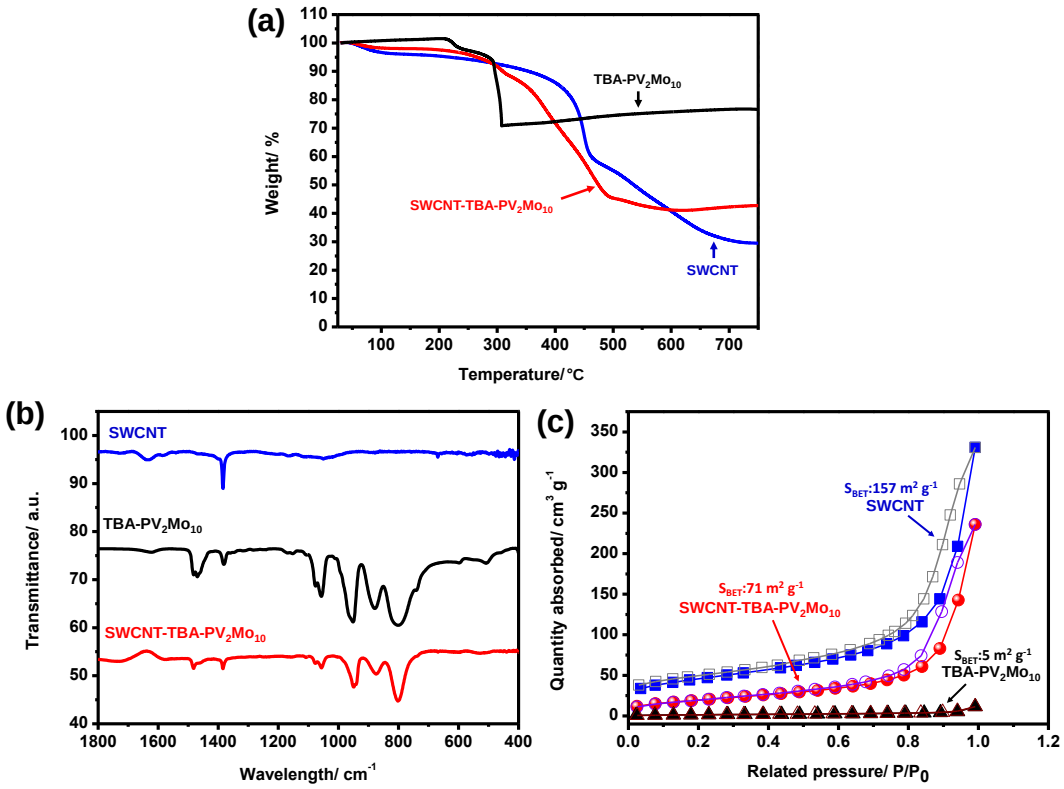

Figure 4.11 (a) TGA analyses, (b) FTIR spectrum, and (c) BET graph of SWCNT, **TBA-PV_2Mo_{10}**, and **SWCNT-TBA-PV_2Mo_{10}** nanohybrid. (Reproduced from my published paper by permission of The Royal Society of Chemistry: http://pubs.rsc.org/en/content/articlelanding/2015/nr/c4nr07528e.[21])

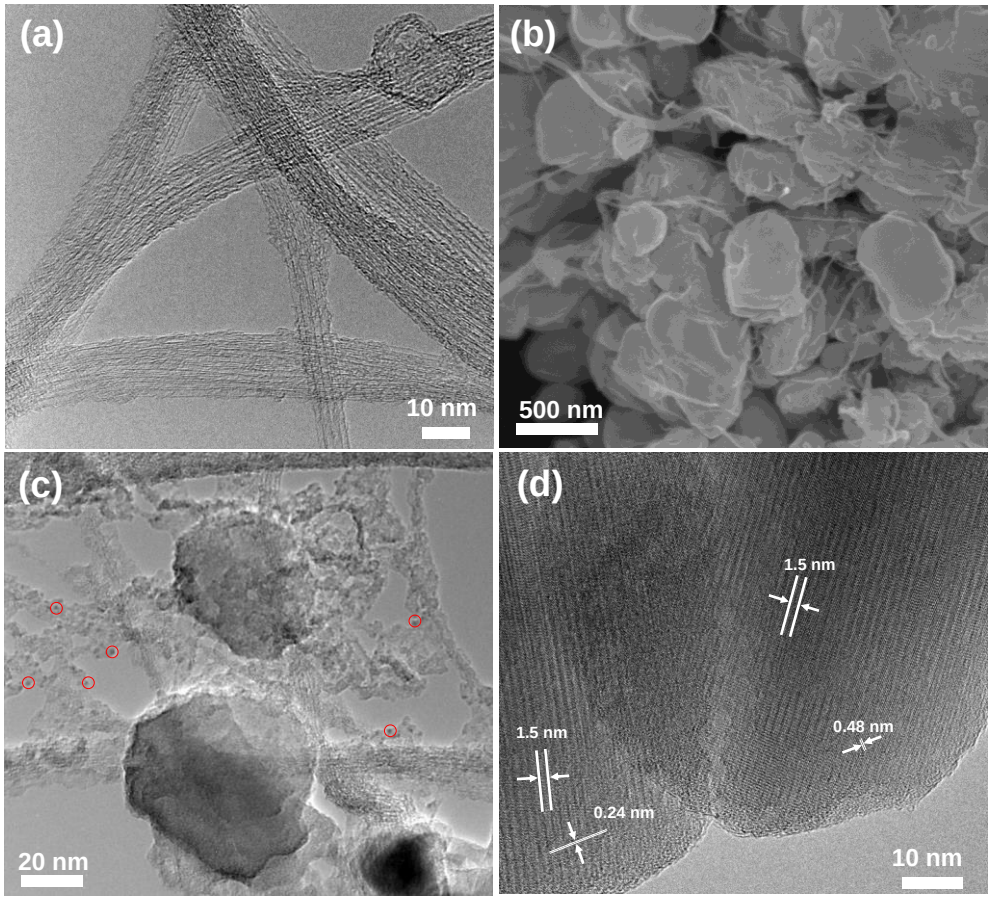

Figure 4.12 (a) HRTEM image of as received SWCNTs. (b) SEM image, (c) the bright-field TEM image, and (d) HRTEM image of **SWCNT-TBA-PV_2Mo_{10}** nanohybrid. (Reproduced from my published paper by permission of The Royal Society of Chemistry: http://pubs.rsc.org/en/content/articlelanding/2015/nr/c4nr07528e.[21])

4.2.3 Electrochemical performance of SWCNT-TBA-PV_2Mo_{10} electrode

In order to demonstrate the potential of **SWCNT-TBA-PV_2Mo_{10}** electrodes for practical device applications, **SWCNT-TBA- PV_2Mo_{10}** symmetric SCs are fabricated. Graphite paper (GP), as the commonly used current collector, was utilized in these SC devices. However, GP also generates current which cannot be ignored in acidic aqueous electrolyte. Hence, we calculated the specific capacitance based on both the geometric working area and the mass. The GCD curves of GP, SWCNT, and **SWCNT-TBA- PV_2Mo_{10}** symmetric SCs at current densities of 1 A g^{-1} (mass

based on single electrode) in 1 M H_2SO_4 are presented in **Figure 4.13 (a)**. The ideally double-layer capacitive behavior can be observed from the linear charge/discharge curves of blank electrode (GP) and SWCNT symmetric SCs. The slope of the charge/discharge curve of **SWCNT-TBA-PV_2Mo_{10}** symmetric SC is not exactly linear. This indicates that **SWCNT-TBA-PV_2Mo_{10}** symmetric SC combines double-layer capacitance and pseudocapacitance. The following equations are utilized to calculate the specific capacitance (C_{sp}) of a symmetric SC:[63]

$$C_{sp}^{A} = \frac{2C}{A} \; or \; C_{sp}^{m} = \frac{2C}{m} \tag{4.8}$$

where A is the geometric surface area, m is the mass of the active materials (SWCNT or **SWCNT-TBA-PV_2Mo_{10}**) in one electrode, and C is the experimental capacitance calculated from the following equation:[61,63]

$$C = \frac{I}{(\frac{dV}{dt})} \tag{4.9}$$

where I is the constant current, V is the potential range, and t is discharge time, respectively.

The specific capacitance calculated based on geometric surface area of GP blank electrodes, SWCNT, and **SWCNT-TBA-PV_2Mo_{10}** at different current densities from 0.1 to 10 mA cm^{-2} are shown in **Figure 4.13 (b)**. Despite the specific capacitance of GP defined in term of geometric working area is significant in acidic aqueous electrolyte, there is apparent improvement contributed from **SWCNT-TBA-PV_2Mo_{10}** material. The specific capacitance of **SWCNT-TBA-PV_2Mo_{10}** symmetric SC are 132, 157, 187, 224, 256, and 317 mF cm^{-2} at current densities of 10, 5, 2, 1, 0.5, and 0.1 mA cm^{-2}, respectively. This shows a much higher specific capacitance than the SWCNT symmetric SC whose specific capacitances are 98, 113, 132, 154, 186, and 231 mF cm^{-2} at current densities of 10, 5, 2, 1, 0.5, and 0.1 mA cm^{-2}, respectively. In average, the specific capacitance of **SWCNT-TBA-PV_2Mo_{10}** symmetric SC is 39 % higher than SWCNT symmetric SC. The improvement of specific capacitance is resulted from the pseudocapacitive contribution

of **TBA-PV_2Mo_{10}** in the nanohybrid.[18] Besides, the specific capacitances are smaller at higher current densities for both SWCNT and **SWCNT-TBA-PV_2Mo_{10}** symmetric SCs.[17] The specific capacitance of SWCNT symmetric SC decreases rapidly with the increasing current density due to the mass transfer limitation of electrolyte ions inside the porous of SWCNTs. The specific capacitance of **SWCNT-TBA-PV_2Mo_{10}** symmetric SC reduces even faster at high current density, which is attributed to the high electrical resistance of **TBA-PV_2Mo_{10}**.[7]

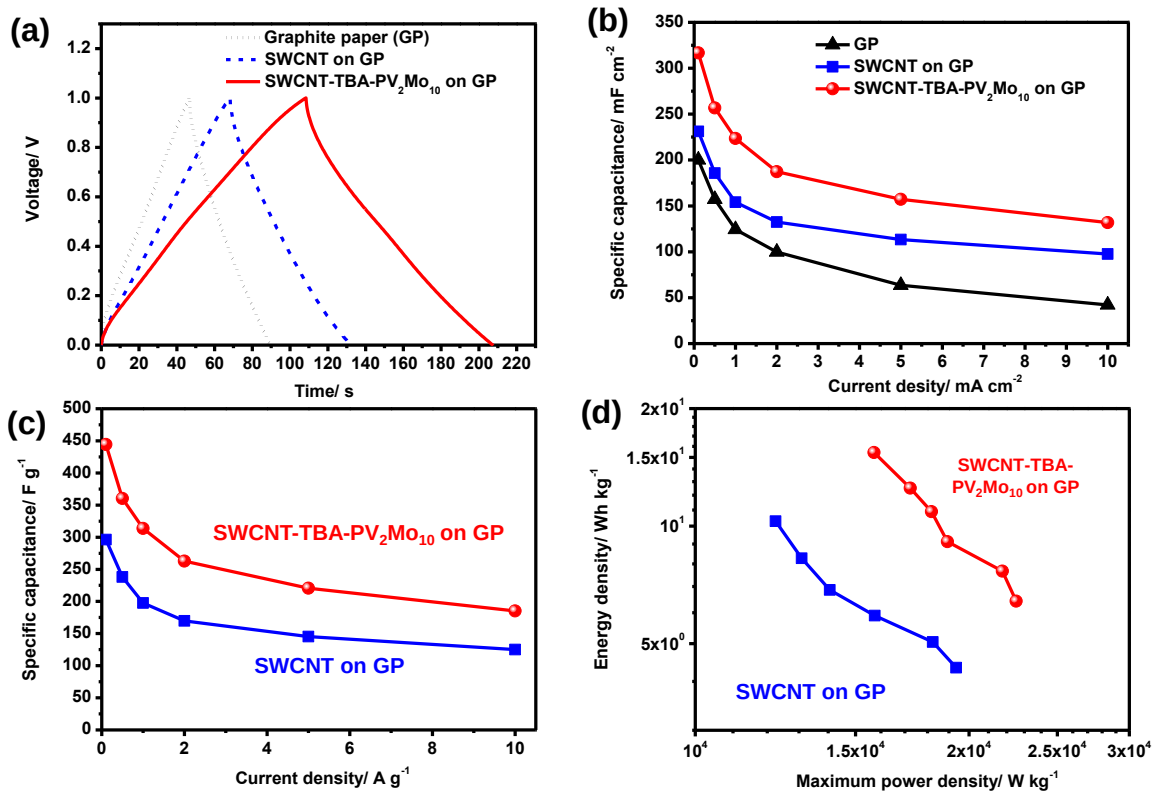

Figure 4.13 Electrochemical performance of SWCNT and **SWCNT-TBA-PV_2Mo_{10}** symmetric SC. (a) Galvanostatic charge-discharge curves at current densities of 1 mA cm^{-2}. (b) The specific capacitance normalized by area at current densities of 0.1-10 mA cm^{-2}. (c) The specific capacitance and (d) the Ragone plots normalized by mass at various current densities of 0.1-10 A g^{-1}. (Reproduced from my published paper by permission of The Royal Society of Chemistry: http://pubs.rsc.org/en/content/articlelanding/2015/nr/c4nr07528e.[21])

Figure 4.13 (c) and **(d)** show the specific capacitances, energy and power densities normalized to the mass of the active material (SWCNT and **SWCNT-TBA-PV_2Mo_{10}**) at different current densities varying from 10 to 0.1 A g^{-1}, respectively. At high current density of 10 A g^{-1}, the specific capacitance of **SWCNT-TBA-PV_2Mo_{10}** symmetric SC is 185 F g^{-1} while the specific capacitance of SWCNT symmetric SC is 125 F g^{-1}. The **SWCNT-TBA-PV_2Mo_{10}** symmetric SC provides a much higher specific capacitance of 444 F g^{-1}, while the specific capacitance of SWCNT symmetric SC is only 236 F g^{-1} at current densities of 0.1 A g^{-1}.

The following equations are used to obtain the energy and maximum power densities: [123,130]

$$E = \frac{1}{2}\frac{C}{M}\Delta V^2 \tag{4.10}$$

$$P_{max} = \frac{\Delta V^2}{4RM} \tag{4.11}$$

where M is the total mass of the active material in both electrodes (kg), and R is the device resistance (Ω). The **SWCNT-TBA-PV_2Mo_{10}** symmetric SC delivers higher energy density than SWCNT symmetric SC at the same power density as shown in the Ragone plots. The maximum energy density of 15.4 Wh kg^{-1} can be achieved from the **SWCNT-TBA-PV_2Mo_{10}** symmetric SC with a power density of 15.7 kW kg^{-1}, while the energy density of SWCNT symmetric SC is ~ 6 Wh kg^{-1} at a similar power density. The **SWCNT-TBA-PV_2Mo_{10}** symmetric SC still exhibits higher energy density of 6.4 Wh kg^{-1} than SWCNT symmetric SC even at a high power density of 22.5 kW kg^{-1}. These results demonstrate that **SWCNT-TBA-PV_2Mo_{10}** is a promising candidate for high power SC applications in acidic aqueous electrolyte.

Figure 4.14 displays the capacitance retention of **SWCNT-TBA-PV_2Mo_{10}** symmetric SC measured in cycling charge-discharge test at current density of 1 A g^{-1}. The capacitance retention of **SWCNT-TBA-PV_2Mo_{10}** symmetric SC exhibits ~ 95 % after 6500 cycles showing an excellent cycle stability. This high cycle stability is mainly contributed by the insoluble nature of **TBA-**

PV_2Mo_{10}. The **SWCNT-TBA-PV_2Mo_{10}** symmetric SC studied in this work exhibits the highest stability and capacitance (calculated based on the mass of the active materials) as compared to other POM SCs with 2-electrode configuration (both symmetric and asymmetric devices) shown in Table 1 (in section 2.1.2.4).

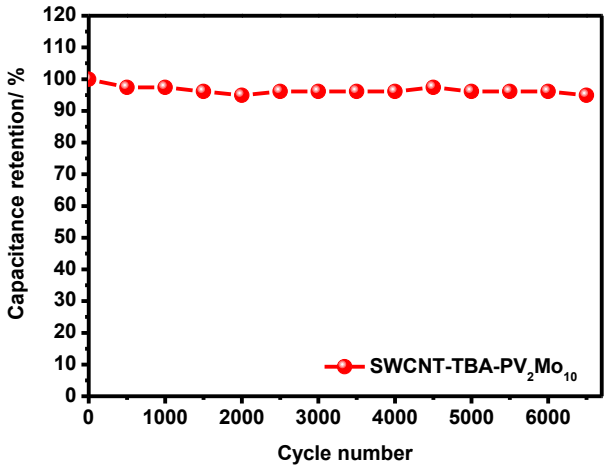

Figure 4.14 Capacitance retention of **SWCNT-TBA-PV_2Mo_{10}** symmetric SC at current densities of 1 A g^{-1}. (Reproduced from my published paper by permission of The Royal Society of Chemistry: http://pubs.rsc.org/en/content/articlelanding/2015/nr/c4nr07528e.[21])

4.2.4 Summary

In this section, a combination of POMs and nanostructured carbon material, **SWCNT-TBA-PV_2Mo_{10}** nanohybrid material, has been synthesized using a simple solution process and has been proved to be a potential electrode material for SCs. The **SWCNT-TBA-PV_2Mo_{10}** symmetric SC in 1 M H_2SO_4 electrolyte presents high specific capacitance of 444 F g^{-1}, high energy density of 15.4 Wh kg^{-1} with high maximum power density of 15.7 W kg^{-1}. The **SWCNT-TBA-PV_2Mo_{10}** symmetric SC also exhibits excellent cycling stability with capacitance retention of ~ 95 % up to 6500 cycles.

4.3 A MWCNT core with graphene oxide nanoribbon shell (MWCNT@GONR) as anode material for sodium ion batteries

Here we present a novel core–shell structure with multi-walled carbon nanotubes (MWCNTs) as the core and graphene oxide nanoribbons (GONRs) as the shell (MWCNT@GONR) as anode material for NIBs. MWCNT@GONR is synthesized utilizing a microwave-assisted process to unzip the MWCNTs. This unique core-shell structure prevents the restacking problem of graphene sheets therefore enabling the penetration of the electrolyte. MWCNT@GONR combines GONRs which provide high surface area and defect sites (carboxylic acid groups, –COOH) that can adsorb more Na^+ on the surface, and MWCNTs which provide excellent electronic conductivity and a direct path for electron transfer. The MWCNT@GONR sample was annealed at various temperatures (300 °C, 600 °C, and 900 °C for 1 hr) to remove functional groups so as to investigate the effect of carboxylic acid groups on Na^+ adsorption. Commercial graphene nanopowder (GNP) and MWCNTs were utilized as anode materials as comparison in this study.

4.3.1 Material characterization of MWCNT@GONR electrode

BET surface area measurements of the MWCNTs and MWCNT@GONR are conducted by N_2 adsorption-desorption isotherms as shown in **Figure 4.15 (a)**. The surface areas obtained from the BET measurements of the MWCNTs and the MWCNT@GONR are 29.3 and 38.2 $m^2\ g^{-1}$, respectively. This demonstrates that the core–shell MWCNT@GONR fabricated from the facile unzipping of MWCNTs by microwave-assisted synthesis presents higher surface area than MWCNT and might lead to attract more Na ion on the surface of MWCNT@GONR. **Figure 4.15 (b)** shows the BJH pore size distribution of

MWCNT and MWCNT@GONR. The pore diameters exhibits a size distribution varying from ~ 3 nm to ~ 120 nm, and most of these pores shows a narrower distribution of mesopores located between 3 and 7 nm.

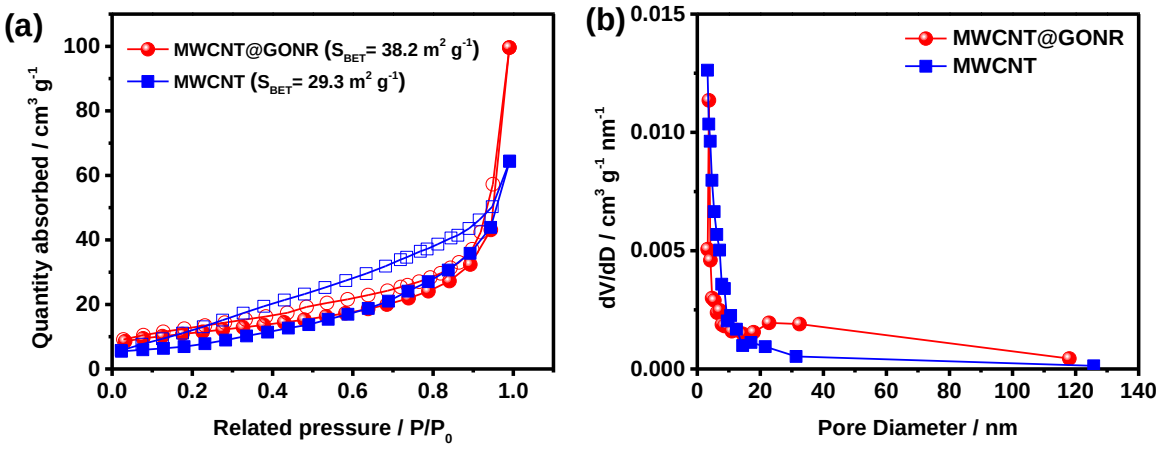

Figure 4.15 (a) BET graph and (b) BJH pore size distribution curve of MWCNT@GONR and MWCNT detected by N_2 adsorption-desorption isotherms, where V represents the total volume and D represents the pore diameter. (Han-Yi Chen et al.: "A Multi-Walled Carbon Nanotube Core with Graphene Oxide Nanoribbon Shell as Anode Material for Sodium Ion Batteries". Adv. Mater. Interfaces 2016, 1600357. Copyright Wiley-VCH Verlag GmbH & Co. KGaA. Reproduced with permission.[137])

Bright-field TEM images of GNP, MWCNT, MWCNT@GONR , MWCNT@GONR annealed at 300 °C for 1 hr (MWCNT@GONR-300°C), MWCNT@GONR annealed at 600 °C for 1 hr (MWCNT@GONR-600°C), and MWCNT@GONR annealed at 900 °C for 1 hr (MWCNT@GONR-900°C) are displayed in **Figure 4.16**. The GNP shows a smooth and planar surface (**Figure 4.16 (a)**), and a tube-like structure (**Figure 4.16 (b)**) is observed for MWCNT as shown in the TEM images. Graphene oxide sheets wrapped around nanotube cores can be observed from the MWCNT@GONR samples, which have maintained their tube-like structure (**Figure 4.16 (c)**). The MWCNT@GONRs still

maintain their morphology even after annealing at 300 °C, 600°C, and 900°C (**Figure 4.16 (d-f)**).

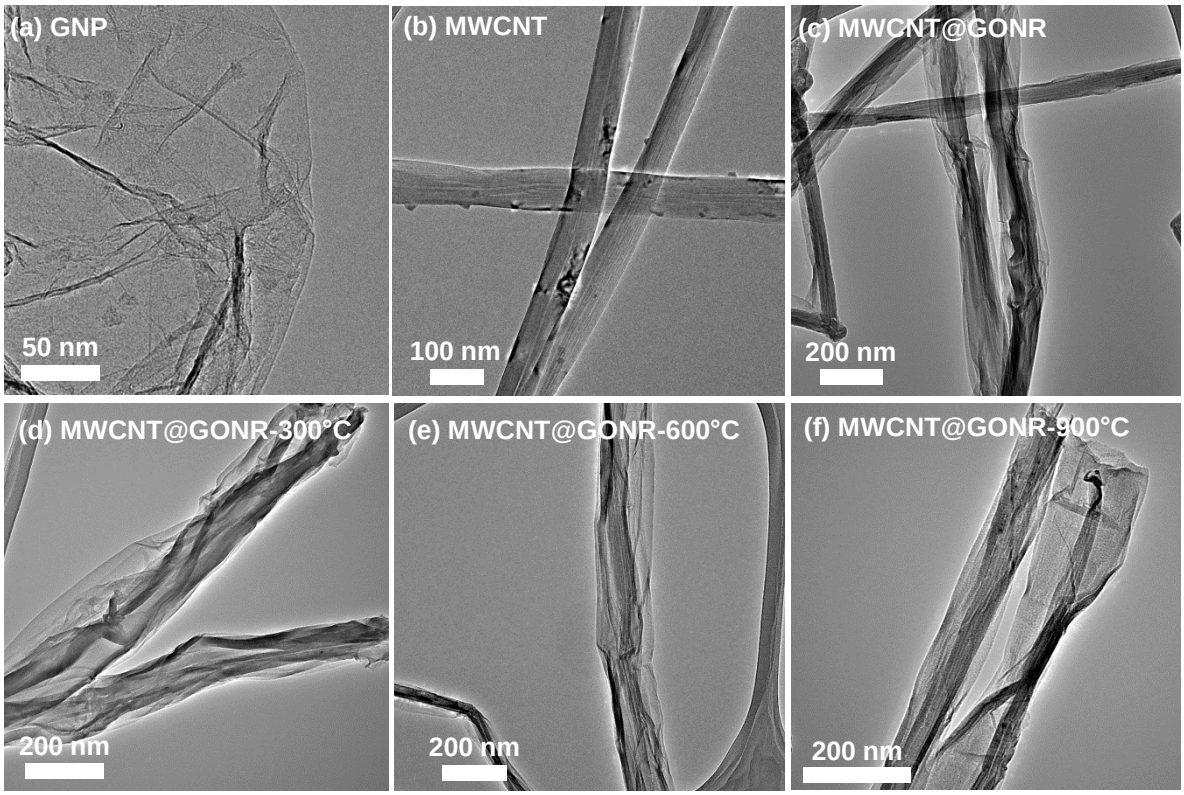

Figure 4.16 TEM images of (a) GNP, (b) MWCNT, (c) MWCNT@GONR, (d) MWCNT@GONR-300°C, (e) MWCNT@GONR-600°C, and (f) MWCNT@GONR-900°C (Han-Yi Chen et al.: "A Multi-Walled Carbon Nanotube Core with Graphene Oxide Nanoribbon Shell as Anode Material for Sodium Ion Batteries". Adv. Mater. Interfaces 2016, 1600357. Copyright Wiley-VCH Verlag GmbH & Co. KGaA. Reproduced with permission.[137])

The scanning electron microscopy (SEM) images of GNP, MWCNT, MWCNT@GONR, MWCNT@GONR-300°C, MWCNT@GONR-600°C, and MWCNT@GONR-900°C can be observed in **Figure 4.17**. The SEM images show that the GNP sheets stack together, while the tube-liked MWCNT interconnect with each other. The MWCNT@GONRs (with and without annealing) present MWCNTs as core and planar graphene sheets surrounding outside of the MWCNTs.

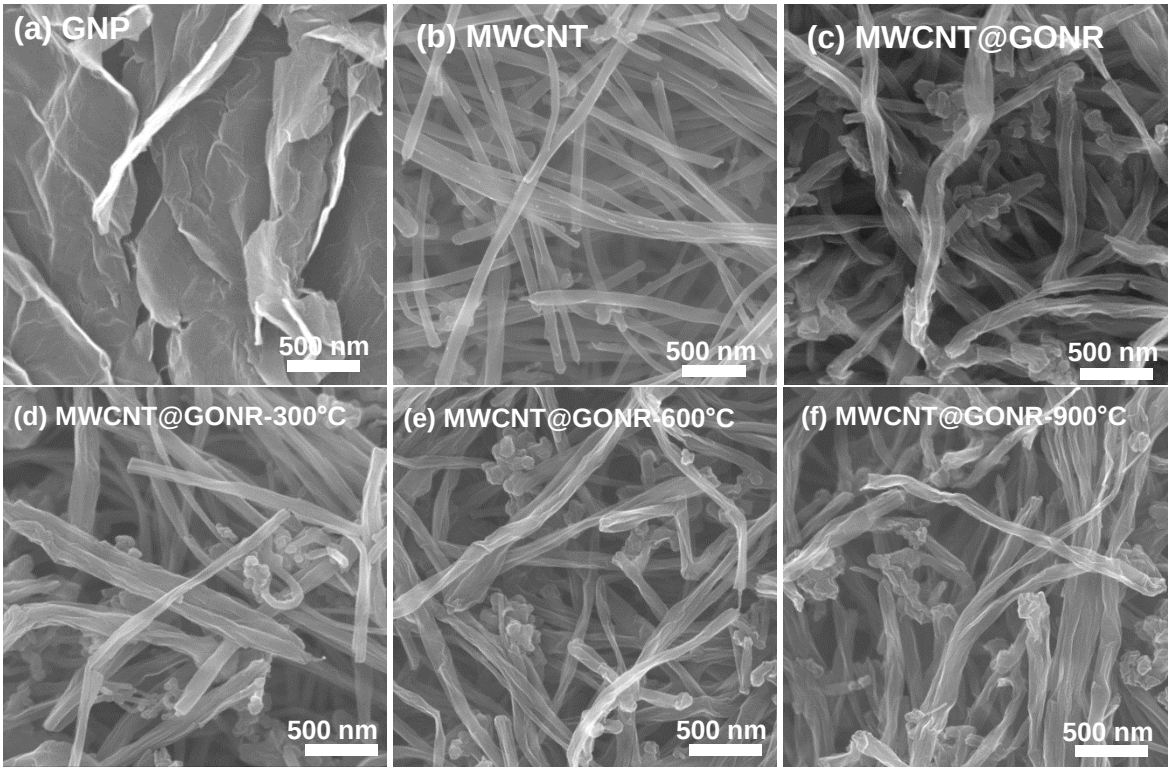

Figure 4.17 FESEM images of (a) GNP, (b) MWCNT, (c) MWCNT@GONR, (d) MWCNT@GONR-300°C, (e) MWCNT@GONR-600°C, and (f) MWCNT@GONR-900°C (Han-Yi Chen et al.: "A Multi-Walled Carbon Nanotube Core with Graphene Oxide Nanoribbon Shell as Anode Material for Sodium Ion Batteries". Adv. Mater. Interfaces 2016, 1600357. Copyright Wiley-VCH Verlag GmbH & Co. KGaA. Reproduced with permission.[137])

The FTIR spectra of the MWCNT, MWCNT@GONR, MWCNT@GONR-300°C, MWCNT@GONR-600°C, and MWCNT@GONR-900°C samples are displayed in **Figure 4.19 (a)**. The peaks located at 1722 cm^{-1} and 3417 cm^{-1} present the stretching C=O and –OH vibration of the carboxylic groups (–COOH) which can be observed for MWCNT@GONR but not in the pristine MWCNT.[138] This demonstrates that the carboxylic groups are created on the surface of MWCNT@GONR during the unzipping process of MWCNT. The peaks of carboxylic groups on MWCNT@GONR-300°C and MWCNT@GONR-600°C can also be detected. Those peaks are missing in the spectrum

of MWCNT@GONR-900°C indicating successful removal of -COOH group by the heat treatment under argon. The aromatic C=C stretch at around 1635 cm^{-1} in the spectra of MWCNT shifts to 1582 cm^{-1} in the spectra of MWCNT@GONRs, which might because of the changes in the MWCNT structure after unzipping processes.[138-141]

TGA spectrum, as shown in **Figure 4.19 (b),** records the weight of samples over temperature under argon for MWCNT, MWCNT@GONR, MWCNT@GONR-300°C, MWCNT@GONR-600°C, and MWCNT@GONR-900°C. The pristine MWCNT sample shows almost no weight loss from the TGA spectrum, implying the absence of functional groups on the surface. A significant weight loss (~ 31 wt %) from ~200 to ~900 °C is observed from the MWCNT@GONR sample showing desorption of functional groups. **Figure 4.19 (c)** shows desorption temperature and the CO and CO_2 signal recorded by a mass spectrometer (MS) indicating that mostly –COOH are present on the surface. MS spectrum exhibits many peaks which indicate a broad distribution of functional groups was generated on the surface of MWCNT@GONR. Those functional groups will be analyzed by XPS later. The weight loss is 26 wt %, 11 wt %, and 2 wt % for MWCNT@GONR-300°C, MWCNT@GONR-600°C, and MWCNT@GONR-900°C, respectively, indicating less functional group on the surface of MWCNT@GONR when the annealing temperature is increased. Only 2 wt % weight loss can be observed in the TGA curve of MWCNT@GONR-900°C implying that the surface functional groups have almost been removed by the annealing at 900 °C. These TGA results correspond to the FTIR results.

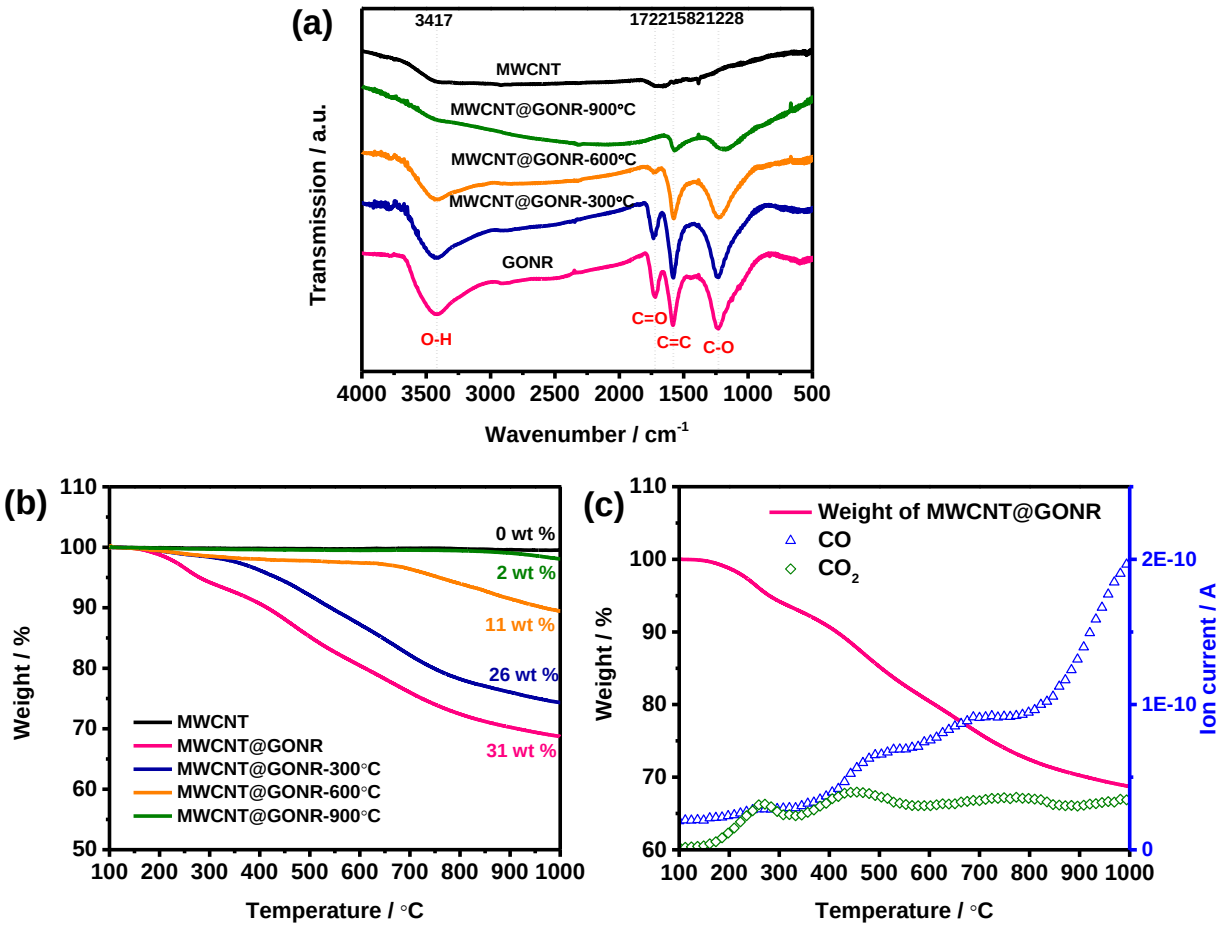

Figure 4.18 (a) FTIR spectrum and (b) TGA spectrum of MWCNT, MWCNT@GONR, MWCNT@GONR-300°C, MWCNT@GONR-600°C, and MWCNT@GONR-900°C; (c) MS spectrum of MWCNT@GONR (Han-Yi Chen et al.: "A Multi-Walled Carbon Nanotube Core with Graphene Oxide Nanoribbon Shell as Anode Material for Sodium Ion Batteries". Adv. Mater. Interfaces 2016, 1600357. Copyright Wiley-VCH Verlag GmbH & Co. KGaA. Reproduced with permission.[137])

Figure 4.19 shows the XPS spectra which are utilized to analyse the surface composition on GNP, MWCNT, MWCNT@GONR, MWCNT@GONR-300°C, MWCNT@GONR-600°C, and MWCNT@GONR-900°C. The corresponding C1s peak spectra with peak binding energies and corresponding atomic percentages of those nanostructured carbon materials are displayed in the XPS spectra.[120] C=C, C–C and C–O

functional groups are observed in all of the nanostructured carbon materials. The numbers after the bonds indicate the atomic ratio as compared to the main C–C peak. High amount of C–O (18.3 %) and extra C=O and O–C=O functional groups can be found in MWCNT@GONR. After annealing, the amount of O-containing functional groups was significantly reduced.

Above FTIR, TGA–MS, and XPS analyses have demonstrated that the unzipping process produces significant amount of O-containing functional groups on the surface of MWCNT@GONR, and the annealing process reduces the amount of O-containing functional groups.

Figure 4.20 shows the XRD patterns of MWCNT, MWCNT@GONR, MWCNT@GONR-300°C, MWCNT@GONR-600°C, and MWCNT@GONR-900°C. An intense peak at $2\theta = 26.2°$ indexed to the (002) reflection can be found in the XRD pattern of the pristine MWCNT. Other diffraction peaks at 2θ of 42.7°, 54.3° and 77.6° are correspond to the (100), (004) and (110) reflections.[138] A MWCNT characteristic peak at 26.2° 2θ (d-spacing ~3.4 Å) and a broad shoulder at 23.7° 2θ (d-spacing ~ 3.8 Å) can be observed in the pattern of MWCNT@GONR, showing large distribution of GONR interlayer spaces with O-containing functional groups surrounding of the MWCNT core. The interlayer spacing of MWCNT@GONR approaches the interlayer spacing of that of MWCNT after annealing due to the removal of O-containing functional groups.[142]

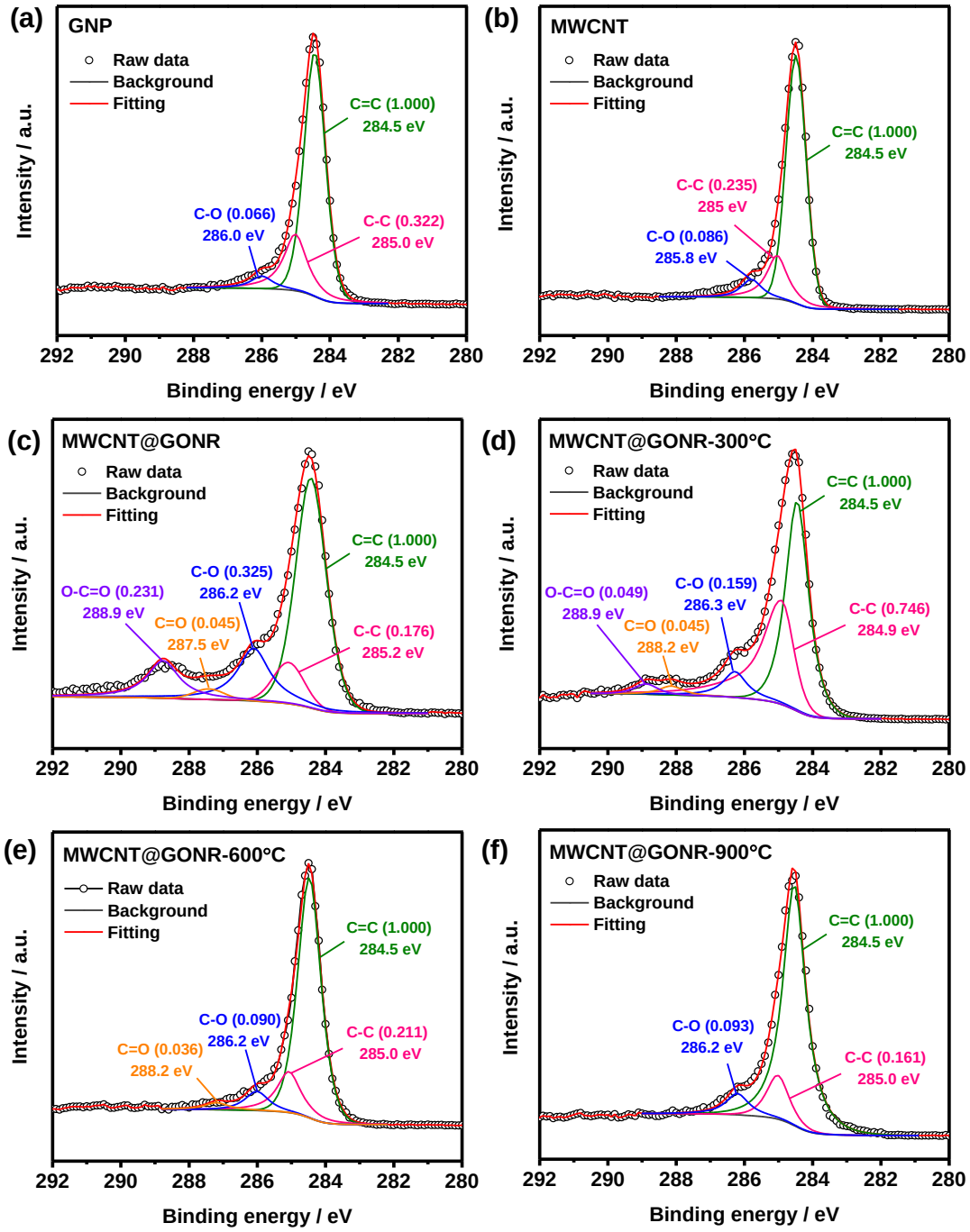

Figure 4.19 XPS spectrum of (a) GNP, (b) MWCNT, (c) MWCNT@GONR, (d) MWCNT@GONR-300°C, (e) MWCNT@GONR-600°C, and (f) MWCNT@GONR-900°C (Han-Yi Chen et al.: "A Multi-Walled Carbon Nanotube Core with Graphene Oxide Nanoribbon Shell as Anode Material for Sodium Ion Batteries". Adv. Mater. Interfaces 2016, 1600357. Copyright Wiley-VCH Verlag GmbH & Co. KGaA. Reproduced with permission.[137])

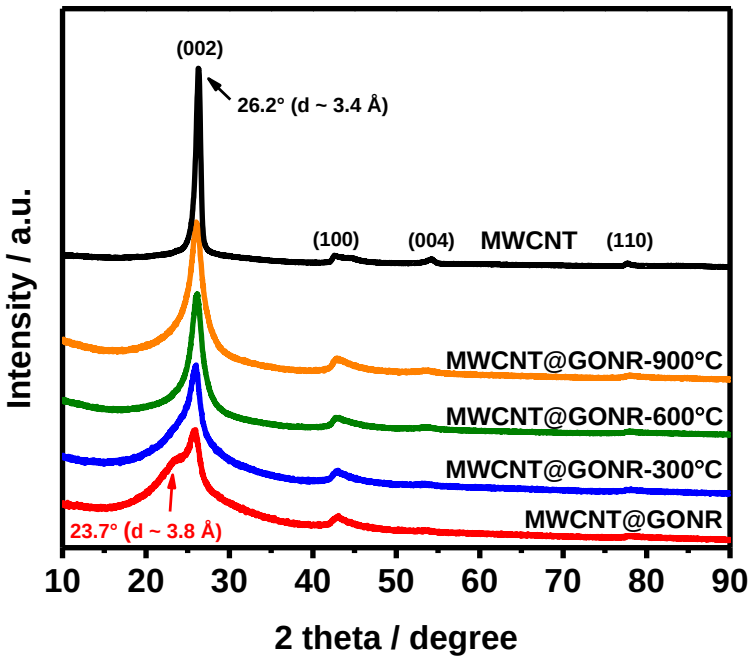

Figure 4.20 XRD spectra of MWCNT, MWCNT@GONR, MWCNT@GONR-300°C, MWCNT@GONR-600°C, and MWCNT@GONR-900°C (Han-Yi Chen et al.: "A Multi-Walled Carbon Nanotube Core with Graphene Oxide Nanoribbon Shell as Anode Material for Sodium Ion Batteries". Adv. Mater. Interfaces 2016, 1600357. Copyright Wiley-VCH Verlag GmbH & Co. KGaA. Reproduced with permission.[137])

Raman Spectroscopy was employed to prove the graphitic character of MWCNT, MWCNT@GONR, MWCNT@GONR-300°C, MWCNT@GONR-600°C, and MWCNT@GONR-900°C as shown in **Figure 4.21.** The ratio of the D-band and G-band intensity (I_D/I_G) is also presented in the Raman spectra where the peak heights are determined by Lorentz curve-fitting. A higher I_D/I_G ratio represents more defect sites on the surface of MWCNT and MWCNT@GONRs. The I_D/I_G ratio of pristine MWCNTs is only 0.1 which reflects low defective graphitic character. The I_D/I_G ratio of

MWCNT@GONR jumps to 0.79 after the unzipping process, indicating highly amount of defects owing to the deterioration of the graphitic structure.[143] Annealing process heals lattice defects on MWCNT-GONR due to the detachment of the O-containing functional groups, hence the I_D/I_G ratio of MWCNT@GONR-300°C and MWCNT@GONR-600°C slightly reduced.[143] The I_D/I_G ratio of MWCNT@GONR-900°C is higher than of MWCNT@GONR-300°C and MWCNT@GONR-600°C, which implies higher amounts of disordered carbon.[144] This might due to the removal of the epoxide group that lead to the in-plane C=C cracking.[144]

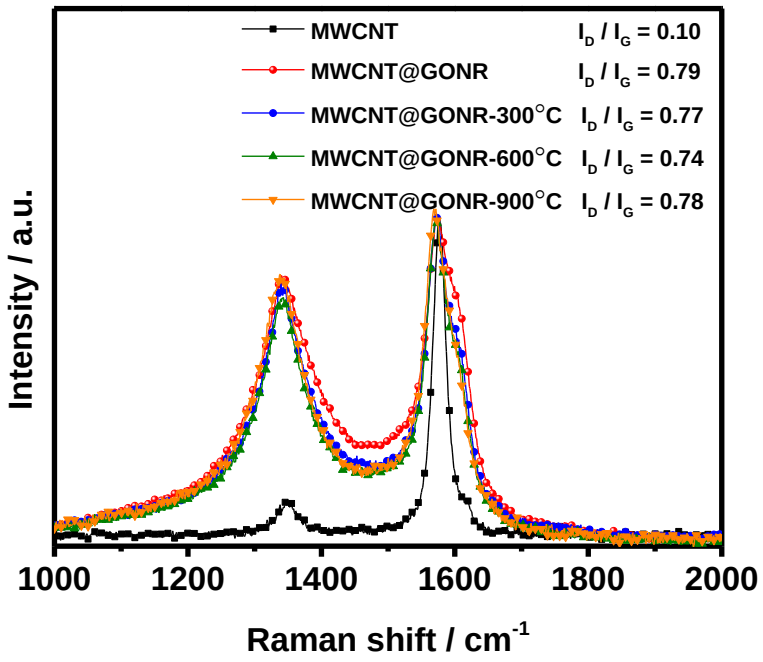

Figure 4.21 Raman spectra of MWCNT, MWCNT@GONR, MWCNT@GONR-300°C, MWCNT@GONR-600°C, and MWCNT@GONR-900°C (Han-Yi Chen et al.: "A Multi-Walled Carbon Nanotube Core with Graphene Oxide Nanoribbon Shell as Anode Material for Sodium Ion Batteries". Adv. Mater. Interfaces 2016, 1600357. Copyright Wiley-VCH Verlag GmbH & Co. KGaA. Reproduced with permission.[137])

4.3.2 Electrochemical performance of MWCNT@GONR electrode in NIBs

The GCD profiles of GNP, MWCNT, MWCNT@GONR, MWCNT@GONR-300°C, MWCNT@GONR-600°C, and MWCNT@GONR-900°C tested at a current density of 50 mA g^{-1} in the first three cycles are shown in **Figure 4.22**. MWCNT@GONR presents a steady insertion of Na^+ in the potential range of 0.005 ~ 2.6 V vs. Na^+/Na in **Figure 4.22 (c)**, while it is not observed in GNP (**Figure 4.22 (a)**) and MWCNT (**Figure 4.22 (b))**. The capacitive behavior with continuous insertion of Na-ions can be observed from these nearly linear charge/discharge curves.[25,27] It lead to a high capacity mainly contributed from the surface defects and functional groups, as well as the core-shell structure which has higher surface area than MWCNT while preventing restacking of graphene sheets.[27,120] The initial columbic efficiency of GNP is only ~11 % which is mainly attributed to the irreversible formation of a SEI layer because of the decomposition of electrolyte on those graphene sheets with large surface areas and the restacking problem.[4,88] A much higher initial columbic efficiency of ~70 % is observed in MWCNT@GONR than GNP, implying the reduction of the restacking problem in graphene with the novel core-shell structure.[120] The capacity in the potential range between 0.75 ~ 2.6 V decreases when increasing the thermal treatment temperature, owing to the reduced defects and functional groups.[145] Nevertheless, this leads to a higher average potential for MWCNT@GONR (at ~ 0.78 V vs. Na/Na^+) than MWCNT@GONR-900°C (at ~ 0.38 V vs. Na/Na^+).

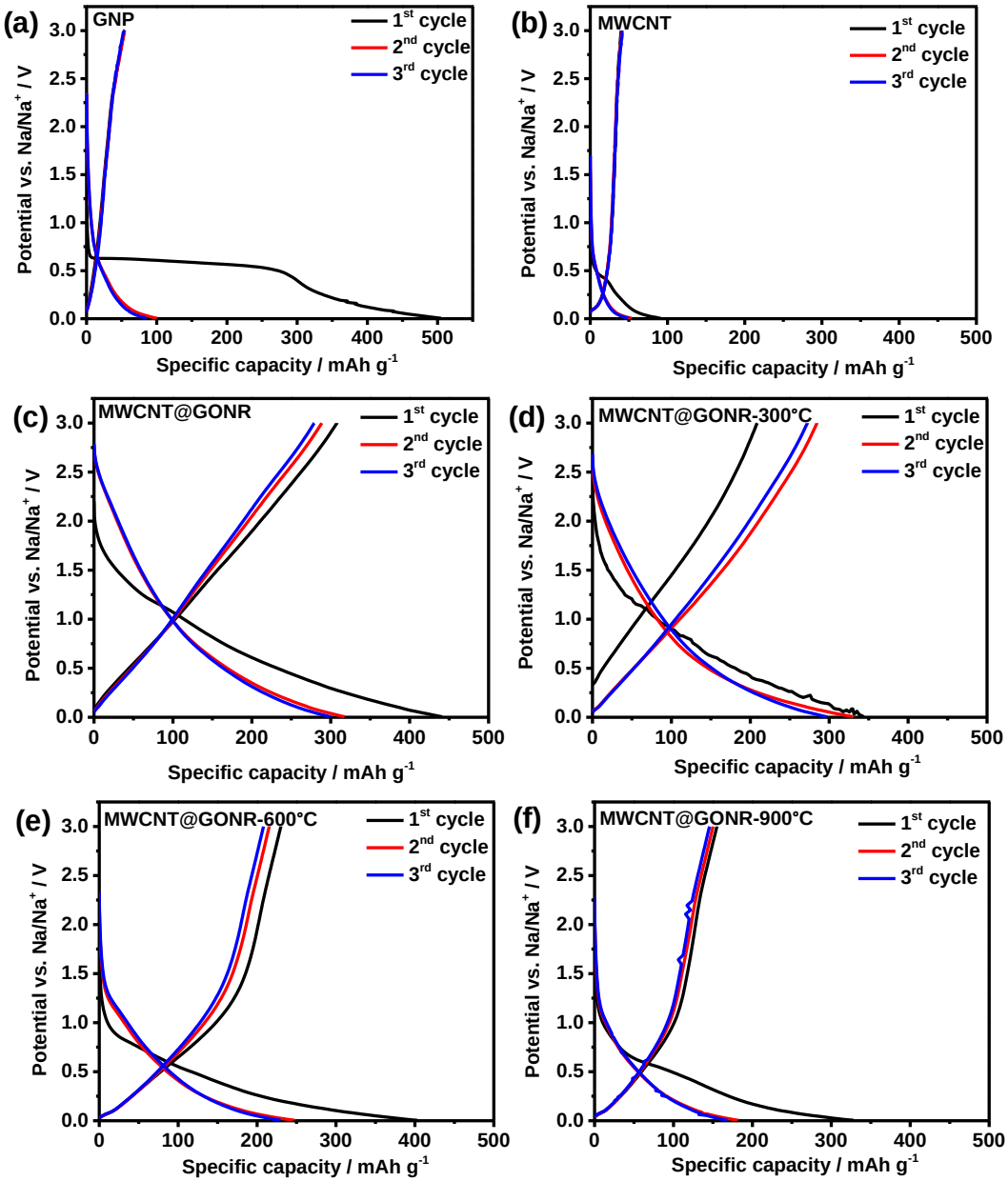

Figure 4.22 The galvanostatic charge-discharge curves at current density of 50 mA g^{-1} of (a) GNP, (b) MWCNT, (c) MWCNT@GONR, (d) MWCNT@GONR-300°C, (e) MWCNT@GONR-600°C, and (f) MWCNT@GONR-900°C in the potential range of 0.005 ~ 3 V vs. Na/Na^+. (Electrolyte: 1M $NaClO_4$ in EC:PC (1:1 weight %)). (Han-Yi Chen et al.: "A Multi-Walled Carbon Nanotube Core with Graphene Oxide Nanoribbon Shell as Anode Material for Sodium Ion Batteries". Adv. Mater. Interfaces 2016, 1600357. Copyright Wiley-VCH Verlag GmbH & Co. KGaA. Reproduced with permission.[137])

Figure 4.23 presents the cycling performance of GNP, MWCNT, MWCNT@GONR, MWCNT@GONR-300°C, MWCNT@GONR-600°C, and MWCNT@GONR-900°C at a current density of 50 mA h g^{-1}. Among those samples, MWCNT@GONR exhibits the largest reversible discharge capacity after the second cycle. The capacities decrease with the reducing amount of O-containing functional groups. It is worth noting that the capacities of MWCNT@GONR samples, with or without annealing process, exhibit significant improvement over MWCNT and GNP. A high capacity up to 317 mA h g^{-1} in the 2^{nd} cycle and ~ 200 mA h g^{-1} after 100 cycles with a coulombic efficiency of ~100 % can be achieved by MWCNT@GONR. The higher capacity of MWCNT@GONR than GNP indicates that it can be a potential carbon buffering matrix to substitute for graphene which is used to form carbon composites with alloy type or metal oxide/sulphide anode materials in order to increase the electrical connectivity and the surface area, as well as prevent the volume expansion. The lower capacity retention of MWCNT@GONR than MWCNT@GONR-900°C might be attributed to the present of O-containing functional groups on MWCNT@GONR that brings on some irreversible sodium adsorption onto the defect sites.[27]

Figure 4.24 shows the capacity at various current densities. The discharge capacities decay at higher current densities. The capacities (6^{th} cycle) of MWCNT, MWCNT@GONR, MWCNT@GONR-300°C, MWCNT@GONR-600°C, and MWCNT@GONR-900°C at a current density of 20 mA h g^{-1} are 64, 361, 320, 234, and 153 mA h g^{-1}, respectively. Higher capacity of MWCNT@GONR as compared to others even at higher current rate mainly contributed from the higher amount of functional groups and surface defects.[27] MWCNT@GONR performs a high capacity of 165 mA h g^{-1} even at

high current density of 2000 mA g^{-1}, exhibiting a high rate capability. At 37th cycle, the current rate changes back to 20 mA g^{-1}, and the capacities are rather stable up to 50th cycle.

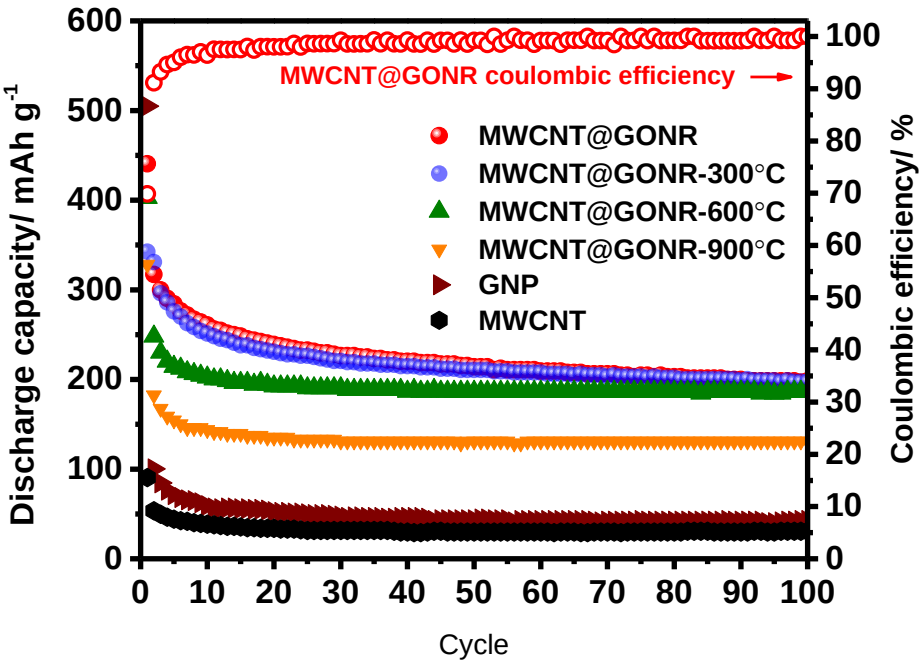

Figure 4.23 The cycling performance measured at current density of 50 mA g^{-1} of GNP, MWCNT, MWCNT@GONR, MWCNT@GONR-300°C, MWCNT@GONR-600°C, and MWCNT@GONR-900°C. (Electrolyte: 1M $NaClO_4$ in EC:PC (1:1 weight %)). (Han-Yi Chen et al.: "A Multi-Walled Carbon Nanotube Core with Graphene Oxide Nanoribbon Shell as Anode Material for Sodium Ion Batteries". Adv. Mater. Interfaces 2016, 1600357. Copyright Wiley-VCH Verlag GmbH & Co. KGaA. Reproduced with permission.[137])

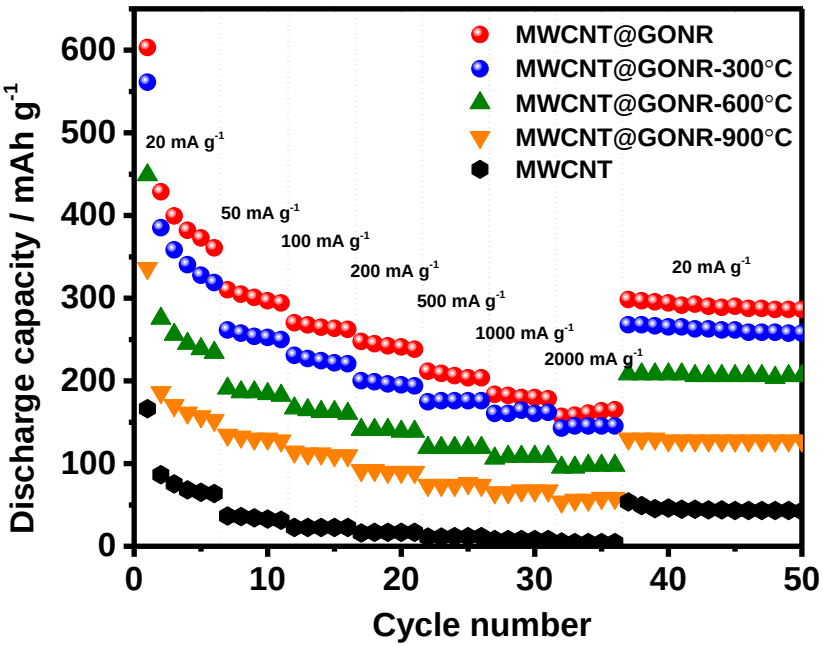

Figure 4.24 The rate capability and stability of GNP, MWCNT, MWCNT@GONR, MWCNT@GONR-300°C, MWCNT@GONR-600°C, and MWCNT@GONR-900°C measured at current density of 20, 50, 100, 200, 500, 1000, 2000, and 20 mA g^{-1}. (Electrolyte: 1M $NaClO_4$ in EC:PC (1:1 weight %)). (Han-Yi Chen et al.: "A Multi-Walled Carbon Nanotube Core with Graphene Oxide Nanoribbon Shell as Anode Material for Sodium Ion Batteries". Adv. Mater. Interfaces 2016, 1600357. Copyright Wiley-VCH Verlag GmbH & Co. KGaA. Reproduced with permission.[137])

4.3.3 MWCNT@GONR–based full cell

A proof of concept test was carried out by utilizing a MWCNT@GONR anode and a P2-Na_xMnO_2 cathode in order to demonstrate the potential application of MWCNT@GONR as anode in practical NIBs.[121] The GCD profile of the P2-Na_xMnO_2 cathode at a current density of 20 mA g^{-1} is shown in **Figure 4.25 (a),** which exhibits a reversible capacity of 192 mAh g^{-1}. **Figure 4.25 (b)** presents the GCD profiles of P2-Na_xMnO_2 half-cell in the 2nd charge cycle and MWCNT@GONR half-cell in the 5th

discharge cycle at a current density of 20 mA g^{-1}. The P2-Na_xMnO_2 half-cell was charged and discharged for 2 cycles and the MWCNT@GONR half-cell was charged and discharged for 5 cycles before fabricating the full cell in order to reduce the effect of SEI formation. The mass ratio of cathode and anode was calculated based on the equation $q_a = q_c$ $(C_a m_a = C_c m_c)$, where C is specific capacity, m is mass, a symbolizes anode, c symbolizes cathode.[20] The capacity of 344 mA h g^{-1} can be obtained in the potential range of 0.005 ~ 2.2 V vs. Na/Na^+ for MWCNT@GONR, and of 164 mA h g^{-1} can be obtained in the potential range of 2.2 ~ 3.8 V vs. Na/Na^+ for P2-Na_xMnO_2, calculated from the GCD curves in **Figure 4.25 (b)**. Based on these data, a mass ratio of MWCNT@GONR: P2-Na_xMnO_2 = 1 : 2.1 is selected in this study.

Figure 4.25 (c) and **(d)** display the battery performance of the MWCNT@GONR// P2-Na_xMnO_2 full cell in the voltage window of 0 V to 4 V. After charging to 4 V, the initial charge capacity of the full cell is up to 466 mA h g^{-1} which is calculated based on the mass of MWCNT@GONR. The discharge capacity at the 1st cycle is 183 mA h g^{-1} based on the mass of MWCNT@GONR with an average potential of 1.65 V. The side reactions from both electrodes might cause the irreversible capacity in the 1st cycle. After the 2nd cycle, the capacities are rather stable with a small amount of degradation. The capacity is 140 mA h g^{-1} based on the mass of MWCNT@GONR at the 20th cycle with a capacity retention of 77 % and a coulomb efficiency of 88 %. The energy density of the MWCNT@GONR//P2-Na_xMnO_2 full cell is 99 Wh kg^{-1} according to the total mass of the active materials on both electrodes. This value is higher than other NIB system with a similar cathode reported in literature, such as rGO/Sb_2S_3//$Na_{2/3}Ni_{1/3}Mn_{2/3}O_2$ NIB system which exhibited an energy density of 80 Wh kg^{-1}.[115] The above results indicate that MWCNT@GONR is a promising anode material for NIBs. Although a $LiFePO_4$//$Li_4Ti_5O_{12}$ LIB system has an higher energy

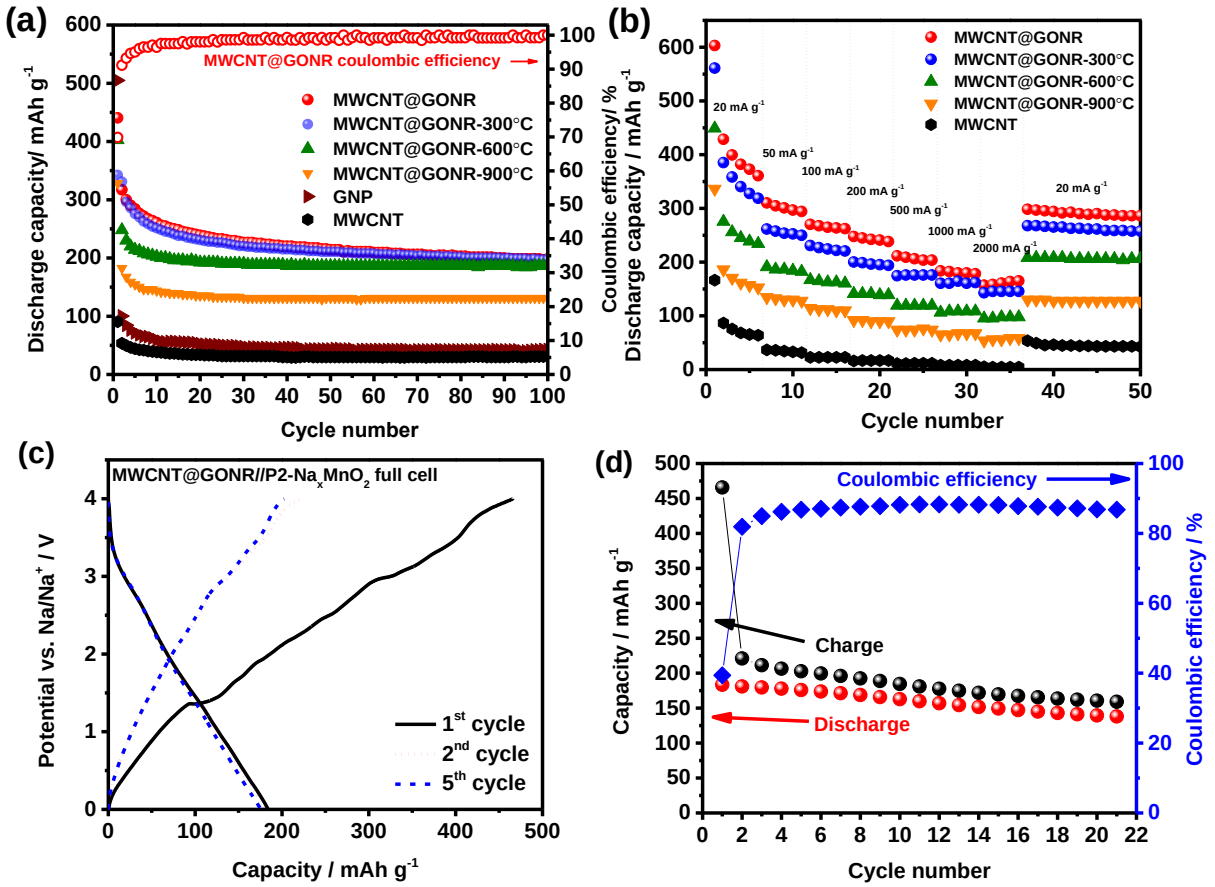

Figure 4.25 Proof of concept for a MWCNT@GONR–based full cell set-up using MWCNT@GONR as anode and P2-Na_xMnO_2 as cathode (Electrolyte: 1M $NaClO_4$ in EC:PC (1:1 weight %)). (a) The GCD curves of the P2-$Na_{0.7}MnO_2$ half-cell at current density of 20 mA g^{-1} in a potential range: 1.5 – 3.8 V vs. Na/Na^+. (b) The GCD curves of MWCNT@GONR half-cell at 5th discharging and P2-Na_xMnO_2 half-cell at 2nd charging at current density of 20 mA g^{-1}. (c) The full cell GCD curves and (d) the charge / discharge capacities with respect to the mass of MWCNT@GONR as well as the corresponding coulomb efficiencies at current density of 20 mA g^{-1} in a potential range: 0 – 4 V. (Han-Yi Chen et al.: "A Multi-Walled Carbon Nanotube Core with Graphene Oxide Nanoribbon Shell as Anode Material for Sodium Ion Batteries". Adv. Mater. Interfaces 2016, 1600357. Copyright Wiley-VCH Verlag GmbH & Co. KGaA. Reproduced with permission.[137])

density of 142 Wh kg^{-1} than our NIB system, [115] MWCNT@GONR//P2-Na_xMnO_2 NIB system can be improved by further optimization, such as optimizing the mass ratio or using other cathode materials with higher capacity.

4.3.4 Summary

In this section, a novel core–shell structure of MWCNT@GONR with carboxylic acid groups has been successfully synthesized by unzipping of MWCNTs using microwave energy, and has been studied as anode material for NIBs. The problem of restacking graphene sheets can be prevented by the unique core-shell structure of MWCNT@GONR which puts MWCNTs between GONR sheets thus enabling the electrolyte penetration. MWCNTs which have high electronic conductivity offer a direct electron transfer path while GONRs offer large surface area with carboxylic acid groups that enhance the adsorption of Na ions on the surface and enlarge the capacity. In order to investigate the impact of the carboxylic acid groups on the surface of MWCNT@GONR, the amount of those functional groups has been decreased successfully by employing annealing process at 300 ~ 900 °C, which is detected by FTIR, TGA, and XPS. At a current density of 50 mA h g^{-1} in the 2nd cycle, MWCNT@GONR with carboxylic acid groups exhibits significant higher capacities (317 mA h g^{-1}) than commercial MWCNT (54 mA h g^{-1}) and GNP (100 mA h g^{-1}). Capacity was reduced when the amount of carboxylic acid groups on MWCNT@GONR was decreased after annealing. A full cell with MWCNT@GONR as anode and P2-Na_xMnO_2 as cathode was fabricated in order to demonstrate an actual device application of MWCNT@GONR, and it presented a high energy density up to 99 Wh kg^{-1}.

Chapter 5 Discussions

According to the results obtained from Chapter 4, we have demonstrated that POMs ($Na_6[V_{10}O_{28}]$), nanostructured carbon/POM hybrid (**SWCNT-TBA-PV_2Mo_{10}**), and nanostructured carbon (MWCNT@GONR) are promising electrode materials for energy storage applications with their high capacitance and capacity.

POMs are proposed to provide high energy density due to their multi redox centers, and they can also offer high power density due to their large molecular size which might have low reorganization energy. Different redox centers (such as V and Mo) undergo different reactions during charging/discharging. POMs with different cation or functional groups (such as Na^+ and TBA-) present different stability in different electrolytes. $Na_6[V_{10}O_{28}]$ is more stable in organic electrolyte (1 M $LiClO_4$ in PC) which enable higher energy density due to the larger voltage window. On the other hand, **TBA-PV_2Mo_{10}** shows highly stability in aqueous electrolyte (1 M H_2SO_4) which exhibit long cycling life. In our high-power-density SC applications, both $Na_6[V_{10}O_{28}]$ and **SWCNT-TBA-PV_2Mo_{10}** electrodes exhibit higher energy density and higher power density than the common used carbon materials such as active carbon or SWCNT. For high-energy-density LIB applications, $Na_6[V_{10}O_{28}]$ cathode electrodes show higher capacity (> 200 mAh g^{-1} at ~ 0.1 C) than the commercial cathode materials such as $LiCoO_2$ (~ 137 mAh g^{-1}) and $LiFePO_4$ (~ 170 mAh g^{-1}). It even offer ~ 100 mAh g^{-1} at ~10 C which indicating the high power density behavior. For high-energy-density and low-cost NIB applications, an easily-synthesized and low-cost MWCNT@GONR anode with functional groups exhibits high capacity (> 300 mAh g^{-1}). Their unique core-shell structure also prevent the restacking problem of graphene sheets.

The aim of this chapter is to discuss the charge storage mechanisms of those POMs and nanostructured carbon electrode materials in order to realize the reason of their excellent performance. This chapter is divided into three sections. The first section discusses the charge

storage mechanisms of $Na_6[V_{10}O_{28}]$ electrodes which are used in SCs and LIBs. Pseudocapacitance contributions of $Na_6[V_{10}O_{28}]$ on the enhanced SC performance were studied using XPS. For the $Na_6[V_{10}O_{28}]$ electrode used in LIBs, we employ both XAFS spectroscopy and kinetic studies conducted by chronoamperometric experiments so as to obtain a complete understanding the electron transfer mechanism. The number of transferred electrons which is related to the energy density can be examined by XAFS, while the electron transfer rate k_0 extracted by kinetic studies is related to the power density. The second section will focus on the influence of the combination of POMs and nanostructured carbon materials by investigating the charge storage mechanism of **SWCNT-TBA-PV_2Mo_{10}** electrodes in SCs utilizing CV and scan rate analysis. The third section examines the impact of unique core-shell structure of MWCNT@GONR and the effect of functional groups of MWCNT@GONR on the NIB performance using various techniques including CV and scan rate analysis.

5.1 Charge Storage Mechanism of $Na_6[V_{10}O_{28}]$ electrode

5.1.1 XPS measurement of $Na_6[V_{10}O_{28}]$ SC electrode

X-ray photoelectron spectroscopy (XPS) was utilized in this study in order to further investigate the redox behaviour of $Na_6[V_{10}O_{28}]$ SC electrodes during charge–discharge process in 1 M $LiClO_4$ in PC. The XPS spectra of V $2p_{3/2}$ and Li 1s of $Na_6V_{10}O_{28}$ electrodes at 0.7 V vs. $Ag/AgNO_3$ (charged) and −1.3 V vs. $Ag/AgNO_3$ (discharged) are shown in **Figure 5.1**. In order to compare the concentration of V and Li, the background curves were corrected and normalized in the XPS spectra.

The change in the oxidation state of V was recorded and determined by the V $2p_{3/2}$ XPS spectra. In the literature, V^{5+} with a $2p_{3/2}$ binding energy of ~517.3 eV, and V^{4+} with a binding energy of ~516.2 eV can be found for $VO_x \cdot H_2O$.[146] Two peaks located at 517.1 eV

and 516 eV with peak splitting of 1.1 eV are observed in **Figure 5.1** indicating the partial reduction of V^{5+} to V^{4+} which are consistent with the literature.[146] After discharging from 0.7 V to −1.3 V the concentration of V^{4+} increases, which implies the redox reactions during the discharge process. The increased amount of V^{4+} is not significant because of the air contact which results in re-oxidation during electrode transportation to the ex-situ XPS instrument before measurement. **Figure 5.1** displays the XPS spectra of Li 1s, showing that the concentration of Li increases during discharge process. This can be explained that Li ions intercalate into or adsorb onto the $Na_6[V_{10}O_{28}]$ electrode.[147] The above findings which show the changing presence of Li and reduction of V^{5+} to V^{4+} demonstrate the Li ions intercalation and/or adsorption during the V reduction processes simultaneously.

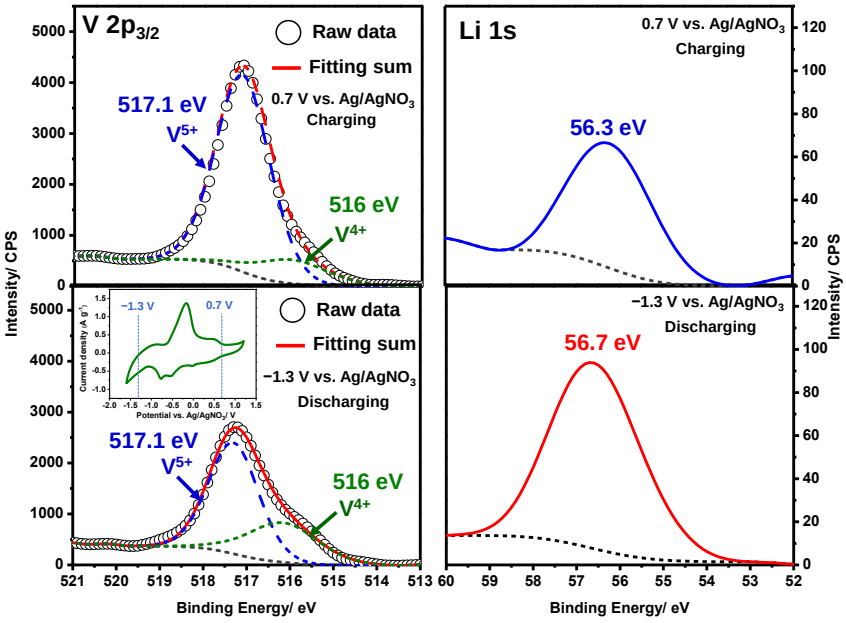

Figure 5.1 XPS spectra of (a) V $2p_{3/2}$ and Li 1s after the charge discharged cycle of $Na_6[V_{10}O_{28}]$ electrodes tested in 1 M $LiClO_4$ in PC. (Han-Yi Chen et al.: "A Polyoxovanadate as an Advanced Electrode Material for Supercapacitors". ChemPhysChem 2014, 15, 2162–2169. Copyright Wiley-VCH Verlag GmbH & Co. KGaA. Reproduced with permission.[20])

According to the results from XPS spectra, the charge storage mechanism of $Na_6[V_{10}O_{28}]$ electrodes in Li-containing organic electrolyte can be expressed as the following reaction which is dominated by the vanadium redox processes accompanied by lithium ion desorption/adsorption and/or insertion/extraction processes:

$$Na_6[V_{10}O_{28}] + \mathrm{n}Li^+ + \mathrm{n}e^- \leftrightarrow Li_\mathrm{n}Na_6[V^{5+}_{10-\mathrm{n}}V^{4+}_\mathrm{n}O_{28}] \quad (5.1)$$

Figure 5.2 illustrates partial reduction of V^{5+} to V^{4+} with intercalating and/or adsorbing Li ions during discharge process based on the above reaction which offers high faradic pseudocapacitance (357 F g^{-1} at a current density of 0.1 A g^{-1}). This study of charge transfer mechanism of $Na_6[V_{10}O_{28}]$ in Li-ion-containing electrolyte is presented in the first time. Nevertheless, the exact number of transferred electrons during the reaction cannot be determined here because of the limitations of ex-situ XPS measurement which might result in re-oxidation owing to air contact during electrode transportation. Thus, the next section will apply In-situ X-ray Absorption Fine Structure technique to determine the exact number of the electron transfer during the redox reaction of $Na_6[V_{10}O_{28}]$ electrode in LIB configuration.

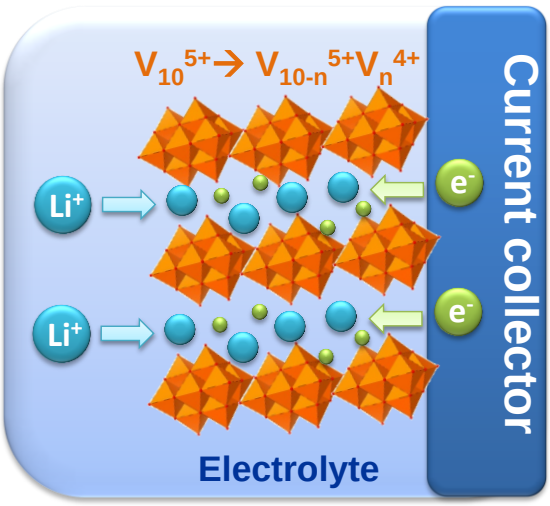

Figure 5.2 A schematic diagram showing the Li ion intercalation and/or adsorption process in $Na_6[V_{10}O_{28}]$ electrodes. (Han-Yi Chen et al.: "A Polyoxovanadate as an Advanced Electrode

Material for Supercapacitors". ChemPhysChem 2014, 15, 2162–2169. Copyright Wiley-VCH Verlag GmbH & Co. KGaA. Reproduced with permission.[20])

5.1.2 In-situ XAS measurement and Kinetic studies of $Na_6[V_{10}O_{28}]$ LIB Electrode

In this study, we combine both XAFS spectroscopy and kinetic studies conducted by chronoamperometric experiments in order to obtain a complete understanding the electron transfer mechanism of $Na_6[V_{10}O_{28}]$ electrode used in LIBs. These studies are relevant for practical applications of $Na_6[V_{10}O_{28}]$ as electrode material for energy storages. XAFS provides the information of electron transfer number which is related to the energy density; the electron transfer rate k_0 which can be obtained by kinetic studies is related to the power density.

5.1.2.1 In-situ XAS analyses of $Na_6[V_{10}O_{28}]$ electrode in LIBs

V K-Edges XANES

The V K-edge XANES spectra which were recorded at different potential vs. Li/Li^+ from the first discharge to the second charge cycle are displayed in **Figure 5.3**. The XANES spectra were normalized to an edge step in the energy region. Those spectra show highly reversible processes during charge/discharge at different potentials.

Figure 5.4 presents the XANES spectra for the first discharge/charge cycle and those of V_2O_5 (5+) and VO_2 (4+) as references. The energy of the absorption curves shift to a lower energy during the discharge process, implying that the V^{5+} is reduced to V^{4+}. When charged to 4 V vs. Li/Li^+, the energy of the absorption curves shifts to higher energy indicating the V^{4+} is oxidized to V^{5+}.

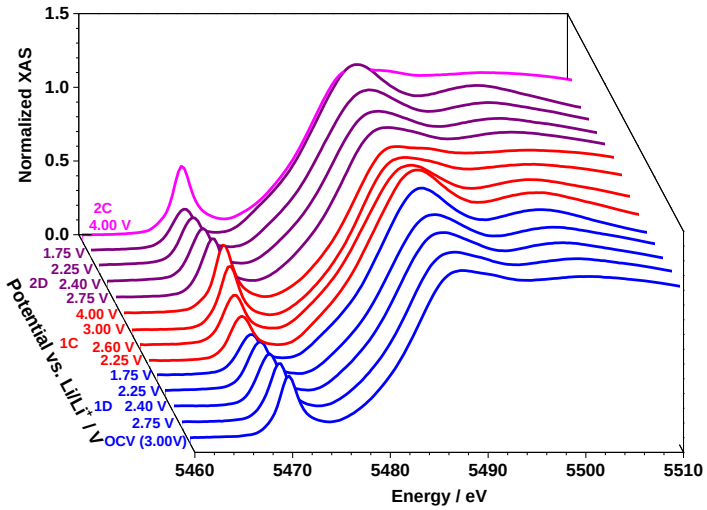

Figure 5.3 Normalized in-situ V K-edge XANES spectra for first discharging (1D, green), first charging (1C, orange), second discharging (2D, blue), and second charging (2C, pink) of $Na_6[V_{10}O_{28}]$ cathode. (Reproduced from my published paper by permission of PCCP Owner Societies. http://pubs.rsc.org/en/content/articlelanding/2017/cp/c6cp05768c.[126])

The valence of vanadium at each potential can be identified by calculating V K-edge XANES absorption edge energies. The linear relationship between the V oxidation state and the X-ray absorption edge energy for the reference materials, V_2O_5 (5+) and VO_2 (4+), was utilized to calculate the average valence of the V ions in $Na_6[V_{10}O_{28}]$. The results are plotted as a function of the battery potential as shown in **Figure 5.5**. The oxidation state of the 10 vanadium ions in $Na_6[V_{10}O_{28}]$ electrode is V^{5+} before any electrochemical testing. Nevertheless, the initial average valence of the V is ca. 4.8 before the first discharge (at open circuit voltage, ca. 3 V), which might be because of self-discharging in the beginning. The average valence of vanadium decreases to around 4.0 during the first discharge cycle, and increases to around 5.0 after the first charge cycle. The second discharge and second charge cycle repeat the same behavior of the first cycle. It is worth noting that the energy shifts during the first two charging/discharging cycles correspond to each other indicating a totally reversible process. The average valence of vanadium changed from

5.0 to 4.0 during the discharging processes implying that all 10 V^{5+} ions in $Na_6[V_{10}O_{28}]$ are reduced to V^{4+}. This result demonstrates that ten additional electrons can be stored in one $[V_{10}O_{28}]^{6-}$ molecule.

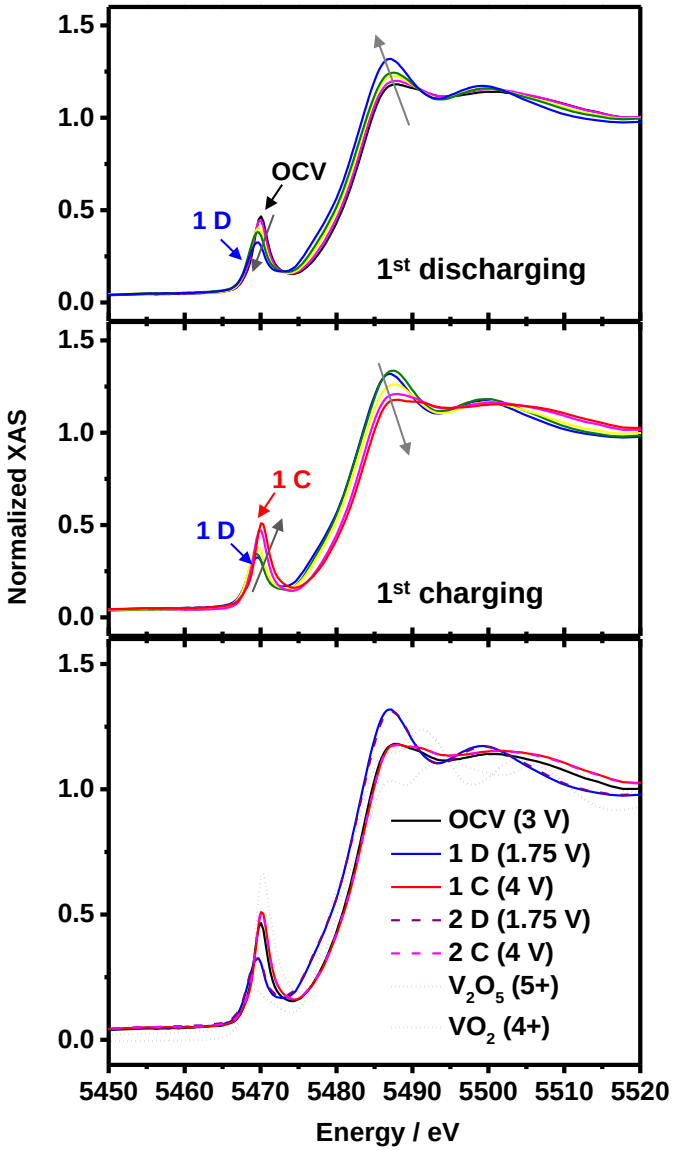

Figure 5.4 V K-edge XANES spectra for $Na_6[V_{10}O_{28}]$ LIBs in the first discharging, second charging, and the first two cycles compared with V_2O_5 and VO_2 reference material. (Reproduced from my published paper by permission of PCCP Owner Societies. http://pubs.rsc.org/en/content/articlelanding/2017/cp/c6cp05768c.[126])

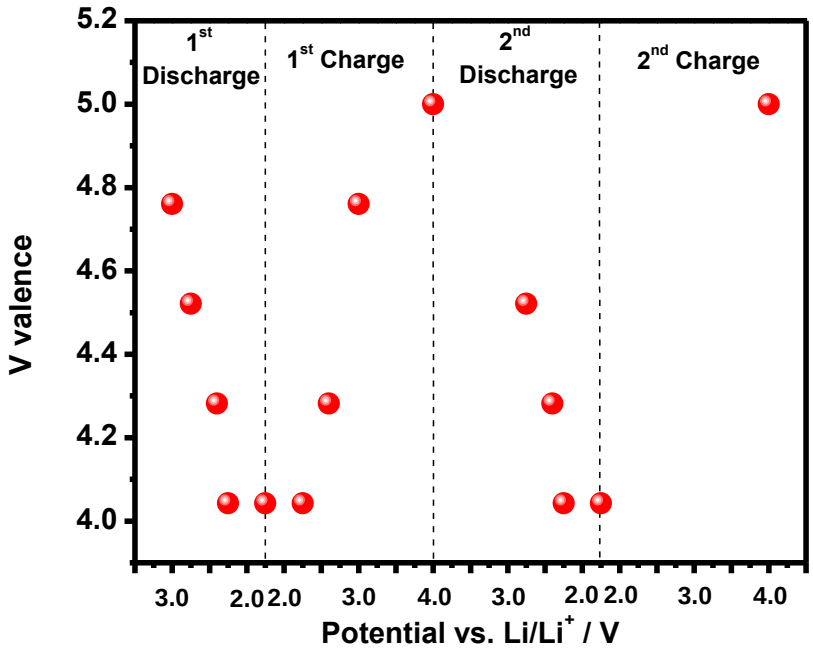

Figure 5.5 Mean V valence of $Na_6[V_{10}O_{28}]$ cathode as a function of the cell voltage (V). (Reproduced from my published paper by permission of PCCP Owner Societies. http://pubs.rsc.org/en/content/articlelanding/2017/cp/c6cp05768c.[126])

The CV curves of the $Na_6[V_{10}O_{28}]$ LIB at different scan rates varying from 0.1 to 2 mV s^{-1} are shown in **Figure 5.6 (a)**. **Figure 5.6 (b)** illustrates the relation between peak currents (I_p) and square root of scan rate ($\nu^{0.5}$) which generates two straight lines indicating the redox-processes are diffusion controlled ($I_p \propto \nu^{0.5}$) [21,61,148,149] where the involved freely diffusing species is lithium ion. The charge storage mechanism of $Na_6[V_{10}O_{28}]$ cathode in LIB according to the results from V K-edge XANES absorption edge energies is dominated by the redox processes of vanadium accompanied by insertion/extraction of lithium ion. This reaction can be summarized by the following expression:

$$Na_6[V_{10}^{5+}O_{28}] + 10Li^+ + 10e^- \leftrightarrow Li_{10}Na_6[V_{10}^{4+}O_{28}] \quad \textbf{(5.2)}$$

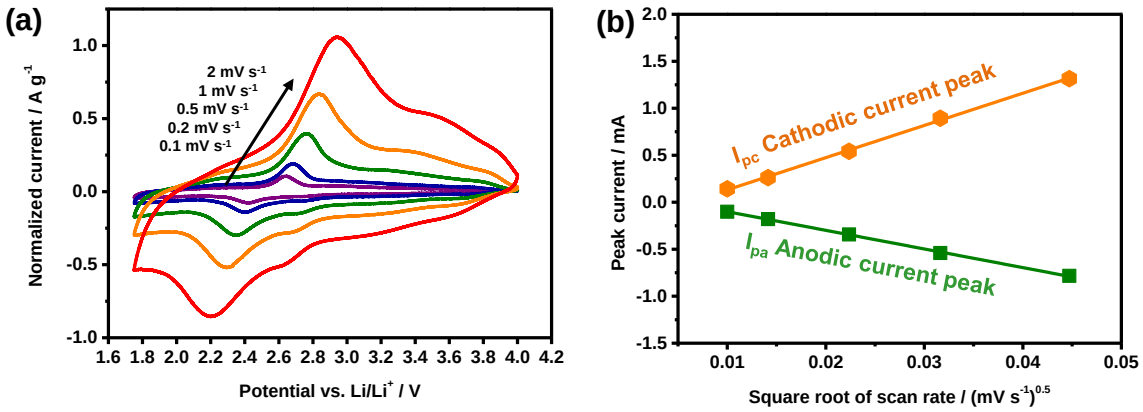

Figure 5.6 (a) Cyclic voltammograms of $Na_6[V_{10}O_{28}]$ electrodes in 1 M $LiPF_6$/EC:DEC (1:1) in a half-cell configuration with Li metal as counter electrode and reference electrode at 0.1, 0.2, 0.5, 1, 2 mV s^{-1}. (b) Peak current vs. square root of scan rate for the main redox peaks in (a). (Reproduced from my published paper by permission of PCCP Owner Societies. http://pubs.rsc.org/en/content/articlelanding/2017/cp/c6cp05768c.[126])

According to the above results, the theoretical capacity of $Na_6[V_{10}O_{28}]$ can be calculated as 245 mAh g^{-1} with ten transferred electrons. This value is much higher than other common LIB cathode materials such as $LiCoO_2$ (137 mAh g^{-1}) or $LiFePO_4$ (170 mAh g^{-1}).[150] Nevertheless, the measured capacity of ~ 220 mAh g^{-1} is lower than the theoretical capacity of 245 mAh g^{-1}, which might be caused by side reactions. Despite the high capacity, the relatively low redox potential of 2.55 V vs. Li/Li^+ is lower than current commercial cathode materials and this might limit it's potential in future high energy applications.[151]

In-situ EXAFS Analyses of $Na_6[V_{10}O_{28}]$ Electrodes

In-situ EXAFS analyses were utilized to detect the local environment and the molecular structural information of vanadium atoms in $Na_6[V_{10}O_{28}]$ during charging/discharging processes. The k^3-weighted Fourier transform (FT) magnitude spectra which present the radial atomic

distribution around vanadium atoms in $Na_6[V_{10}O_{28}]$ are displayed in **Figure 5.7 (a)** and **(b)**. The detected states-of-charge are represented in the spectra as: OCV (open circuit voltage), 1D (1st discharging), 1C (1st charging), 2D (2nd discharging), and 2C (2nd charging). The spectrum shows five main peaks at around 1.2, 1.6, 2.1, 2.7, and 3.3 Å at OCV.[22] The peaks located at around 1.2 and 1.6 Å represent a V=O double bond and a V−O−V single bond, respectively. Those peaks are assigned to the V−O local geometry of the first coordination sphere. The peaks which are contributed from V−V second coordination sphere can be found at around 2.1, 2.7, and 3.3 Å.[22,152] After the first discharge (from OCV to 1D), the spectrum changes: the intensity becomes smaller at the 1.2 Å peak, and the intensity of the 1.6 Å peak is significantly reduced. The intensity of the 1.6 Å peak decreases after the first charging (1C), while the peak at 1.2 Å is seen to increase. The 2D and 1D spectrums are similar and the spectrum of 2C overlaps with the 1C, indicating highly reversible structural changes of the $[V_{10}O_{28}]^{6-}$ molecule during charging/discharging processes. The intensity of V=O (~1.2 Å) reduces during discharging process implying the double bonds become single bonds, while the Li ions adsorb on the terminal O atoms. During the discharging process, the intensity of V−O−V (~1.6 Å) increases showing higher symmetrical structure of V^{4+} than V^{5+}.[152] The intensity of V−V bonds decreases after 1st discharge and remain stable in the following cycles, indicating some of the crystal structure becomes amorphous as shown in **Figure 5.8**. These results correspond to the observation in literature which studied a V-based POM, $K_7[NiV_{13}O_{38}]$, as cathode in LIBs and showed amorphization after 1st discharge and became stable in the following cycles.[3]

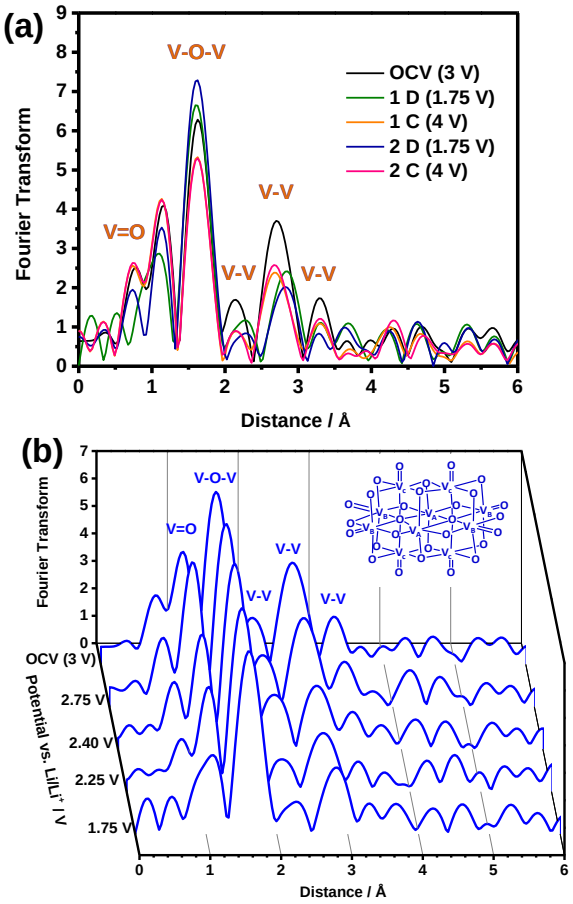

Figure 5.7 (a) The experimental Fourier transforms of the V K-edge EXAFS spectra for OCV, 1D, 1C, 2D, and 2C. (b) Evolution of the Fourier transforms of the V K-edge EXAFS spectra in the first discharging.

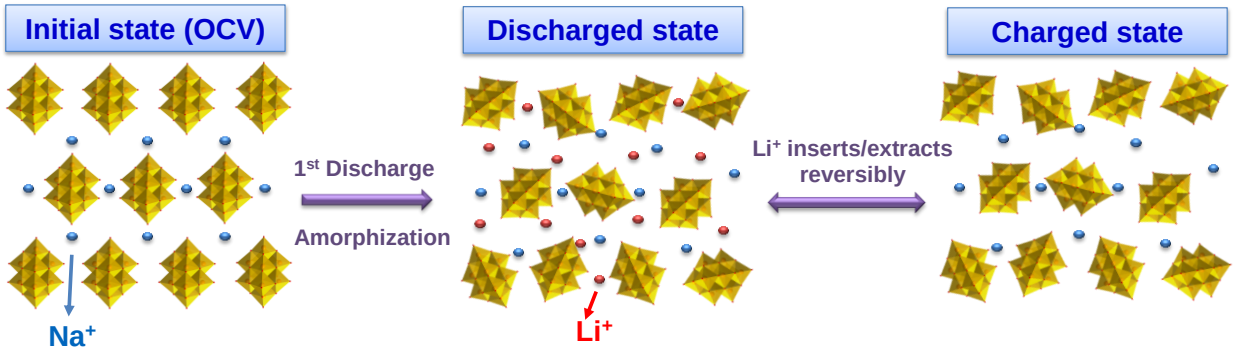

Figure 5.8 Schematic illustration of the discharge–charge reaction mechanism for $Na_6[V_{10}O_{28}]$ cathode.

5.1.2.2 Kinetic studies of $Na_6[V_{10}O_{28}]$ electrode in LIBs

In this study, chronoamperometric experiments are utilized to record the transient currents at temperatures varying from -10 ˚C to 50 ˚C in order to calculate the electron transfer rates and reorganization energy of $Na_6[V_{10}O_{28}]$ porous electrodes in LIBs.

The first principles can be utilized to predict the reorganization energy, λ in a liquid-solid interface. The reorganization energy represents the energy required to change the nuclear configurations from the reactant and the solvent states to the product state.[153] The total reorganization energy for electron transfer includes the outer reorganization of the solvent λ_o, resulting from long-range electrostatic forces, and the inner relaxation of the reactant λ_i, resulting from short range bond forces.[85] The POM framework shelters the electrostatic interaction between polar solvent and redox-center, thus the outer sphere reorganization λ_o energy of POMs is supposed to be small.[87] The outer sphere reorganization λ_o can be evaluated based on the Born energy of solvation:[85]

$$\boldsymbol{\lambda_o = \frac{e^2}{8\pi\varepsilon_0 k_B T}\left(\frac{1}{a_0} - \frac{1}{2d}\right)\left(\frac{1}{\varepsilon_{op}} - \frac{1}{\varepsilon_s}\right)} \qquad \textbf{(5.3)}$$

where ε_0 is the permittivity of free space, a_0 is the effective radius of the reactant, d is the distance from the center of the reactant to the surface of the electrode, ε_{op} is the optical dielectric constant and ε_s is the static dielectric constant. Generally, λ_o represents a major part of the entire reorganization energy λ. The average radius of $[V_{10}O_{28}]^{6-}$ is a_0 =0.7 nm and we assume $[V_{10}O_{28}]^{6-}$ is contact with the electrode directly. Hence d = a_0 = 0.7 nm, and the outer reorganization energy of 98 meV is estimated. As compared to a commonly used LIB cathode, $LiFePO_4$ (213 meV, *FeO_6 octahedrons, $d=a_0=0.21$ nm*), the outer reorganization energy of $Na_6[V_{10}O_{28}]$ is much smaller.[85] In order to prove this assumption that $Na_6[V_{10}O_{28}]$ has low reorganization energy, we determine λ

experimentally by conducting potential-step chronoamperometry experiments for $Na_6[V_{10}O_{28}]$ LIB at temperatures varying from -10 ˚C to 50 ˚C.

As mentioned in section 2.2.4, the redox dynamics of a $Na_6[V_{10}O_{28}]$ porous electrode can be modeled as a simple three-state Markov chain as shown in **Figure 5.9**.[85,86] In this model, $Na_6[V_{10}O_{28}]$ porous electrode is composed of $Na_6[V_{10}^{5+}O_{28}]$ particles, active particles (phase-transforming, partially inserted by Li ions but not fully filled), and $Li_{10}Na_6[V_{10}^{4+}O_{28}]$ particles (fully filled with Li ions). The activation rate of transforming each $Na_6[V_{10}^{5+}O_{28}]$ particle into an activate particle is represented by k_A. The reaction rate at the surface of activate particles which intercalate/de-intercalate lithium ions continuously during redox process is represented by k.[85,86]

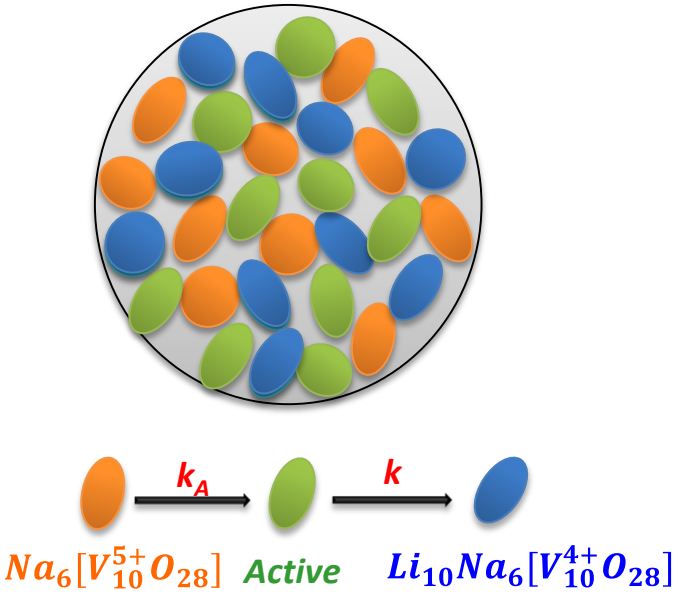

Figure 5.9 Schematic process in a porous electrode consisting of $Na_6[V_{10}^{5+}O_{28}]$ particles which will transform to active particles with an activation rate of k_A, active (transforming) particles, and $Li_{10}Na_6[V_{10}^{4+}O_{28}]$ particle which are transformed from an active particle with a reaction rate of k.

Bai and Tian have proposed a statistical model to identify discrete-particle phase transformations in porous electrode as shown in equation (2.8).[85,86] Here we modify the equation

by adding the contribution from non-faradaic currents that charge the double layer: $I_0 e^{-t/\tau}$. The modified transient current in response to a potential step is shown in the following equation:[85]

$$I = kQ\left[\frac{N_0 k+(N_1-1)k_A}{k-k_A}e^{-kt} + \frac{(1-N_0-N_1)k_A}{k-k_A}e^{-k_A t}\right] + I_0 e^{-t/\tau} \quad (5.4)$$

where Q is the capacity, N_0 is the initial fraction of reacting particles in the electrode. N_1 is the initial fraction of inactive particles in the electrode, which is set to zero in this work.[85] τ is the time constant and I_0 is the current at t=0 s .

Chronoamperometry experiments were utilized to record the current transient in order to calculate the electron transfer rates and reorganization energy of $Na_6[V_{10}O_{28}]$ electrodes. Before each negative over potential step, $Na_6[V_{10}O_{28}]$ LIBs were charged to and held at 4.0 V vs. Li/Li^+ for 4 h, while they were discharged to and held at 2.0 V vs. Li/Li^+ for 4 h before each positive over potential step, so that the initial states before each step were kept the same. The size of the potential step was determined according to the formal potential (e.g. 2.55 V vs. Li^+/Li at 25 °C) which is temperature dependent and was calculated as the average of the main peak potentials from CVs. Equation 5.4 was utilized to fit the current transients in order to obtain the k values at different over potentials. **Figure 5.10 (a)** illustrates two transient currents as examples at a potential step of $\pm$125 mV at 25 °C. The transient current of the charging step (125 mV) is fitted with the parameters: k = 0.094 s^{-1}, k_A = 0.010 s^{-1}, Q = 0.292 A s, N_0 = 0.2, and I_0 = 5.9 mA, where the measured capacity is Q_{ex}= 0.286 A s. The transient current of the discharging step (125 mV) is fitted with the parameters: k = 0.09 s^{-1}, k_A = 0.012 s^{-1}, Q = 0.292 A s, N_0 = 0.41, and I_0 = 94 mA, where the measured capacity is Q_{ex} =0.288 A s. In our results, the value of k is larger than k_A which indicates the increase of active particles is slower and the population is relatively stable after long period of time.[154] This might due to the amorphous structure of $Na_6[V_{10}O_{28}]$ after initial discharge as observed from EXAFS results. The amorphous structure which lack of free channels slows down the speed of starting Li ions intercalation results in smaller k_A as compared to k. After

starting to fill the Li ions in to the structure, the speed becomes faster because of the low reorganization energy (POM framework shelters the electrostatic interaction between polar solvent and redox-center) which leads to larger k as compared to k_A.

Figure 5.10 (b) illustrates the Tafel plots of the reaction rates k determined from chronoamperometric experiments using equation (5.4). In the Tafel plots, $\eta = e(E - E^{0'})/k_B T$ is the dimensionless overpotential where e represents the elementary charge, k_B represents Boltzmann constant, and T represents the absolute temperature. The Butler-Volmer **(**BV) model is utilized to illustrate the linear Tafel plot which is represented as the dotted curves with α = 0.5. By extrapolating the linear fit plots to zero overpotential (η =0), the electron transfer constant k_0 can be determined.[155] However, this k_0 value is related to the ten electrons transfer in the whole $Na_6[V_{10}O_{28}]$ molecule as detected by XANES.

The kinetic rate constant k_0' for a single electron in $Na_6[V_{10}O_{28}]$ is calculated by dividing k_0 by 10 (the number of transferred electrons). The k_0' value is ~ 6.0×10^{-3} s^{-1} for $Na_6[V_{10}O_{28}]$ which is roughly thirty times larger than the k_0' value for $LiFePO_4$ ($k_0'^{,LiFePO4}$=2.0 x 10^{-4} s^{-1}) as reported in literature.[85]

Chronoamperometric experiments at different temperatures (-10, 10, 25, and 50 °C) were employed to determine the reorganization energy of $Na_6[V_{10}O_{28}]$. **Figure 5.10 (c)** displays the reaction rates extracted from experiments at -10, 10, 25, and 50 °C. The effective energy barrier, G_a, can be obtained based on the Arrhenius temperature dependence:

$$\ln k_0 = \ln A - \frac{G_a}{k_B T} \qquad (5.5)$$

where A represents the Arrhenius constant. **Figure 5.10 (d)** illustrates the Arrhenius plots of the rate constants under -10, 10, 25, and 50 °C. Based on the equation (5.5), the effective energy barrier, G_a, of $Na_6[V_{10}O_{28}]$ can be calculated as 49 meV, which is roughly 2.5 times smaller than for

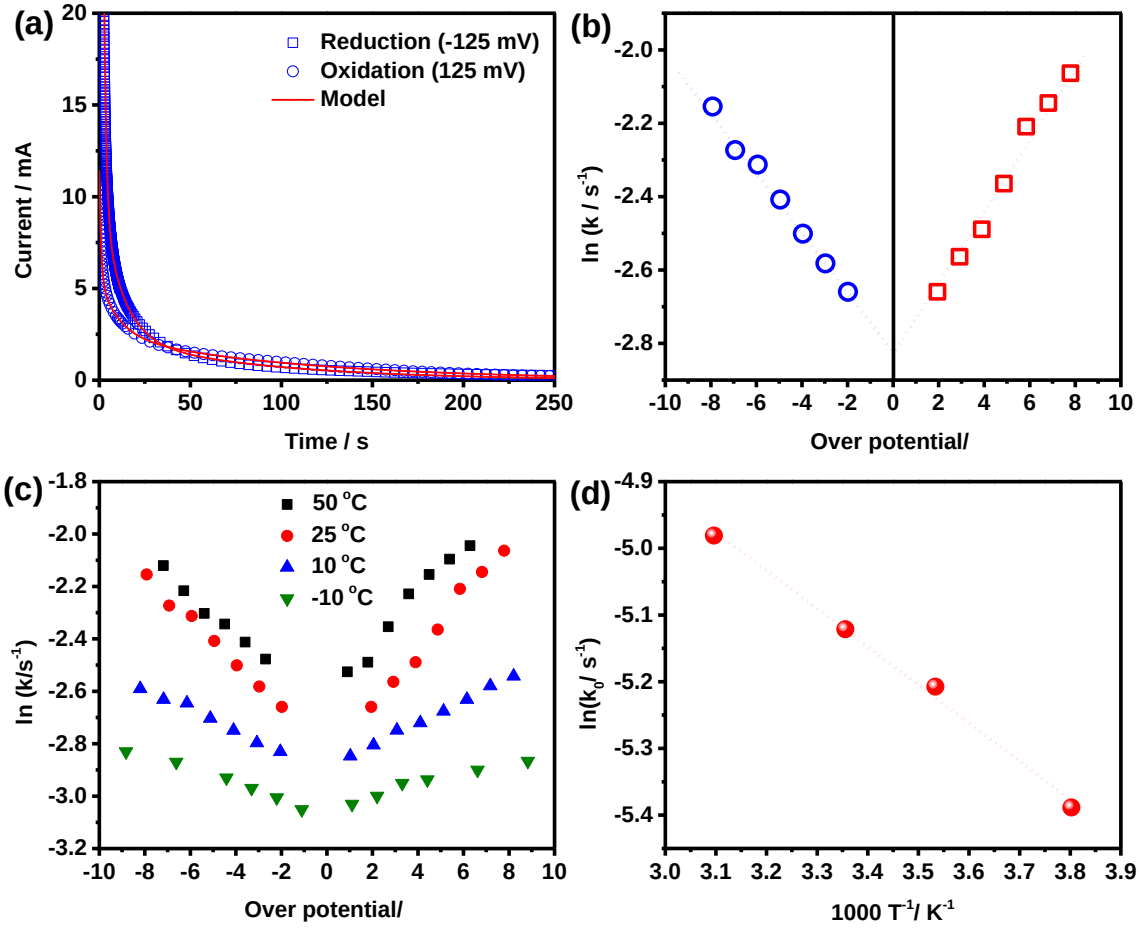

Figure 5.10 (a) Examples of the transient currents with fitting curves under 25 °C. (b) Tafel plots of the reaction rates extracted by the transient current equation from chronoamperometry experiments of $Na_6[V_{10}O_{28}]$ electrodes under 25 °C, where overpotential $\eta = e(E - E^{0'})/k_BT$. Dotted curves indicate the BV model (linear Tafel plot) with a = 0.5 (c) Tafel plots of the fundamental reaction rates under -10, 10, 25, and 50 °C. (d) Arrhenius plot of the rate constants k_0' under -10, 10, 25, and 50 °C. (Reproduced from my published paper by permission of PCCP Owner Societies. http://pubs.rsc.org/en/content/articlelanding/2017/cp/c6cp05768c.[126])

$LiFePO_4$ in the literature ($G_a^{LiFePO4}$ = 110 meV).[85] Base on the classical Marcus theory, the effective energy barrier is ~ λ/4:[85]

$$G_a = \frac{(\lambda + \Delta G^0)^2}{4\lambda} \approx \frac{\lambda}{4} \tag{5.6}$$

The reorganization energy of $Na_6[V_{10}O_{28}]$ electrode can be estimated as $\lambda = 197$ meV according to equation (5.6), which corresponds with our assumption for $\lambda_o = 98$ meV as $\lambda = \lambda_i + \lambda_o$. It shows that $\lambda_i \approx 99\ meV$ while λ_i and λ_o contribute almost equally to the reorganization energy. This result is reasonable because of the large size of the molecule with its highly coordinated redox-centers.

Those results from in-situ XAS and kinetic studies are summarized in **Figure 5.11**.

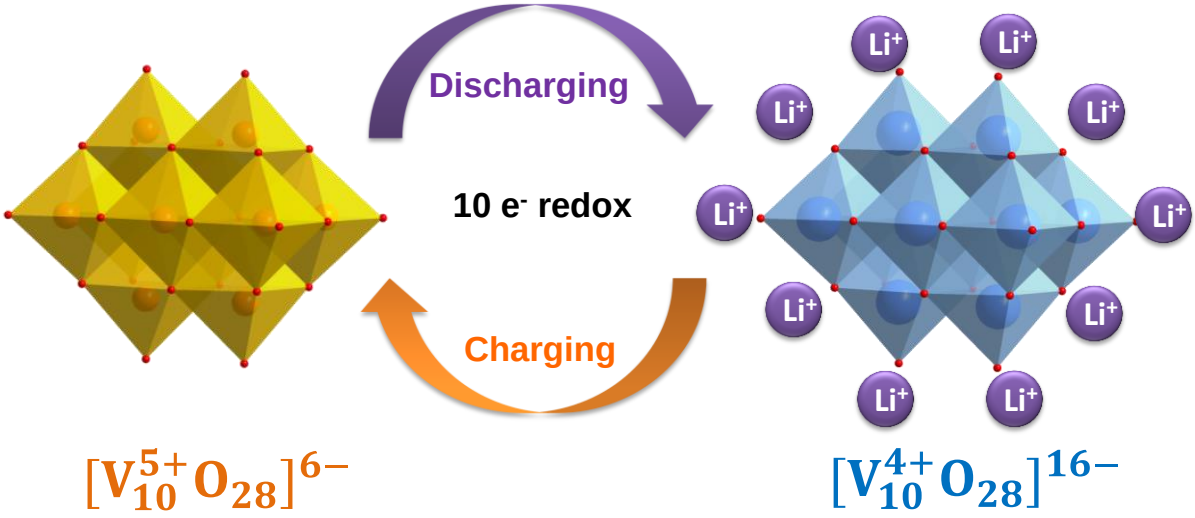

Figure 5.11 A model of redox reaction for $Na_6[V_{10}O_{28}]$ electrodes (Reproduced from my published paper by permission of PCCP Owner Societies. http://pubs.rsc.org/en/content/articlelanding/2017/cp/c6cp05768c. [126])

5.2 Charge Storage Mechanism of SWCNT-TBA-PV_2Mo_{10} Electrode in SCs

In this research, three-electrode CV was employed to investigate the electrochemical performance and pseudocapacitive behavior of **SWCNT-TBA-PV_2Mo_{10}** nanohybrid material as an electrode material for SCs. Ag/AgCl in 3.5 M KCl was utilized as the reference electrode and a Pt wire was used as the counter electrode. The CV curves of **TBA-PV_2Mo_{10}**, SWCNT, **SWCNT-TBA-PV_2Mo_{10}** and blank (polished glassy carbon with a diameter of 5 mm) electrodes tested from

−0.2 V to 1.0 V vs. Ag/AgCl at scan rates of 10 mV s^{-1} are illustrated in **Figure 5.11 (a)**. The current generated from the capacitance of the glassy carbon blank electrode is too small so that can be negligible. A rectangular double-layer capacitive behavior with a couple of broad redox peaks at the potential range of 0.3−0.5 V vs. Ag/AgCl is observed in the CV curve of the SWCNT electrode, indicating the faradic reactions generated from the carboxylic acid groups on the surface of SWCNTs.[63] The CV curve of the **TBA-PV_2Mo_{10}** electrode which deviates from the rectangular shape of an ideal capacitor exhibits faradaic behavior (pseudocapacitance).[156] The low electrical conductivity of the **TBA-PV_2Mo_{10}** electrode results in the broad and not well-defined redox peaks. The CV curve of the **SWCNT-TBA-PV_2Mo_{10}** electrode stems from the curve of SWCNT electrode with four extra well-defined redox peaks that are similar with the redox peaks in **TBA-PV_2Mo_{10}** electrode, showing a combination of double-layer capacitance mainly dominated from SWCNT and pseudocapacitance mainly dominated from **TBA-PV_2Mo_{10}**.[61] The main oxidation peaks at (i) 0.48 V, (ii) 0.37 V, (iii) 0.23 V, and (iv) −0.03 V vs. Ag/AgCl, and the corresponding reduction peaks located at (i') 0.45, (ii') 0.30 V, (iii') 0.20 V, and (iv') −0.06 V vs. Ag/AgCl can be observed. An intermediate reaction of (iii) is observed as a small oxidation peak (noted as *) at 0.1 V vs. Ag/AgCl. The irreversible reactions which are located at −0.15 and −0.2 V vs. Ag/AgCl (labeled with circles) will not be discussed here. The redox reactions of Mo atoms can be found in the redox couples of ii/ii', iii/iii', and iv/iv' which are two-electron reversible systems. A more positive potential than the other three reactions is observed at i/i' which might be the contribution from the redox reaction of V atoms and the faradic reactions generated from the carboxylic acid groups on the surface of SWCNTs. The electrochemical behavior of $[PV_2Mo_{10}O_{40}]^{5-}$ is similar to the previous studies reported by Barth and Bajwa et.al. [36, 37] The redox reactions of $[PV_2Mo_{10}O_{40}]^{5-}$ can be expressed by the following equations based on literature:[58,66,157]

$$[\boldsymbol{PV_2^V Mo_{10}^{VI} O_{40}}]^{5-} + (\boldsymbol{6+n})\boldsymbol{e^-} + (\boldsymbol{6+n})\boldsymbol{H^+} \leftrightarrow \boldsymbol{H_{6+n}}[\boldsymbol{PV_{2-n}^V V_n^{IV} Mo_6^{VI} Mo_4^V O_{40}}]^{5-} \qquad (5.7)$$

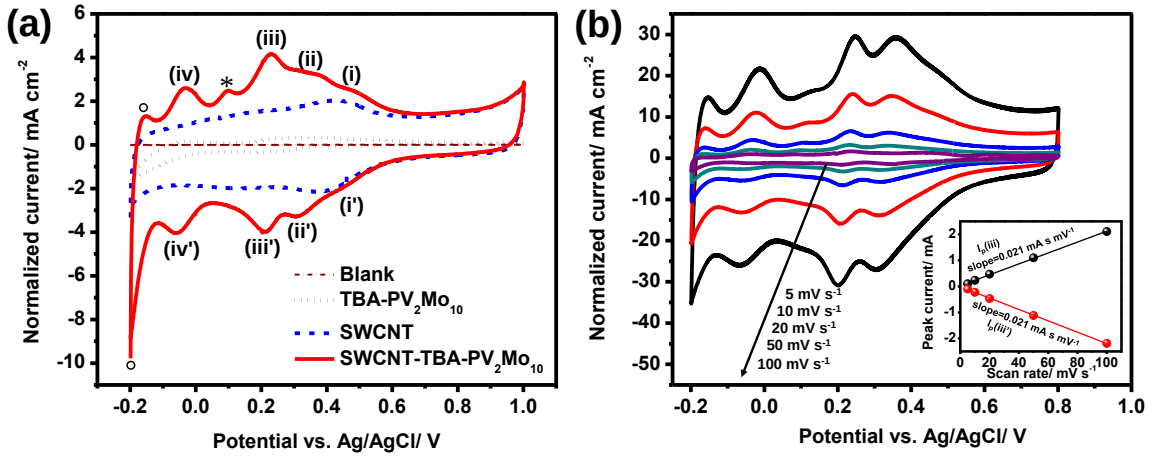

Figure 5.12 Cyclic voltammograms of (a) blank (glassy carbon), **TBA-PV$_2$Mo$_{10}$**, SWCNT, and **SWCNT-TBA-PV$_2$Mo$_{10}$** electrodes at 10 mV s^{-1}, and (b) **SWCNT-TBA-PV$_2$Mo$_{10}$** electrodes at 100, 50, 20, 10, 5 mV s^{-1} in 1 M H_2SO_4 in a three-electrode configuration with Pt wire as the counter electrode and Ag/AgCl as the reference electrode. Inset in (b) is peak current versus scan rate for the process (iii/iii′). (Reproduced from my published paper by permission of The Royal Society of Chemistry: http://pubs.rsc.org/en/content/articlelanding/2015/nr/c4nr07528e.[21])

Figure 5.12 (b) shows the CV curves of the SWCNT-TBA-PV$_2$Mo$_{10}$ electrode at different scan rates varying from 5 to 100 mV s^{-1}. The inset of **Figure 5.12 (b)** illustrates the relation between peak currents (I_p) and scan rates (ν) for process iii/iii′. Those data points produce two straight lines with the same absolute slope. The peak current is proportional to the scan rate which exhibits that the redox-processes are surface-processes rather than diffusion controlled ($I_p \propto \nu^{0.5}$).[61,148,149] The other three redox reactions also exhibit a similar behavior. The following equation can be utilized to express the relationship of peak current and scan rate:[61]

$$I_p = \frac{n^2 F^2 A \Gamma \nu}{4RT} \quad (5.8)$$

where n represents number of electrons, F represents Faraday's constant, A represents the surface area measured from BET (cm^2), Γ represents surface coverage (mol cm^{-2}), R represents ideal gas constant, and T represents temperature (K). Equation (5.8) cab be used to calculate the surface

coverage of SWCNT-TBA-PV_2Mo_{10} electrode: $\Gamma = 1.8 \times 10^{-11}$ mol cm^{-2}. The smaller surface coverage value of **SWCNT-TBA-PV_2Mo_{10}** electrode as compared to the maximum theoretical value (1.4×10^{-10} mol cm^{-2}), which assumes full coverage of Keggin-type POMs onto a flat accessible surface (ex. graphite),[61,158] indicating the pore accessibility is limited.

5.3 Charge Storage Mechanism of MWCNT@GONR electrode in NIBs

GNP, MWCNT, MWCNT@GONR, MWCNT@GONR-300°C, MWCNT@GONR-600°C, and MWCNT@GONR-900°C were tested as anode in a NIB half-cell configuration in order to understand their electrochemical properties. The half-cells were discharged in the beginning and cycled between 0.005 V and 3 V vs. Na^+/Na in the following cycles. The CV curves were recorded for all samples at a scan rate of 0.1 mV s^{-1} and the first three cycles are shown in **Figure 5.13**. In this first cycle of the CV curves, two main reduction peaks can be found. The reduction peak observed at ~ 0.45 V vs. Na^+/Na is attributed to the irreversible formation of solid-electrolyte interphase (SEI).[159] The adsorption of Na^+ onto the graphene sheets and/or active sites can be observed at the reduction peak of ~ 0.005 V.[4,160] One more reduction peak at ~ 1.4 V can be observed in MWCNT@GONR in the first cycle. It is contributed from the reactions of sodium with functional groups at the carbon surface.[161] The peaks in the oxidation curves at ~ 0.085 V vs. Na^+/Na for GNP, MWCNT@GONR, and MWCNT@GONR-300°C, and at ~ 0.010 V vs. Na^+/Na for MWCNT, MWCNT@GONR-600°C, and MWCNT@GONR-900°C, could be contributed from the desorption of Na^+ from the graphene layers.[160] **Figure 5.13 (a)** shows the CV curve of GNP which exhibits highly irreversible current in the initial cycle owing to the large amount of SEI layer in the high surface area. The current in the following cycles

decreases significantly which is owing to the restacking of the graphene sheets.[88] MWCNT@GONR presents much higher specific current and smaller irreversible current than GNP indicating that putting carbon nanotubes between graphene sheets can reduce the restacking effect in graphene and enhance the electrolyte penetration.[120] The enlarged surface area and significantly increased functional groups after the unzipping process result in the higher specific current of MWCNT@GONR as compared to MWCNT. As shown in **Figure 5.13 (c)-(f),** the CV curves of MWCNT@GONR with annealing at various temperatures (300, 600, and 900 °C) are performed in order to investigate the effect of O-containing functional groups on the electrochemical performance of MWCNT@GONR. The higher the annealing temperature the lower amount of O-containing functional groups on the sample is proved by FTIR, TGA-MS, and XPS. The specific currents reduce when the annealing temperature is increased in the potential range of 0.75 ~ 3 V vs. Na^+/Na, demonstrating that the redox reaction between sodium ions, and those functional groups on the surface of MWCNT@GONR offer more sites to store sodium ions.[27]

The charge storage mechanism of enhanced Na^+ storage capability of MWCNT@GONR is proposed here and illustrated in **Figure 5.15**. The enlarged surface area offers more spaces to attract Na ions after unzipping processes. Meanwhile, the highly active defects and functional groups on the surface of MWCNT@GONR can absorb a large amount of Na ions. Furthermore, the defects enable Na ions insert through the vacancies into the interlayers leading to more sites for the storage of Na ions.

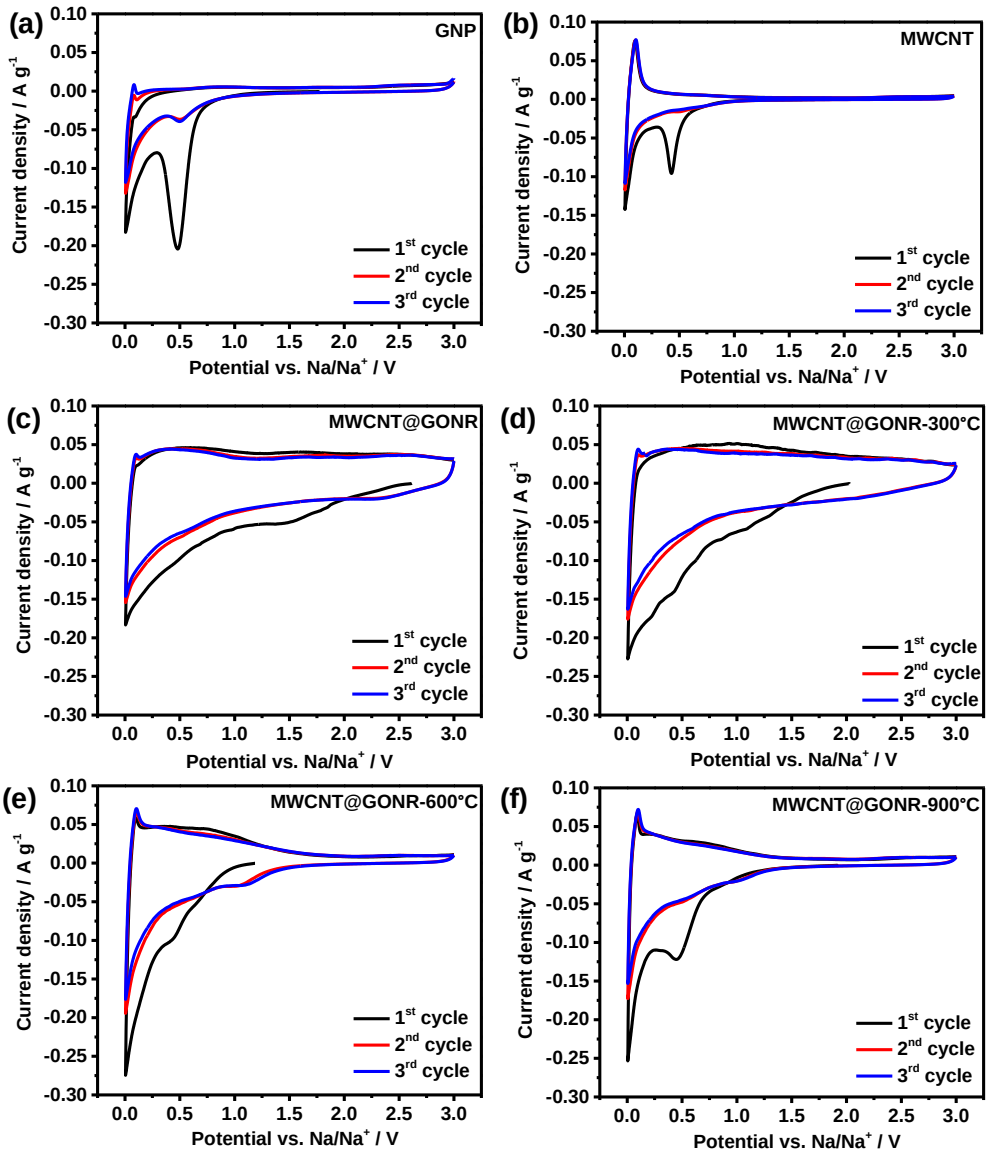

Figure 5.13 Cyclic voltammograms of (a) GNP, (b) MWCNT, (c) MWCNT@GONR, (d) MWCNT@GONR-300°C, (e) MWCNT@GONR-600°C, and (f) MWCNT@GONR-900°C measured at 0.1 mV s^{-1} in the potential range of 0.005 ~ 3 V vs. Na/Na^+ (Electrolyte: 1M $NaClO_4$ in EC:PC (1:1 weight %)). (Han-Yi Chen et al.: "A Multi-Walled Carbon Nanotube Core with Graphene Oxide Nanoribbon Shell as Anode Material for Sodium Ion Batteries". Adv. Mater. Interfaces 2016, 1600357. Copyright Wiley-VCH Verlag GmbH & Co. KGaA. Reproduced with permission.[137])

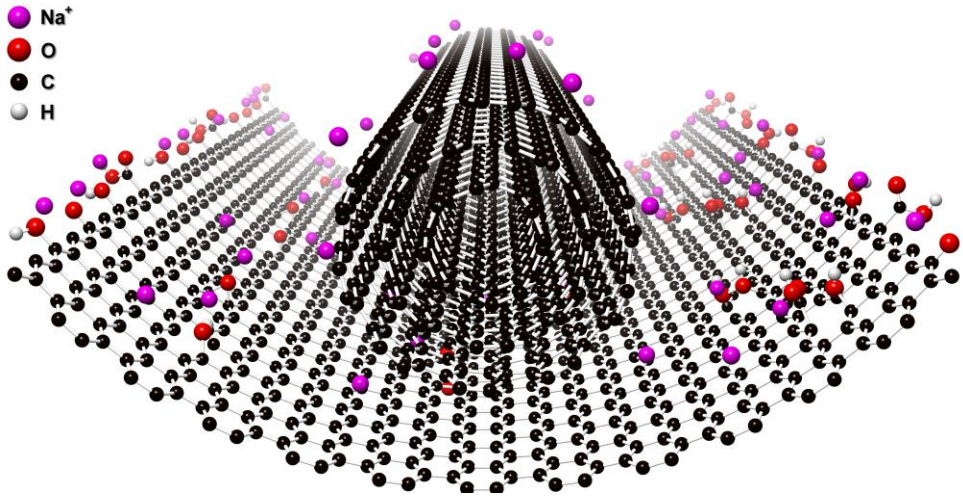

Figure 5.15 Schematic diagrams of insertion/adsorption of sodium ions into/onto MWCNT@GONR (Han-Yi Chen et al.: "A Multi-Walled Carbon Nanotube Core with Graphene Oxide Nanoribbon Shell as Anode Material for Sodium Ion Batteries". Adv. Mater. Interfaces 2016, 1600357. Copyright Wiley-VCH Verlag GmbH & Co. KGaA. Reproduced with permission.[137])

Chapter 6 Conclusions

Generally, in the electrochemical energy storages SCs provide high power density and long cycle life but limited energy density. In the other hand, LIBs and NIBs offer higher energy density but lower power density and cycling life as compared to SCs. Furthermore, NIBs has lower energy density but lower cost than LIBs, so it is promising for large-scale energy storage applications. The scientific novelty of this thesis is the realization of new electrode materials including polyoxometalates (POMs) and nanostructured carbon materials for SCs, LIBs, and NIBs in order to meet the demand for practical applications. This thesis also presents an in-depth investigation of the charge storage and charge transport mechanisms of POMs and nanostructured carbon materials utilized in those energy storage applications.

As we proposed, POM electrodes exhibit high energy density due to the multiple redox centers and high power density because of the low reorganization energy which enable fast charge transfer. In this thesis, $Na_6[V_{10}O_{28}]$ electrode presents a high specific capacitance of 354 F g^{-1} at 0.1 A g^{-1} in 1 M $LiClO_4$ in PC. Besides, the AC//$Na_6[V_{10}O_{28}]$ asymmetric SC provides a high power density of 6238 W kg^{-1} (with a corresponding energy density of 22 Wh kg^{-1}) and high energy density of 73 Wh kg^{-1} (with the power density of 312 W kg^{-1}), exhibiting the highest values of energy and power density among reported POM SCs so far. This high capacitance and energy density of $Na_6[V_{10}O_{28}]$ electrode is dominated by the vanadium redox processes ($V^{5+} \rightarrow V^{4+}$) accompanied by lithium ion desorption/adsorption and/or insertion/extraction processes based on the results from XPS measurements. The AC//$Na_6[V_{10}O_{28}]$ asymmetric SC is cycled up to 1000 cycles with a capacitance retention of ~ 70 %, showing moderate cycling stability. This might because of the less stability of POMs in organic electrolyte for long cycling time.

In order to achieve high cycling stability of POM SCs, **TBA-PV_2Mo_{10}** was selected in this work due to its insoluble nature in aqueous electrolyte and multiple redox reactions under acidic

solution. SWCNT was utilized to combine with **TBA-PV_2Mo_{10}** in order to increase the surface area and electronic conductivity. The **SWCNT-TBA-PV_2Mo_{10}** symmetric SC in 1 M H_2SO_4 electrolyte presents high specific capacitance of 444 F g^{-1}, high energy density of 15.4 Wh kg^{-1} with high maximum power density of 15.7 W kg^{-1}. The energy density and power density of **SWCNT-TBA-PV_2Mo_{10}** symmetric SC are higher than **SWCNT** symmetric SC is due to the pseudocapacitive behavior mainly contributed from **the redox reaction of TBA-PV_2Mo_{10}:** $[\boldsymbol{PV_2^V Mo_{10}^{VI} O_{40}}]^{\mathbf{5-}} + (\mathbf{6}+\boldsymbol{n})\boldsymbol{e^-} + (\mathbf{6}+\boldsymbol{n})\boldsymbol{H^+} \leftrightarrow \boldsymbol{H_{6+n}[PV_{2-n}^{V} V_n^{IV} Mo_6^{VI} Mo_4^{V} O_{40}]^{5-}}$. The redox-processes of **SWCNT-TBA-PV_2Mo_{10}** electrodes are surface-processes rather than diffusion controlled which has been determined by CV scan rate analyses. The surface-processes enable fast charging/discharging of SCs. The **SWCNT-TBA-PV_2Mo_{10}** symmetric SC also exhibits excellent cycling stability with capacitance retention of ~ 95 % up to 6500 cycles, which supports our statement that TBA functional groups enhance the stability of POM SCs in aqueous electrolyte.

For the study of POM electrodes in high-energy LIB applications, $Na_6[V_{10}O_{28}]$ was utilized and investigated as cathode material in this thesis. The electrodes exhibit high capacity of 213 mAh g^{-1} at 15 mA g^{-1} and high cycle stability up to 50 cycles with capacity retention of ~ 86 % at 150 mAh g^{-1}. In order to investigate the fundamental charge storage and transport mechanisms of $Na_6[V_{10}O_{28}]$ electrode in LIBs, in-situ XAFS measurements and chronoamperometric experiments were employed. In-situ V K-edge XAFS measurement revealed the oxidation states and inner structure changes of $Na_6[V_{10}O_{28}]$ molecule during charging/discharging. It was shown that the $[V_{10}O_{28}]^{6-}$ molecule undergoes a reversible 10 electron transfer with fully reduced/oxidized V^{5+}/V^{4+} ions in $Na_6[V_{10}O_{28}]$ during charging/discharging. Based on the results from in-situ XAFS measurements, a theoretical capacity of 245 mAh g^{-1} can be obtained for $Na_6[V_{10}O_{28}]$, which is higher than for typical LIB cathode materials such as $LiCoO_2$ (137 mAh g^{-1}) or $LiFePO_4$ (170 mAh g^{-1}). This result supports our statement that POMs provide multiple redox reactions which increase

the energy density. Furthermore, the kinetic rate and reorganization energy of $Na_6[V_{10}O_{28}]$ LIBs were also investigated by using chronoamperometric experiments. The obtained electron transfer kinetic rate of $Na_6[V_{10}O_{28}]$ ($k_0 = 5.9 \times 10^{-3}$ s^{-1}) is roughly 30 times faster than that of $LiFePO_4$ ($k_0 = 2.0 \times 10^{-4}$ s^{-1})[85], and the effective energy barrier of $Na_6[V_{10}O_{28}]$ is ~2.5 times smaller than for $LiFePO_4$ which leads to faster kinetics. This result correspond to our proposal that the higher molecular size, the lower reorganization energy and the faster kinetics (higher power density).

In order to develop high-energy and low-cost NIB, a novel core–shell structure of MWCNT@GONR with carboxylic acid groups has been synthesized by unzipping of MWCNTs using microwave energy, and has been studied as anode material for NIBs. At a current density of 50 mA h g^{-1} in the 2nd cycle, MWCNT@GONR with carboxylic acid groups reported in this thesis exhibits significant higher capacities (317 mA h g^{-1}) than commercial MWCNT (54 mA h g^{-1}) and GNP (100 mA h g^{-1}). This result indicates that the problem of restacking graphene sheets reported in the previous literatures can be prevented by this unique core-shell structure of MWCNT@GONR which puts MWCNTs between GONR sheets thus enabling the electrolyte penetration. MWCNTs which have high electronic conductivity offer a direct electron transfer path while GONRs offer large surface area with carboxylic acid groups that enhance the adsorption of Na ions on the surface and enlarge the capacity. Capacity was reduced when the amount of carboxylic acid groups on MWCNT@GONR was decreased after annealing, showing a strong evidence that surface defects and functional groups on MWCNT@GONR offer more place for accommodating Na ions. Above results prove that MWCNT@GONR could be a promising alternative carbon buffering matrix to graphene in preparing carbon composites with alloy type or metal oxide/sulphide anode materials. A full cell with MWCNT@GONR as anode and P2-Na_xMnO_2 as cathode was fabricated in order to demonstrate an actual device application of MWCNT@GONR, and it presented a high energy density up to 99 Wh kg^{-1}. MWCNT@GONR

is easily-synthesized and cost-efficient exhibiting high capacities at different cycling rates with good stability, and it is a safe and environmentally friendly material for commercial NIB applications.

Based on the above findings, $Na_6[V_{10}O_{28}]$, **SWCNT-TBA-PV_2Mo_{10}**, and MWCNT@GONR are promising electrode candidates for SC, LIB, and NIB applications.

Chapter 7 Future Works

7.1 Vanadium-based POMs as electrode materials for LIBs and NIBs

The vanadium-based POMs exhibit high capacities as electrode materials for LIBs and NIBs which were developed in this thesis and from literature. Thus we will focus on V-based POMs with different structures and additional transition metals in the POM clusters as electrode materials for LIBs and NIBs. In order to design ideal POMs as electrode materials with high energy and power densities, the electrochemical properties of different transition metal substitutions in POMs will be investigated in this research. Several polyoxovanadates with different transition metal substitutions such as $Na_9[PV_{14}O_{42}]$, $Na_7[NiV_{13}O_{38}]$, $Na_7[MnV_{13}O_{38}]$, $Na_7[FeV_{13}O_{38}]$, $Na_7[CoV_{13}O_{38}]$, $K_6[V_{10}O_{28}]$, $(KH)_9[PV_{14}O_{42}]$, $K_7[NiV_{13}O_{38}]$, and $K_7[MnV_{13}O_{38}]$ will be synthesized and investigated. Further studies of the charge storage and transport mechanisms with different POMs in LIBs and NIBs can be carried out through various electrochemical characterization techniques, including cyclic voltammetry (CV), in-situ X-ray absorption fine structure (XAFS), and chronoamperometry experiments.

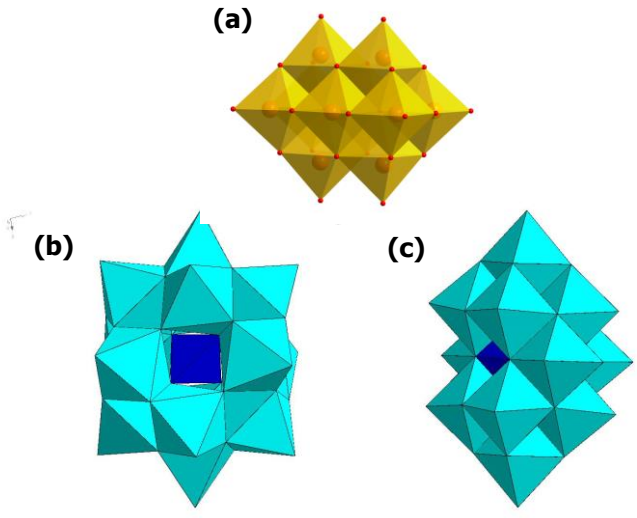

Figure 7.1 Structures of (a) $[V_{10}O_{28}]^{6-}$, (b) $[PV_{14}O_{42}]^{9-}$, and (c) $[NiV_{13}O_{38}]^{7-}$ or $[MnV_{13}O_{38}]^{7-}$.

7.2 POM/Carbon hybrid materials for SCs

POMs are metal oxide clusters with low electronic conductivity. In this thesis, a Nano hybrid material, **SWCNT-TBA-PV_2Mo_{10}**, has been demonstrated as a promising electrode material for SCs. Thus, further nanostructured carbon materials such as graphene and MWCNT@GONR can be employed to improve the electronic conductivity and thus enhance the power density as well as the specific capacitance. Furthermore, anchoring POMs onto nanostructured carbon materials to enhance the cycling stability is also proposed to prevent dissolution of POMs into aqueous electrolytes.

7.3 MWCNT@GONR with different functional groups as electrode materials for NIBs

In this thesis, MWCNT@GONR with carboxylic acid groups exhibit excellent performance as anode materials for NIBs. Thus, the influence of different kinds of functional groups such nitrogen-containing and oxygen-containing groups on Na ions adsorption can be investigated in order to achieve better performance for NIBs. The nitrogen-containing functional groups on MWCNT@GONR can be prepared by a simple microwave method with nitrogen-containing solutions. Those MWCNT@GONR samples will be characterized by FT-IR, TGA, BET surface area measurement, XRD, XPS, Raman, FESEM, and HRTEM. The battery performance will be analyzed by CV and GCD. Furthermore, in order to investigate the influence of different functional groups on Na ions adsorption, the MWCNT@GONR samples will be investigated with fundamental understanding on charge storage and transport mechanism by applying density functional theory (DFT).

References

(1) Soloveichik, G. L. *Annu. Rev. Chem. Biomol. Eng.* **2011**, *2*, 503.
(2) Wang, H.; Hamanaka, S.; Yokoyama, T.; Yoshikawa, H.; Awaga, K. *Chemistry-an Asian Journal* **2011**, *6*, 1074.
(3) Ni, E. F.; Uematsu, S.; Quan, Z.; Sonoyama, N. *Journal of Nanoparticle Research* **2013**, *15*.
(4) Wang, Y. X.; Chou, S. L.; Liu, H. K.; Dou, S. X. *Carbon* **2013**, *57*, 202.
(5) Pramudita, J. C.; Pontiroli, D.; Magnani, G.; Gaboardi, M.; Ricco, M.; Milanese, C.; Brand, H. E. A.; Sharma, N. *Chemelectrochem* **2015**, *2*, 600.
(6) Yabuuchi, N.; Kubota, K.; Dahbi, M.; Komaba, S. *Chemical Reviews* **2014**, *114*, 11636.
(7) Park, S.; Lian, K.; Gogotsi, Y. *Journal of the Electrochemical Society* **2009**, *156*, A921.
(8) Simon, P.; Gogotsi, Y. *Nature Materials* **2008**, *7*, 845.
(9) Egashira, M.; Okada, S.; Korai, Y.; Yamaki, J.; Mochida, I. *Journal of Power Sources* **2005**, *148*, 116.
(10) Portet, C.; Yushin, G.; Gogotsi, Y. *Carbon* **2007**, *45*, 2511.
(11) Stoller, M. D.; Park, S. J.; Zhu, Y. W.; An, J. H.; Ruoff, R. S. *Nano Letters* **2008**, *8*, 3498.
(12) Schwegler, M. A.; Vinke, P.; Vandereijk, M.; Vanbekkum, H. *Applied Catalysis a-General* **1992**, *80*, 41.
(13) Lee, H. Y.; Goodenough, J. B. *Journal of Solid State Chemistry* **1999**, *148*, 81.
(14) Zhang, Y.; Li, J.; Kang, F.; Gao, F.; Wang, X. *International Journal of Hydrogen Energy* **2012**, *37*, 860.
(15) Cottineau, T.; Toupin, M.; Delahaye, T.; Brousse, T.; Belanger, D. *Applied Physics a-Materials Science & Processing* **2006**, *82*, 599.
(16) Gomez-Romero, P.; Chojak, M.; Cuentas-Gallegos, K.; Asensio, J. A.; Kulesza, P. J.; Casan-Pastor, N.; Lira-Cantu, M. *Electrochemistry Communications* **2003**, *5*, 149.
(17) Cuentas-Gallegos, A. K.; Lira-Cantu, M.; Casan-Pastor, N.; Gomez-Romero, P. *Advanced Functional Materials* **2005**, *15*, 1125.
(18) Cuentas-Gallegos, A.; Martinez-Rosales, R.; Baibarac, M.; Gomez-Romero, P.; Rincon, M. E. *Electrochemistry Communications* **2007**, *9*, 2088.
(19) Suppes, G. M.; Cameron, C. G.; Freund, M. S. *Journal of the Electrochemical Society* **2010**, *157*, A1030.
(20) Chen , H.-Y.; Wee , G.; Al-Oweini, R.; Friedl , J.; Tan, K. S.; Wang, Y.; Wong , C. L.; Kortz, U.; Stimming, U.; Srinivasan, M. *ChemPhysChem* **2014**, *15*, 2162.
(21) Chen, H.-Y.; Al-Oweini, R.; Friedl, J.; Lee, C. Y.; Li, L.; Kortz, U.; Stimming, U.; Srinivasan, M. *Nanoscale* **2015**, *7*, 7934.
(22) Uematsu, S.; Quan, Z.; Suganuma, Y.; Sonoyama, N. *Journal of Power Sources* **2012**, *217*, 13.
(23) Wang, H.; Hamanaka, S.; Nishimoto, Y.; Irle, S.; Yokoyama, T.; Yoshikawa, H.; Awaga, K. *Journal of the American Chemical Society* **2012**, *134*, 4918.
(24) Ni, E.; Uematsu, S.; Sonoyama, N. *Solid State Ionics* **2014**.
(25) Hartung, S.; Bucher, N.; Chen, H.-Y.; Al-Oweini, R.; Sreejith, S.; Borah, P.; Yanli, Z.; Kortz, U.; Stimming, U.; Hoster, H. E.; Srinivasan, M. *Journal of Power Sources* **2015**, *288*, 270.
(26) Ponrouch, A.; Goñi, A. R.; Palacín, M. R. *Electrochemistry Communications* **2013**, *27*, 85.
(27) Wang, Z. H.; Qie, L.; Yuan, L. X.; Zhang, W. X.; Hu, X. L.; Huang, Y. H. *Carbon* **2013**, *55*, 328.

(28) Xu, Y.; Memarzadeh Lotfabad, E.; Wang, H.; Farbod, B.; Xu, Z.; Kohandehghan, A.; Mitlin, D. *Chemical Communications* **2013**, *49*, 8973.
(29) Wang, Y.; Yu, X.; Xu, S.; Bai, J.; Xiao, R.; Hu, Y.-S.; Li, H.; Yang, X.-Q.; Chen, L.; Huang, X. *Nat Commun* **2013**, *4*.
(30) Chevrier, V. L.; Ceder, G. *Journal of The Electrochemical Society* **2011**, *158*, A1011.
(31) Darwiche, A.; Marino, C.; Sougrati, M. T.; Fraisse, B.; Stievano, L.; Monconduit, L. *Journal of the American Chemical Society* **2012**, *134*, 20805.
(32) Qian, J.; Wu, X.; Cao, Y.; Ai, X.; Yang, H. *Angewandte Chemie* **2013**, *125*, 4731.
(33) Nithya, C.; Gopukumar, S. *Journal of Materials Chemistry A* **2014**, *2*, 10516.
(34) Yu, G.; Xie, X.; Pan, L.; Bao, Z.; Cui, Y. *Nano Energy* **2013**, *2*, 213.
(35) Conway, B. E. *Electrochemical Supercapacitors: Scientific Fundamentals and Technological Applications*; Springer, 1999.
(36) Conway, B. E.; Pell, W. G. *Journal of Solid State Electrochemistry* **2003**, *7*, 637.
(37) Haas, O.; J. Cairns, E. *Annual Reports Section "C" (Physical Chemistry)* **1999**, *95*, 163.
(38) Rose, M. F.; Johnson, C.; Owens, T.; Stephens, B. *Journal of Power Sources* **1994**, *47*, 303.
(39) Frackowiak, E.; Jurewicz, K.; Delpeux, S.; Beguin, F. *Journal of Power Sources* **2001**, *97-8*, 822.
(40) Pandolfo, A. G.; Hollenkamp, A. F. *Journal of Power Sources* **2006**, *157*, 11.
(41) Wallace, G. G.; Chen, J.; Li, D.; Moulton, S. E.; Razal, J. M. *Journal of Materials Chemistry* **2010**, *20*, 3553.
(42) Subrahmanyam, K. S.; Vivekchand, S. R. C.; Govindaraj, A.; Rao, C. N. R. *Journal of Materials Chemistry* **2008**, *18*, 1517.
(43) Zhao, X.; Tian, H.; Zhu, M.; Tian, K.; Wang, J. J.; Kang, F.; Outlaw, R. A. *Journal of Power Sources* **2009**, *194*, 1208.
(44) Pham, G. T.; Park, Y. B.; Liang, Z.; Zhang, C.; Wang, B. *Composites Part B-Engineering* **2008**, *39*, 209.
(45) Yang, Y. L.; Wang, Y. D.; Ren, Y.; He, C. S.; Deng, J. N.; Nan, J.; Chen, J. G.; Zuo, L. *Materials Letters* **2008**, *62*, 47.
(46) Niu, C. M.; Sichel, E. K.; Hoch, R.; Moy, D.; Tennent, H. *Applied Physics Letters* **1997**, *70*, 1480.
(47) Ma, R. Z.; Liang, J.; Wei, B. Q.; Zhang, B.; Xu, C. L.; Wu, D. H. *Journal of Power Sources* **1999**, *84*, 126.
(48) Zhang, Y.; Feng, H.; Wu, X. B.; Wang, L. Z.; Zhang, A. Q.; Xia, T. C.; Dong, H. C.; Li, X. F.; Zhang, L. S. *International Journal of Hydrogen Energy* **2009**, *34*, 4889.
(49) Rudge, A.; Raistrick, I.; Gottesfeld, S.; Ferraris, J. P. *Electrochimica Acta* **1994**, *39*, 273.
(50) Zheng, J. P.; Cygan, P. J.; Jow, T. R. *Journal of the Electrochemical Society* **1995**, *142*, 2699.
(51) Kawasaki, N.; Wang, H.; Nakanishi, R.; Hamanaka, S.; Kitaura, R.; Shinohara, H.; Yokoyama, T.; Yoshikawa, H.; Awaga, K. *Angewandte Chemie-International Edition* **2011**, *50*, 3471.
(52) Yamada, A.; Goodenough, J. B. *Journal of the Electrochemical Society* **1998**, *145*, 737.
(53) Pope, M. T.; Muller, A. *Angewandte Chemie-International Edition in English* **1991**, *30*, 34.
(54) *Issue dedicated to Polyoxometalates, European Journal of Inorganic Chemistry 34*; Kortz, U., Ed., 2009; Vol. 34.
(55) Pope, M. T.; Kortz, U. In *Encyclopedia of Inorganic and Bioinorganic Chemistry*; John Wiley & Sons, Ltd: 2011.
(56) *Polyoxometalate Chemistry: From Topology via Self-Assembly to Applications*; Pope, M. T.; Müller, A., Eds.; Kluwer Academic: Dordrecht, The Netherlands, 2001.

(57) *Special Issue on Polyoxometalates, Chemical Reviews 98*; Hill, C. L., Ed., 1998; Vol. 98.
(58) White, A. M.; Slade, R. C. T. *Electrochimica Acta* **2003**, *48*, 2583.
(59) White, A. M.; Slade, R. C. T. *Electrochimica Acta* **2004**, *49*, 861.
(60) Akter, T.; Hu, K. W.; Lian, K. *Electrochimica Acta* **2011**, *56*, 4966.
(61) Ruiz, V.; Suarez-Guevara, J.; Gomez-Romero, P. *Electrochemistry Communications* **2012**, *24*, 35.
(62) Vaillant, J.; Lira-Cantu, M.; Cuentas-Gallegos, K.; Casan-Pastor, N.; Gomez-Romero, P. *Progress in Solid State Chemistry* **2006**, *34*, 147.
(63) Skunik, M.; Chojak, M.; Rutkowska, I. A.; Kulesza, P. J. *Electrochimica Acta* **2008**, *53*, 3862.
(64) Bajwa, G.; Akter, T.; Lian, K. In *Fullerenes, Nanotubes, and Carbon Nanostructures - 219th Ecs Meeting*; Guldi, D., Ed. 2011; Vol. 35, p 31.
(65) White, A. M.; Slade, R. C. T. *Synthetic Metals* **2003**, *139*, 123.
(66) Bajwa, G.; Genovese, M.; Lian, K. *Ecs Journal of Solid State Science and Technology* **2013**, *2*, M3046.
(67) Bajwa, G. Master thesis, University of Toronto, 2012.
(68) Etacheri, V.; Marom, R.; Elazari, R.; Salitra, G.; Aurbach, D. *Energy & Environmental Science* **2011**, *4*, 3243.
(69) Yazami, R.; Touzain, P. *Journal of Power Sources* **1983**, *9*, 365.
(70) Thackeray, M.; David, W.; Bruce, P.; Goodenough, J. *Materials Research Bulletin* **1983**, *18*, 461.
(71) Wakihara, M. *Materials Science and Engineering: R: Reports* **2001**, *33*, 109.
(72) Ji, L.; Lin, Z.; Alcoutlabi, M.; Zhang, X. *Energy & Environmental Science* **2011**, *4*, 2682.
(73) Bruce, P. G.; Scrosati, B.; Tarascon, J. M. *Angewandte Chemie International Edition* **2008**, *47*, 2930.
(74) Yoshikawa, H.; Kazama, C.; Awaga, K.; Satoh, M.; Wada, J. *Chemical Communications* **2007**, 3169.
(75) Sonoyama, N.; Suganuma, Y.; Kume, T.; Quan, Z. *Journal of Power Sources* **2011**, *196*, 6822.
(76) Wang, H.; Kawasaki, N.; Yokoyama, T.; Yoshikawa, H.; Awaga, K. *Dalton Transactions* **2012**, *41*, 9863.
(77) Wang, S.; Li, H. L.; Li, S.; Liu, F.; Wu, D. Q.; Feng, X. L.; Wu, L. X. *Chemistry-a European Journal* **2013**, *19*, 10895.
(78) Yang, H. X.; Song, T.; Liu, L.; Devadoss, A.; Xia, F.; Han, H.; Park, H.; Sigmund, W.; Kwon, K.; Paik, U. *Journal of Physical Chemistry C* **2013**, *117*, 17376.
(79) Kume, K.; Kawasaki, N.; Wang, H.; Yamada, T.; Yoshikawa, H.; Awaga, K. *Journal of Materials Chemistry A* **2014**, *2*, 3801.
(80) Ni, E.; Kume, T.; Uematsu, S.; Quan, Z.; Sonoyama, N. *Electrochemistry* **2014**, *82*, 14.
(81) Wang, H.; Yamada, T.; Hamanaka, S.; Yoshikawa, H.; Awaga, K. *Chemistry Letters* **2014**, *43*, 1067.
(82) Cheng, J.-H.; Pan, C.-J.; Lee, J.-F.; Chen, J.-M.; Guignard, M.; Delmas, C.; Carlier, D.; Hwang, B.-J. *Chemistry of Materials* **2014**, *26*, 1219.
(83) Chidsey, C. E. D. *Science* **1991**, *251*, 919.
(84) Henstridge, M. C.; Laborda, E.; Rees, N. V.; Compton, R. G. *Electrochimica Acta* **2012**, *84*, 12.
(85) Bai, P.; Bazant, M. Z. *Nature Communications* **2014**, *5*.
(86) Bai, P.; Tian, G. Y. *Electrochimica Acta* **2013**, *89*, 644.

(87) Friedl, J.; Al-Oweini, R.; Herpich, M.; Keita, B.; Kortz, U.; Stimming, U. *Electrochimica Acta* **2014**, *141*, 357.
(88) Wang, L. P.; Yu, L. H.; Wang, X.; Srinivasan, M.; Xu, Z. C. J. *Journal of Materials Chemistry A* **2015**, *3*, 9353.
(89) Wen, Y.; He, K.; Zhu, Y.; Han, F.; Xu, Y.; Matsuda, I.; Ishii, Y.; Cumings, J.; Wang, C. *Nat Commun* **2014**, *5*.
(90) Sun, Y.; Zhao, L.; Pan, H.; Lu, X.; Gu, L.; Hu, Y.-S.; Li, H.; Armand, M.; Ikuhara, Y.; Chen, L.; Huang, X. *Nat Commun* **2013**, *4*, 1870.
(91) Senguttuvan, P.; Rousse, G.; Seznec, V.; Tarascon, J.-M.; Palacín, M. R. *Chemistry of Materials* **2011**, *23*, 4109.
(92) Alcántara, R.; Jaraba, M.; Lavela, P.; Tirado, J. L. *Chemistry of Materials* **2002**, *14*, 2847.
(93) Hariharan, S.; Saravanan, K.; Ramar, V.; Balaya, P. *Physical Chemistry Chemical Physics* **2013**, *15*, 2945.
(94) Hariharan, S.; Saravanan, K.; Balaya, P. *Electrochemistry Communications* **2013**, *31*, 5.
(95) Yuan, S.; Huang, X.-l.; Ma, D.-l.; Wang, H.-g.; Meng, F.-z.; Zhang, X.-b. *Advanced Materials* **2014**, *26*, 2273.
(96) Ryu, H.-S.; Kim, J.-S.; Park, J.; Park, J.-Y.; Cho, G.-B.; Liu, X.; Ahn, I.-S.; Kim, K.-W.; Ahn, J.-H.; Ahn, J.-P.; Martin, S. W.; Wang, G.; Ahn, H.-J. *Journal of Power Sources* **2013**, *244*, 764.
(97) Hu, Z.; Wang, L.; Zhang, K.; Wang, J.; Cheng, F.; Tao, Z.; Chen, J. *Angewandte Chemie* **2014**, *126*, 13008.
(98) Zhou, T.; Pang, W. K.; Zhang, C.; Yang, J.; Chen, Z.; Liu, H. K.; Guo, Z. *ACS Nano* **2014**, *8*, 8323.
(99) Su, Q.; Du, G.; Zhang, J.; Zhong, Y.; Xu, B.; Yang, Y.; Neupane, S.; Li, W. *ACS Nano* **2014**, *8*, 3620.
(100) Shadike, Z.; Zhou, Y.-N.; Ding, F.; Sang, L.; Nam, K.-W.; Yang, X.-Q.; Fu, Z.-W. *Journal of Power Sources* **2014**, *260*, 72.
(101) Wang, Y.-X.; Chou, S.-L.; Liu, H.-K.; Dou, S.-X. *Carbon* **2013**, *57*, 202.
(102) Kim, Y.; Kim, Y.; Choi, A.; Woo, S.; Mok, D.; Choi, N.-S.; Jung, Y. S.; Ryu, J. H.; Oh, S. M.; Lee, K. T. *Advanced Materials* **2014**, *26*, 4139.
(103) Bresser, D.; Mueller, F.; Buchholz, D.; Paillard, E.; Passerini, S. *Electrochimica Acta* **2014**, *128*, 163.
(104) Oh, S.-M.; Myung, S.-T.; Jang, M.-W.; Scrosati, B.; Hassoun, J.; Sun, Y.-K. *Physical Chemistry Chemical Physics* **2013**, *15*, 3827.
(105) Kim, J.-C.; Kim, D.-W. *Electrochemistry Communications* **2014**, *46*, 124.
(106) Gonzalez, J. R.; Nacimiento, F.; Alcantara, R.; Ortiz, G. F.; Tirado, J. L. *CrystEngComm* **2013**, *15*, 9196.
(107) Thorne, J. S.; Dunlap, R. A.; Obrovac, M. N. *Electrochimica Acta* **2013**, *112*, 133.
(108) Yamamoto, T.; Nohira, T.; Hagiwara, R.; Fukunaga, A.; Sakai, S.; Nitta, K.; Inazawa, S. *Electrochimica Acta* **2014**, *135*, 60.
(109) He, M.; Kravchyk, K.; Walter, M.; Kovalenko, M. V. *Nano Letters* **2014**, *14*, 1255.
(110) Abel, P. R.; Lin, Y.-M.; de Souza, T.; Chou, C.-Y.; Gupta, A.; Goodenough, J. B.; Hwang, G. S.; Heller, A.; Mullins, C. B. *The Journal of Physical Chemistry C* **2013**, *117*, 18885.
(111) Xiao, L.; Cao, Y.; Xiao, J.; Wang, W.; Kovarik, L.; Nie, Z.; Liu, J. *Chemical Communications* **2012**, *48*, 3321.
(112) Zhao, L.; Zhao, J.; Hu, Y.-S.; Li, H.; Zhou, Z.; Armand, M.; Chen, L. *Advanced Energy Materials* **2012**, *2*, 962.

(113) Park, Y.; Shin, D.-S.; Woo, S. H.; Choi, N. S.; Shin, K. H.; Oh, S. M.; Lee, K. T.; Hong, S. Y. *Advanced Materials* **2012**, *24*, 3562.
(114) Nithya, C.; Gopukumar, S. *Chemsuschem* **2013**, *6*, 898.
(115) Yu, D. Y. W.; Prikhodchenko, P. V.; Mason, C. W.; Batabyal, S. K.; Gun, J.; Sladkevich, S.; Medvedev, A. G.; Lev, O. *Nat Commun* **2013**, *4*.
(116) Domaille, P. J. *Journal of the American Chemical Society* **1984**, *106*, 7677.
(117) Tsigdino.Ga; Hallada, C. J. *Inorganic Chemistry* **1968**, *7*, 437.
(118) Nomiya, K.; Yagishita, K.; Nemoto, Y.; Kamataki, T. A. *Journal of Molecular Catalysis a-Chemical* **1997**, *126*, 43.
(119) Sun, C. L.; Chang, C. T.; Lee, H. H.; Zhou, J. G.; Wang, J.; Sham, T. K.; Pong, W. F. *Acs Nano* **2011**, *5*, 7788.
(120) Lin, L. Y.; Yeh, M. H.; Tsai, J. T.; Huang, Y. H.; Sun, C. L.; Ho, K. C. *Journal of Materials Chemistry A* **2013**, *1*, 11237.
(121) Bucher, N.; Hartung, S.; Nagasubramanian, A.; Cheah, Y. L.; Hoster, H. E.; Madhavi, S. *Acs Applied Materials & Interfaces* **2014**, *6*, 8059.
(122) Wee, G.; Soh, H. Z.; Cheah, Y. L.; Mhaisalkar, S. G.; Srinivasan, M. *Journal of Materials Chemistry* **2010**, *20*, 6720.
(123) Chen, Z.; Augustyn, V.; Wen, J.; Zhang, Y. W.; Shen, M. Q.; Dunn, B.; Lu, Y. F. *Advanced Materials* **2011**, *23*, 791.
(124) Ramos, S.; Duarte, R. O.; Moura, J. J. G.; Aureliano, M. *Dalton Transactions* **2009**, 7985.
(125) Zhetcheva, V. D. K.; Pavlova, L. P. *Turkish Journal of Chemistry* **2011**, *35*, 215.
(126) Chen, H.-Y.; Friedl, J.; Pan, C.-J.; Haider, A.; Al-Oweini, R.; Cheah, Y. L.; Lin, M.-H.; Kortz, U.; Hwang, B.-J.; Srinivasan, M.; Stimming, U. *Physical Chemistry Chemical Physics* **2017**, DOI: 10.1039/C6CP05768C.
(127) Chen, Z.; Concepcion, J. J.; Brennaman, M. K.; Kang, P.; Norris, M. R.; Hoertz, P. G.; Meyer, T. J. *Proceedings of the National Academy of Sciences* **2012**, *109*, 15606.
(128) Aravindan, V.; Cheah, Y. L.; Mak, W. F.; Wee, G.; Chowdari, B. V. R.; Madhavi, S. *ChemPlusChem* **2012**, *77*, 570.
(129) Li, L. L.; Peng, S. J.; Cheah, Y. L.; Teh, P. F.; Wang, J.; Wee, G.; Ko, Y. W.; Wong, C. L.; Srinivasan, M. *Chemistry-a European Journal* **2013**, *19*, 5892.
(130) Zhang, F.; Zhang, T. F.; Yang, X.; Zhang, L.; Leng, K.; Huang, Y.; Chen, Y. S. *Energy & Environmental Science* **2013**, *6*, 1623.
(131) Zheng, C.; Qian, W.; Wei, F. *Materials Science and Engineering: B* **2012**, *177*, 1138.
(132) Pettersson, L.; Andersson, I.; Selling, A.; Grate, J. H. *Inorganic Chemistry* **1994**, *33*, 982.
(133) Arichi, J.; Eternot, M.; Louis, B. *Catalysis Today* **2008**, *138*, 117.
(134) Al-Oweini, R.; El-Rassy, H. *Journal of Molecular Structure* **2009**, *919*, 140.
(135) Al-Oweini, R.; Bassil, B. S.; Palden, T.; Keita, B.; Lan, Y. H.; Powell, A. K.; Kortz, U. *Polyhedron* **2013**, *52*, 461.
(136) Al-Oweini, R.; Bassil, B. S.; Friedl, J.; Kottisch, V.; Ibrahim, M.; Asano, M.; Keita, B.; Novitchi, G.; Lan, Y. H.; Powell, A.; Stimming, U.; Kortz, U. *Inorganic Chemistry* **2014**, *53*, 5663.
(137) Chen, H.-Y.; Bucher, N.; Hartung, S.; Li, L.; Friedl, J.; Liou, H.-P.; Sun, C.-L.; Stimming, U.; Srinivasan, M. *Advanced Materials Interfaces* **2016**, *3*, 1600357.
(138) Gupta, V.; Saleh, T. *Syntheses of Carbon Nanotube-Metal Oxides Composites; Adsorption and Photo-degradation*, 2011.
(139) Cruz-Delgado, V. J.; Espana-Sanchez, B. L.; Avila-Orta, C. A.; Medellin-Rodriguez, F. J. *Polymer Journal* **2012**, *44*, 952.
(140) Nasibulina, L. I.; Anoshkin, I. V.; Nasibulin, A. G.; Cwirzen, A.; Penttala, V.; Kauppinen, E. I. *Journal of Nanomaterials* **2012**.

(141) Hussain, S.; Jha, P.; Chouksey, A.; Raman, R.; Islam, S. S.; Islam, T.; Choudhary, P. K. *Journal of Modern Physics* **2011**, *Vol.02No.06*, 6.
(142) David, L.; Singh, G. *The Journal of Physical Chemistry C* **2014**, *118*, 28401.
(143) Friedl, J.; Bauer, C. M.; Rinaldi, A.; Stimming, U. *Carbon* **2013**, *63*, 228.
(144) Huh, S. H. In *Physics and Applications of Graphene - Experiments*; Mikhailov, S., Ed.; InTech: Rijeka, Croatia, 2011, p 73.
(145) Xiao, B. W.; Li, X. F.; Li, X.; Wang, B. Q.; Langford, C.; Li, R. Y.; Sun, X. L. *Journal of Physical Chemistry C* **2014**, *118*, 881.
(146) Li, J.-M.; Chang, K.-H.; Wu, T.-H.; Hu, C.-C. *Journal of Power Sources* **2013**, *224*, 59.
(147) Kalubarme, R. S.; Jadhav, H. S.; Park, C.-J. *Electrochimica Acta* **2013**, *87*, 457.
(148) Li, J. M.; Chang, K. H.; Hu, C. C. *Electrochemistry Communications* **2010**, *12*, 1800.
(149) Chen, J.; Liu, S. L.; Feng, W.; Zhang, G. Q.; Yang, F. L. *Physical Chemistry Chemical Physics* **2013**, *15*, 5664.
(150) Nitta, N.; Wu, F.; Lee, J. T.; Yushin, G. *Materials Today* **2015**, *18*, 252.
(151) Tarascon, J. M.; Armand, M. *Nature* **2001**, *414*, 359.
(152) Mansour, A. N.; Smith, P. H.; Baker, W. M.; Balasubramanian, M.; McBreen, J. *Journal of the Electrochemical Society* **2003**, *150*, A403.
(153) Bard, A. J.; Faulkner, L. R. *Electrochemical Methods: Fundamentals and Applications, 2nd Edition*; Wiley Global Education: USA, 2000.
(154) Bai, P.; Cogswell, D. A.; Bazant, M. Z. *Nano Letters* **2011**, *11*, 4890.
(155) Laborda, E.; Henstridge, M. C.; Batchelor-McAuley, C.; Compton, R. G. *Chemical Society Reviews* **2013**, *42*, 4894.
(156) Chen, H.-Y.; Wee, G.; Al-Oweini, R.; Friedl, J.; Tan, K. S.; Wang, Y.; Wong, C. L.; Kortz, U.; Stimming, U.; Srinivasan, M. *ChemPhysChem* **2014**.
(157) Barth, M.; Lapkowski, M.; Lefrant, S. *Electrochimica Acta* **1999**, *44*, 2117.
(158) Song, I. K.; Kaba, M. S.; Barteau, M. A. *Journal of Physical Chemistry* **1996**, *100*, 17528.
(159) Bommier, C.; Luo, W.; Gao, W.-Y.; Greaney, A.; Ma, S.; Ji, X. *Carbon* **2014**, *76*, 165.
(160) Jin, J.; Shi, Z.-q.; Wang, C.-y. *Electrochimica Acta* **2014**, *141*, 302.
(161) Tang, K.; Fu, L.; White, R. J.; Yu, L.; Titirici, M.-M.; Antonietti, M.; Maier, J. *Advanced Energy Materials* **2012**, *2*, 873.

Publication list

Journal Papers

1. Han-Yi Chen, Grace Wee, Rami Al-Oweini, Jochen Friedl, Kim Soon Tan, Yuxi Wang, Chui Ling Wong, Ulrich Kortz, Ulrich Stimming*, and Madhavi Srinivasan*, **"A Polyoxovanadate as an Advanced Electrode Material for Supercapacitors"**, *ChemPhysChem*, **2014**, 15, 2162-2169
2. Han-Yi Chen, Rami Al-Oweini, Jochen Friedl, Ching Yi Lee, Linlin Li, Ulrich Kortz, Ulrich Stimming*, Madhavi Srinivasan*, "**A Novel SWCNT-Polyoxometalate Nanohybrid Material as Electrode for Electrochemical Supercapacitors**", *Nanoscale*, **2015**, 7, 7934-7941
3. Steffen Hartung, Nicolas Bucher, Han-Yi Chen, Rami Al-Oweini, Sivaramapanicker Sreejith, Parijat Borah, Zhao Yanli, Ulrich Kortz, Ulrich Stimming, Harry Hoster, Madhavi Srinivasan*, **"Vanadium-based Polyoxometalate as New Material for Sodium ion Battery Anodes"**, *Journal of Power Sources*, **2015**, 288, 270-277
4. Meng-Che Tu, Han-Yi Chen, Yuxi Wang, Shabbir M. Moochhala, Palaniappan Alagappan, Bo Liedberg***,** "**Immunosensor Based on Carbon Nanotube/Manganese Dioxide Electrochemical Tags**", *Analytica Chimica Acta*, **2015**, 853, 228-233
5. Linlin Li, Shengjie Peng, Han-Yi Chen, Xiaopeng Han, Fangyi Cheng, Madhavi Srinivasan, Qingyu Yan, Stefan Adams, Seeram Ramakrishna, and Jun Chene*, **"Polypyrrole-coated Hierarchical Porous Composites Nanoarchitectures for Advanced Solid-state Flexible Hybrid Devices",** *Nano Energy*, **2016**, 19, 307-317
6. Ali Haider, Masooma Ibrahim, Bassem S. Bassil, Akina M. Carey, Anh Nguyen Viet, Xiaolin Xing, Wassim W. Ayass, Juan F. Miñambres, Rongji Liu, Guangjin Zhang, Bineta Keita, Valeriu Mereacre, Annie K. Powell, Kamil Balinski, Alpha N'Diaye, Karsten Kuepper, Han-

Yi Chen, Ulrich Stimming, and Ulrich Kortz*, "**Oxidation State Tuning of Two Mixed-Valent Mn16-Containing Heteropolyanions: Synthesis, Characterization, and Potential Applications**", *Inorganic Chemistry*, **2016**, 55, 2755-2764

7. Hsin-Yi Wang, Ting-Shan Chan, Han-Yi Chen, Hao Ming Chen, and Bin Liu*, **Identification of Catalytic Sites for Water Oxidation in Normal Spinel Cobalt Oxide**", *Journal of the American Chemical Society*, **2016**, 138, 36-39

8. Nicolas Bucher, Steffen Hartung, Joseph Franklin, Anna Wise, Linda Lim, **Han-Yi Chen**, Johanna Weker, Michael Toney, Madhavi Srinivasan*, **"P2-$Na_xCo_yMn_{1-y}O_2$ (y = 0, 0.1) as Cathode Materials in Sodium-Ion Batteries—Effects of Doping and Morphology To Enhance Cycling Stability"**, *Chemistry of Materials*, **2016**, 28, 2041-2051

9. Steffen Hartung, Nicolas Bucher, Joseph Franklin, Anna Wise, Linda Lim, **Han-Yi Chen**, Johanna Weker, Maria-E. Michel-Beyerle, Michael Toney, Madhavi Srinivasan*, **"Mechanism of Na^+ Insertion in Alkali Vanadates and its Influence on Battery Performance"**, *Advanced Energy Materials*, **2016**, 6, 1502336

10. Hsin-Yi Wang, **Han-Yi Chen**, Ying-Ya Hsu, Ulrich Stimming, Hao Ming Chen, and Bin Liu*,"**Modulation of Crystal Surface and Lattice by Doping: Achieving Ultrafast Metal-Ion Insertion in Anatase TiO_2"**, *ACS Applied Materials & Interfaces*, **2016**, 8, 29186–29193

11. Han-Yi Chen, Nicolas Bucher, Steffen Hartung, Jochen Friedl, Huei- Ping Liou, Linlin Li, Chia-Liang Sun, Ulrich Stimming*, and Madhavi Srinivasan*, " **A Multi-walled Carbon Nanotube Core with Graphene Oxide Nanoribbon Shell as Anode Material for Sodium Ion Batteries**", *Advanced Materials Interfaces*, **2016**, 3, 1600357.

12. Han-Yi Chen, Jochen Friedl, Chun-Jern Pan, Rami Al-Oweini, Ali Haider, Yan Ling Yeah, Ming-Hsien Lin, Ulrich Kortz, Bing-Joe Hwang*, Madhavi Srinivasan*, and Ulrich Stimming*, **"In-situ X-ray Absorption Near Edge Structure Studies and Charge Transfer**

Kinetics of $Na_6[V_{10}O_{28}]$ Electrodes", *Physical Chemistry Chemical Physics*, **2016**, DOI: 10.1039/c6cp05768c

International Conference Proceedings:

1. (Oral Presentation) Han-Yi Chen, Jochen Friedl, Grace Wee, Rami Al-Oweini, Ching Yi Lee, Chui Ling Wong, Ulrich Kortz, Ulrich Stimming*, and Madhavi Srinivasan*, **"Investigations of Vanadium-Containing Polyoxometalates as Electrode Materials for Supercapacitors"**, 7th Asian Conference on Electrochemical Power Sources (ACEPS-7), Osaka, Japan, November 24-27, **2013**.
2. (Poster Presentation) Han-Yi Chen, Jochen Friedl, Rami Al-Oweini, Ulrich Kortz, Madhavi Srinivasan*, Ulrich Stimming* **"Polyoxometalates as Electrode Materials for Molecular Cluster Batteries"**, 15th Topical Meeting of the International Society of Electrochemistry, Niagara Falls, Canada, 27-30 April **2014** .
3. (Poster Presentation) Jochen Friedl, Rami Al-Oweini, Han-Yi Chen, Max Herpich, Ulrich Kortz, Ulrich Stimming, **"Electrochemistry of Tri-Mn Substituted Keggin Ions "**, 15th Topical Meeting of the International Society of Electrochemistry, Niagara Falls, Canada, 27-30 April **2014** .
4. (Poster Presentation) J. Friedl, H. Chen, U. Stimming, **" Polyoxometalates for energy storage applications"**, 3rd International Seminar on Green Energy Conversion, Yamanashi, Japan, August, **2014**
5. (Poster Presentation) Han-Yi Chen, Jochen Friedl, Rami Al-Oweini, Chun-Jern Pan, Bing-Joe Hwang, Ulrich Kortz, Madhavi Srinivasan*, Ulrich Stimming*, **"Electrochemical Studies of Vanadium-Based Polyoxometalate Molecular-Cluster Batteries",** ECS Conference on Electrochemical Energy Conversion & Storage with SOFC-XIV, Glasgow, Scotland, UK, 26-31 July, 2015